Development and application of in-fibre Bragg grating based biomedical pressure sensors

by

Christopher Raymond Stuart Dennison
B.Eng., University of Victoria, 2006

A thesis submitted in partial fulfillment of the
requirements for the degree of

MASTER of APPLIED SCIENCE

in the Department of Mechanical Engineering

July, 2008

Development and application of in-fibre Bragg grating based biomedical pressure sensors

by

Christopher Raymond Stuart Dennison

Supervisory committee

Dr. Peter Wild, Supervisor
(Department of Mechanical Engineering)

Dr. Bradley Buckham, Departmental member
(Department of Mechanical Engineering)

Dr. David Sinton, Departmental member
(Department of Mechanical Engineering)

Dr. Reuven Gordon, Outside member, External examiner
(Department of Electrical and Computer Engineering)

Supervisory committee

Dr. Peter Wild, Supervisor
(Department of Mechanical Engineering)

Dr. Bradley Buckham, Departmental member
(Department of Mechanical Engineering)

Dr. David Sinton, Departmental member
(Department of Mechanical Engineering)

Dr. Reuven Gordon, Outside member, External examiner
(Department of Electrical and Computer Engineering)

Abstract

Two in-fibre Bragg grating based optical pressure sensors were developed to address the limitations of conventional solid-state electronic biomedical sensors. The first sensor, developed for intervertebral disc pressure measurements varying over several MPa, had a major diameter of only 400 μm and sensing area of 0.03 mm^2. This sensor was validated in spine biomechanics studies and was shown to: give accurate and repeatable measurements, be compatible with the small (*e.g.* cervical) discs, and alter disc mechanics less than the current alternative sensor. This sensor is also the smallest, most mechanically compliant disc pressure sensor presented to date.

The second FBG sensor was developed to measure sub-kPa pressure variations and had a major diameter and sensing area of only 200 μm and 0.02 mm^2, respectively. This sensor achieves sub-kPa repeatability through a novel design that is approximately 100 times smaller than other FBG sensors presented with sub-kPa pressure repeatability.

Table of Contents

List of Figures

List of Tables

Nomenclature

Symbols

Δ	indicates change in magnitude when preceding a variable
De	diameter of etched fibre section
Df	diameter of fibre proximal to sensor tip
Do	outside diameter of hypodermic tube
Dp	diameter of polymer coating
Dt	inside diameter of hypodermic tube
E	Young's modulus
ε_i	strain in the i^{th} direction
H	intervertebral disc height
L	sensing length of fibre interferometer
Lg	length of Bragg grating
Ls	length of silicone supported fibre segment
λ	wavelength of light
λ_B	Bragg wavelength reflected by Bragg grating
$\Delta\lambda_W$	linewidth of reflected spectrum from Bragg grating
Λ	spatial period of index of refraction profile in Bragg grating
n	index of refraction
n_o	index of refraction of optical fibre core
ν	Poisson ratio
P	pressure
p_{ij}	element of photo-elastic tensor

ϕ	phase delay of light in fibre interferometer
r^2	linear-regression-calculated correlation coefficient
R_{MAX}	maximum reflectivity of Bragg grating spectrum
t	time
T	traction
W	intervertebral disc width (major axis)
x	magnitude of a generic measurand

Acronyms

FOS	fibre optic sensor
FBG	in-fibre Bragg grating
FSU	functional spine unit
FWHM	full-width at half maximum of reflected spectrum
IVD	intervertebral disc
OSA	optical spectrum analyzer

Acknowledgements

Over the past years, Dr. Peter Wild has provided excellent supervision, guidance and regular encouragement. I will always remember his honesty and integrity.

I would also like to thank Drs. David R. Wilson and Peter A. Cripton of the Department of Orthopaedic Engineering Research and Mechanical Engineering at the University of British Columbia, for their tireless encouragement, guidance, and excellent contributions to the research presented in this thesis.

I can't even begin to describe how much Lindsay means to me. Her love, constant encouragement and laughter made everything better, all of the time.

…..*"work hard, son."*
My father

Chapter 1

Introduction

1.1 Background

Since the nineteen-sixties, fibre-optic technologies have been exploited for biomedical applications [1]. One of the first applications used bundles of optical fibres *in vivo* (*i.e.* in living patients) in an endoscope for the purpose of both illumination and imaging [1]. Contemporary application of fibre-optic technologies has expanded to sensing of physical parameters such as strain [2-4], temperature [3-5], and pressure [6, 7] among others [1]. Pressure measurement in human physiologic systems is an important subset of the possible applications open to fibre-optic sensors (FOSs) because they can be used to understand, diagnose, and monitor various pathologies [1, 8-11] and, in some cases, the current (non-optical) sensing technologies used in these applications have significant limitations [1]. The main limitations of these electronic sensing technologies, for example piezoelectric or semiconductor, are high-cost and long-term instability [1]. Moreover, *in vivo* application of these technologies exposes patients to electrical connections which could result in electric-shock.

The magnitude of pressure within human physiological systems can vary from a few kPa to MPa [1]. One clinical application involving relatively low pressure magnitudes, from approximately 1 kPa to 2 kPa, is monitoring of intracranial pressure [1, 8, 9]. When the human head is subjected to trauma, elevated levels of pressure that are predominantly caused by brain swelling can result [8]. When intracranial pressure exceeds normal levels, various modes of brain damage can result including crushing of brain tissue, shifting of brain structures, and damage resulting from restricted blood and

oxygen supply to brain tissue [1, 8, 9]. Contemporary intracranial pressure sensors usually consist of miniature (*i.e.* diameter smaller than 1 mm) piezoresistive catheters that are extremely fragile, require regular recalibration and, over time, have excessive drift [1]; experimental non-invasive methods have also been developed but are not in widespread use [8].

Another application that is relevant in the context of research and clinical settings, involving relatively high pressures up to approximately 3 MPa, is pressure measurement within human intervertebral discs (IVDs). Disc pressure is an important indicator of disc mechanics which is itself closely linked to disc pathology [10, 11]. When pressure measurement is used in concert with provocative discography, a clinical procedure designed to identify which or whether the IVD is the source of pain, there is significant potential to increase the diagnostic power of the discography procedure [12].

In contemporary disc pressure studies, large (*i.e.* diameter between 1 mm and 3 mm) needle mounted strain-gauge sensors are used [10, 11, 13-16]. However, these sensors are suspected of altering the disc's natural biomechanics due to their rigidity and size [12, 17]. In experimental models with disc heights comparable to the sensor diameter (*e.g.* pig or human cervical/thoracic discs), these sensors can interfere with the vertebral endplates and other anatomic features [12, 14]. These drawbacks limit the utility of the sensors for *ex vivo* research (*i.e.* in cadaver specimens) and can have long term effects on disc health. Moreover, some investigators believe that they can potentially initiate disc degeneration [12, 17]. These long term effects have limited the utility of pressure measurements in conjunction with discography to mainly *ex vivo* experiments [12]. Moreover, because the strain-gage sensors are too large for cervical/thoracic discs there is

a paucity of both experimental data and understanding of the biomechanics in this region of the spine [14].

FOSs can avoid some of the problems mentioned above because they possess key characteristics:

1. Small size and mechanical compliance: FOSs have typical sensing lengths and diameters of the μm scale; because they are small and usually constructed from silica glass with a Young's Modulus and yield strength of 69 GPa and 50 MPa, respectively, they are robust yet offer little mechanical resistance to applied loads;
2. Biocompatibility: glass is chemically inert, stable, and non toxic. The use of low-intensity optical signals ensures patient safety, dielectricity ensures optical signals remain in the core of the optical fibre;
3. Immunity to electromagnetic interference: eliminates the need for external shielding of the sensor and could potentially allow FOSs to be applied in concert with magnetic resonance imaging.

The characteristics outlined above make FOSs attractive alternatives to electronic sensors because FOSs can be both minimally invasive and compatible with other medical diagnostic/imaging procedures already in widespread use. Moreover, because light is used to carry information there is the potential to achieve specific multi-parameter sensing within a single probe [4]. This is because light is described by various parameters (*e.g.* wavelength, phase, polarization direction and intensity *etc.*) that can be modulated to various extents by different physical variables (*e.g.* pressure and temperature). Minimally invasive, multi-parameter sensors are attractive to clinicians because their use can eliminate the need for repeated invasive tests [1].

1.2 Fibre-optic pressure sensors

FOSs can be grouped into three main categories based upon their principle of operation: interferometric, intensity modulating and Bragg grating-based [18]. Interferometric sensors can be further classified by their respective geometry or interference-path configuration. Udd *et al.* (1991) presents a concise listing of interferometric sensors types including ring-resonator, Sagnac, Fabry-Perot, Mach-Zehnder, and Michelson [18].

1.2.1 Interferometric FOSs

Figure 1.1a is a schematic of a fibre-based interferometer. Light leaving the source enters the coupler and is directed to the sensing length of the interferometer. The sensing length, L, is the length of optical fibre between the two partially reflective in-fibre mirrors. Light reflected from the first mirror is directed back into the coupler and into the light intensity detector. The remaining light, not reflected by the first mirror, is transmitted along the sensing length to the second mirror. Some of the light incident on the second mirror is then reflected back toward the first mirror and some of this light is then transmitted through the first mirror and into the light intensity detector. The result of these reflections is two interfering light waves entering the intensity detector.

Variations in measurands that act on the sensing length are detected from the measurand-dependant change in light intensity versus phase delay, ϕ, profile of the two interfering light-waves (Figure 1.1b). The phase delay of light passing through the fibre is a function of the fibre's index of refraction, n, the wavelength of the light, λ, and the sensing length (*i.e.* $\phi = \frac{2\pi n}{\lambda} \mathrm{L}$) [18]. Therefore if variations in the measurand cause

changes in either the index of refraction or the sensing length of the fibre, the intensity versus phase delay profile shown in Figure 1.1b will be altered. Detecting the alterations, including intensity changes and changes in the period of the profile shown in Figure 1.1b, is the most common method of sensing the measurand.

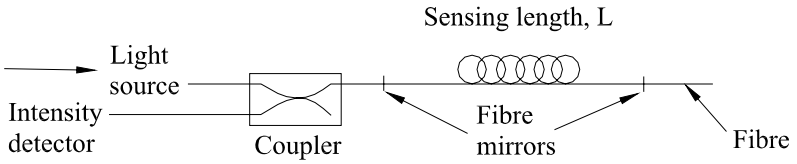

a)

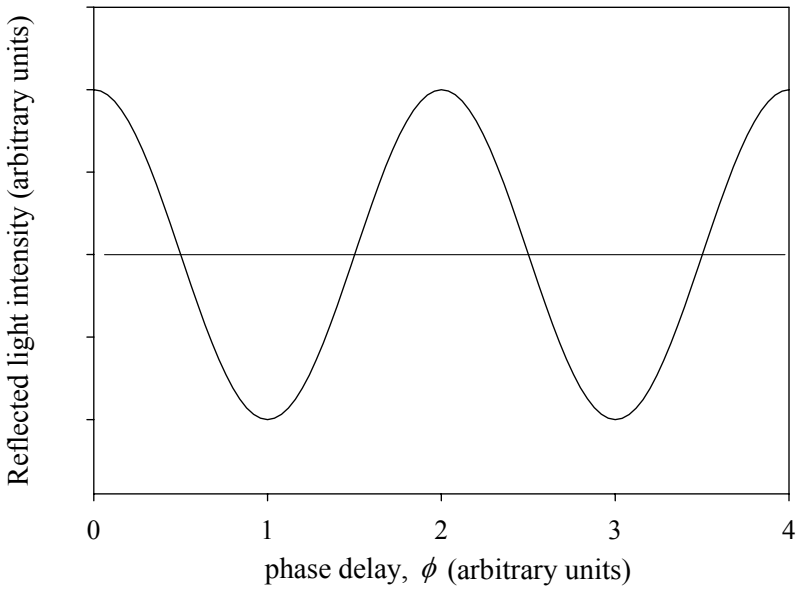

b)

Figure 1.1: a) schematic of fibre interferometer [18], and b) light intensity versus phase delay profile measured by light intensity detector.

Not all interferometers are well suited to pressure measurements. Ring-resonator interferometers, for example, are best suited to sensing rotation or acceleration of a body [18]. These interferometers are spatially distributed and require a fixed geometry not easily miniaturized. For these reasons, this class of sensor is not well-suited for biomedical applications where extremely small sensors are required.

Sagnac interferometers can be used to measure pressure in certain fibre-optic coil configurations. However, this configuration is best suited to acoustic measurements, and not slowly varying pressure signals such as those in the human body [18]. Miniature coil configurations are also difficult to construct.

Pressure sensors have been reported that employ both the Mach-Zehnder [19] and Michelson [19, 20] configurations. However, to achieve the appropriate pressure measurement repeatability for the medical applications already mentioned, these sensor types must have gage lengths on the order of centimeters to meters, too large for many *in vivo* applications. Therefore, the biomedical utility of these sensors is diminished because of poor spatial resolution. In most cases they are simply too large to be inserted *in vivo*.

Conversely, Fabry-Perot interferometers can be constructed to achieve both sub-kPa pressure repeatability as well as sensing lengths and sensor diameters of the sub-mm scale [21-23]. Unfortunately, miniaturized sensors of this configuration have proven to be both difficult to construct and fragile [7, 23]. Moreover, interferometric sensors cannot be easily multiplexed or configured to achieve multi-parameter sensing.

1.2.2 Intensity modulating FOSs

Figure 1.2a is a schematic of a typical fibre-based intensity modulating FOS system [18]. Light leaving source enters the optical coupler and is directed into another fibre. At the tip of this fibre there is a sensing element, as shown inset in Figure 1.2b. Light leaving the core of the fibre is reflected by a deformable reflector (inset Figure 1.2b) and a fraction of this reflected light is coupled back into the fibre core. The fraction of light that re-enters the fibre core is directed back into the coupler and into the light intensity detector.

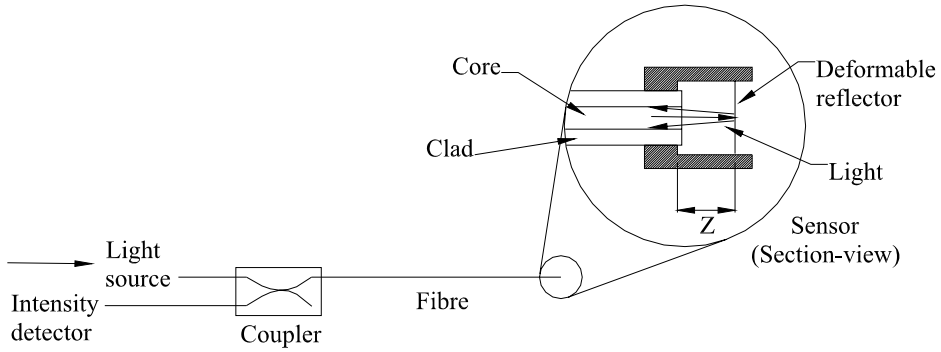

a)

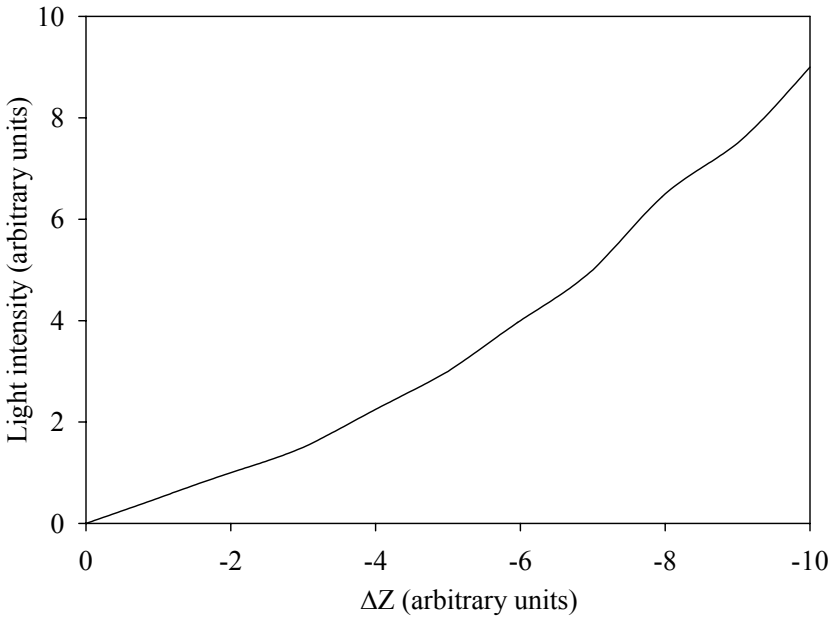

b)

Figure 1.2: a) schematic of intensity modulating FOS, and b) as the distance, Z, decreases (shown as $-\Delta Z$) the intensity of the light measured at the detector increases.

The amount (*i.e.* intensity) of light that is directed into the detector is a function of the distance between the fibre end and the inside surface of the deformable reflector, Z. As shown in Figure 1.2b, when Z decreases (*i.e.* negative ΔZ), the intensity of the light on the detector increases. Variations of a given measurand can then be detected as variations in Z, which are measured as variations in the light intensity measured by the detector.

Intensity modulated sensors have been presented with performance comparable to the Fabry-Perot sensors mentioned above as well as sub-mm sensor diameters [24-26]. However, like the Fabry-Perot sensors, the key drawback with these intensity modulating sensors is the inability to achieve sensor multiplexing and multi-parameter sensing.

In-fibre Bragg gratings (FBGs) are an attractive alternative to the FOSs discussed above, as well as piezoelectric, resistive or other semiconductor sensing technologies, because they posses the key characteristics of other FOSs: small size (typically 125 μm in diameter), mechanical compliance, chemical inertness, resistance to corrosive environments and immunity to electromagnetic interference. Unlike the other FOS types, FBGs are capable of simultaneous multi-parameter sensing when suitably configured [18]. Multiple FBG sensors can be multiplexed along a single optical fibre thereby allowing spatially distributed measurements [27]. These intrinsic qualities also make FBGs attractive for medical pressure measurement applications; mainly because there is potential to create multi-parameter and minimally invasive sensors that address the limitations of current miniature sensors [1].

1.2.3 In-fibre Bragg gratings

As shown in Figure 1.3a, a FBG is typically formed within the core of a single-mode optical fibre [27]. The grating consists of a series of regions of increased refractive index, n, spaced at a regular period, Λ, over a finite length of the fibre core; usually between 2 mm and 10 mm in sensing applications. The regions of increased refractive index, Δn, are formed by exposing the Germania-doped fibre core to intense ultraviolet light at regular intervals of period Λ [28].

When light spanning a broad range of wavelengths (Figure 1.3a) encounters the Bragg grating a single narrow spectrum of wavelengths is reflected. This reflected spectrum is symmetric about the Bragg wavelength, λ_B (Figure 1.3a and 1.3b) which can be calculated using the grating period, Λ, and the refractive index of the fibre core, n_o, using the following relation derived from coupled-mode theory [27]:

$$\lambda_B = 2\Lambda n_o \tag{1}$$

The maximum reflectivity, R_{MAX} (Figure 1.3b), of the Bragg grating can be calculated using the length of the grating, Lg, and Δn for a given Bragg wavelength as [27]:

$$R_{MAX}\left(\lambda_B, \mathrm{Lg}\right) = \tanh^2\left[\pi\left(\frac{\Delta n}{2n_0}\right)\left(\frac{\mathrm{Lg}}{\Lambda}\right)\right] \tag{2}$$

Whereas the linewidth, $\Delta\lambda_W$, of the reflected spectrum (Figure 1.3b) is given by [27]:

$$\Delta\lambda_W = 2\lambda_B\sqrt{\left(\frac{\Lambda}{Lg}\right)^2 + \left(\frac{\Delta n}{2n_0}\right)^2} \tag{3}$$

The remaining light, that is not reflected, is transmitted past the Bragg grating and can be used to illuminate subsequent FBGs that are designed to reflect a different Bragg wavelength than the first Bragg grating. These subsequent gratings can be designed to reflect distinct Bragg wavelengths by ensuring that the grating period, Λ, is different in each grating.

FBGs can be used as sensors by measuring changes in the Bragg wavelength, $\Delta\lambda_B$, that result from changes in the measurand. For example, as shown in Figure 1.1a, tractions, T, applied to the optical fibre result in strain within the FBG that will cause a predictable change in the Bragg wavelength (Figure 1.3b). The change in the

Bragg wavelength can be predicted from the principal strains, ε_z, ε_x, ε_y, shown in Figure 1.1a, as:

$$\frac{\Delta\lambda_B}{\lambda_B} = \varepsilon_z - \frac{n_o^2}{2}\left[p_{zz}\varepsilon_z + p_{zx}\varepsilon_x + p_{zy}\varepsilon_y \right] \quad (4)$$

The coefficients, p_{zz}, p_{zy}, p_{zx}, are positive valued photo-elastic constants [27] that relate strain magnitude to changes in the fibre-core index of refraction. If the strains are known functions of the applied tractions, T, the ratio of changes in the Bragg wavelength to changes in the tractions, $\Delta\lambda_B / \Delta T$, can be predicted [27]. When the strains along the grating are uniform, the changes in λ_B will resemble those shown in Figure 1.1b, where the maximum reflectivity and full-width at half maximum (FWHM) of the spectra remain constant [27]. If strains along the grating are not uniform, changes in the Bragg wavelength can be accompanied by reductions in the maximum reflectivity as well as increased FWHM. Methods to predict changes in the FWHM and maximum reflectivity are discussed in Appendix A.

As outlined in the above example, sensing with FBGs can be achieved by measuring Bragg wavelength changes that are caused by strains along the grating. These strains can be created by many physical parameters including displacement [29], strain [3], temperature [30], humidity [31], and pressure [30].

1.3 Accuracy, uncertainty, repeatability, resolution and specificity

As will be discussed in subsequent sections and in the Appendices, there are various methods of measuring Bragg wavelength variations that result from varying pressure. Each method is subject to errors that affect the overall ability to measure

pressure. Before these discussions begin, the relevant metrics of measurement performance are defined:

1. Accuracy: the difference between the measured value and the true value of the measurand [32].
2. Uncertainty: a calculated quantity corresponding to the first standard deviation in repeated measurements of the measurand [33]. In this thesis, all measurements are assumed to be randomly distributed (Gaussian distribution) about the true value.
3. Repeatability: the smallest detectable difference in the measurand that can be measured on successive measurements [32].
4. Specificity: the ability of a measurement device to respond only to the measurand of interest [34].

Accuracy is achieved by calibrating sensors using reference pressure sensors that themselves have excellent accuracy. To achieve long-term accuracy, the sensor system must be comprised of components that maintain their respective calibrations. Increases in repeatability are achieved with sensor systems that are capable of detecting increasingly small variations in wavelength. For the biomedical pressure measurement applications considered in this thesis, sensor systems with increased pressure measurement repeatability are required for the reasons outlined in the next section. Specificity of pressure measurements, in the work presented in this thesis, was achieved by maintaining isothermal experiment conditions as well as isolating sensors from extraneous loads.

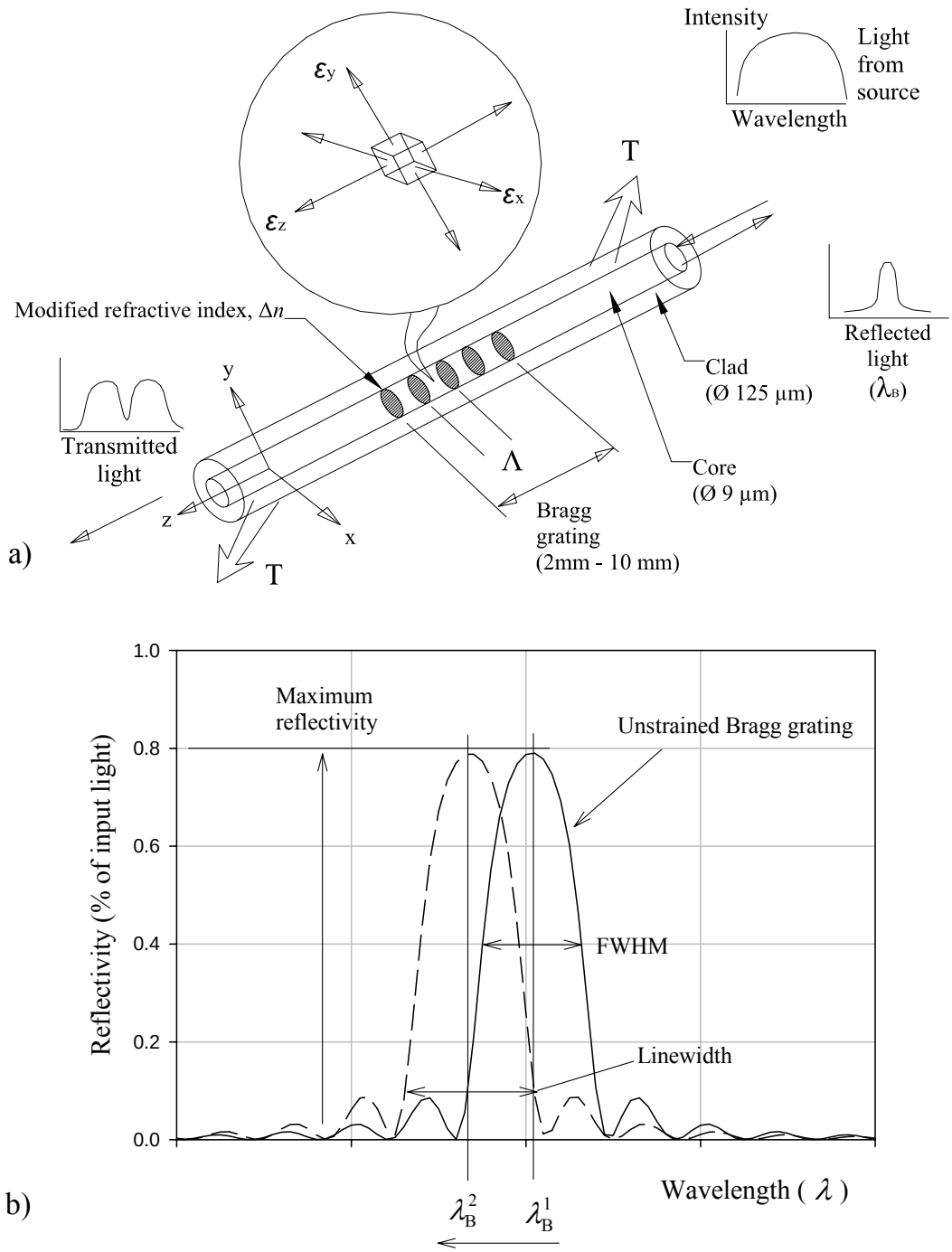

Figure 1.3: a) schematic showing features of optical fibre including the core, clad and Bragg grating. When light spanning a broad range of wavelengths encounters the Bragg grating, a single narrow spectrum of wavelengths centered at the Bragg wavelength, λ_B, is reflected while remaining light is transmitted. Tractions, T, applied to the fibre result in strains, $\varepsilon_z, \varepsilon_x, \varepsilon_y$, within the optical fibre; and b) when the Bragg grating experiences uniform strains there is a predictable shift in λ_B while the maximum reflectivity and full-width at half maximum (FWHM) remain constant.

1.4 Limitations of current FBG pressure sensors and interrogation schemes

Although bare-FBGs, similar to that shown in Figure 1.3, possess the key characteristics of FOSs, they also possess poor sensitivity to hydrostatic fluid pressure and are only suitable for pressure measurements over several MPa. For example, the sensitivity to pressure, typically expressed in terms of wavelength shift versus change in applied pressure (*e.g.* pico-meters (pm) per MPa), of a typical FBG is approximately -3.1 pm/MPa and is a constant over a range of tens of MPa [30]. Wavelength changes are typically measured using interferometers or optical spectrum analyzers [35] that have wavelength measurement repeatabilities of, at best, approximately ± 1.5 pm at measurement rates of up to 2 Hz [29]. An estimate of the pressure measurement repeatability of ± 0.5 MPa can be calculated [35] by dividing the wavelength measurement repeatability (*i.e.* ± 1.5 pm) by the pressure sensitivity (*i.e.* -3.1 pm/MPa). This level of repeatability is not appropriate for any biomedical pressure measurement applications including those described in Section 1.1.

Improvements to the pressure measurement repeatability are achieved by either designing new instruments capable of highly repeatable wavelength measurements or designing new FBG sensors that have intrinsically higher sensitivity to pressure. As a group, instrumentation schemes used to convert wavelength shifts to measurements of physical parameters are called *interrogation schemes*. The interrogation schemes can be classified into three main categories: scanning spectral filters with broadband light sources [36], scanning narrowband lasers [2] and fixed filters [37, 38]. Figure 1.4 shows the general layout of these three main interrogation schemes.

Interrogation schemes based on scanning spectral filters or narrow band scanning light sources can take many forms but they all operate on a single principle: conversion of variations in the Bragg wavelength to variations in light intensity that are measured versus time by intensity detectors. For example, as shown in Figure 1.4a, light leaving the broadband source is directed into a coupler and then into the FBG sensor. The FBG sensor reflects a single narrow spectrum centered on the Bragg wavelength based on the magnitude of the measurand, x. This narrow spectrum is directed into the scanning filter that transmits light only at a given wavelength. The scanning filter repeatedly scans over a range of wavelengths ($\lambda(t)$ in Figure 1.4a) and the intensity detector measures the transmitted light intensity versus time. The time of the peak intensity, t(x), can then be used to calculate the Bragg wavelength of the sensor using the transmission wavelength, $\lambda(t)$, of the scanning filter.

The method by which filters convert wavelength changes to intensity changes is described using Figure 1.5. Figure 1.5a shows an example spectrum from a FBG-sensor (in black) and a reflection spectrum from a scanning filter (light grey). As the filter scans through a pre-determined range of wavelengths during a given time (shown by $\lambda(t)$ in Figure 1.4a and 1.5a) there is an envelope in the intensity versus wavelength plot where the filter spectrum and FBG spectrum intersect (dark grey). The amount of light contained within this envelope is the amount of light that is transmitted through the filter. This light can be measured, using intensity detectors, as a function of time as shown at right in Figure 1.4a. As mentioned previously, the Bragg wavelength of the FBG for a given magnitude of the measurand, x, can then be calculated by converting the time at the peak detector output (Figure 1.4a) to wavelength using the function $\lambda(t)$.

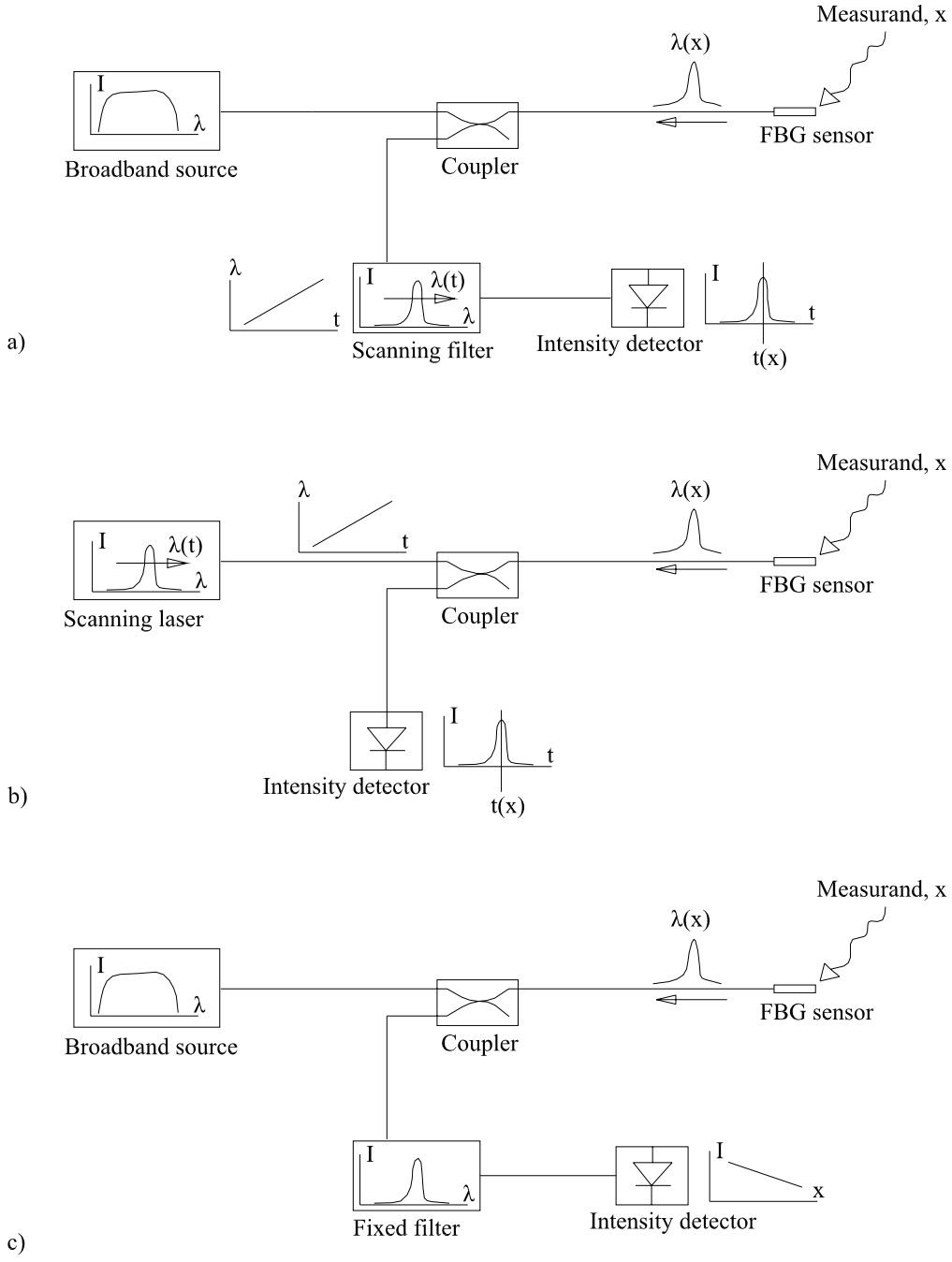

Figure 1.4: Schematics showing a) scanning filter, b) scanning narrowband laser, and c) fixed filter based interrogation schemes.

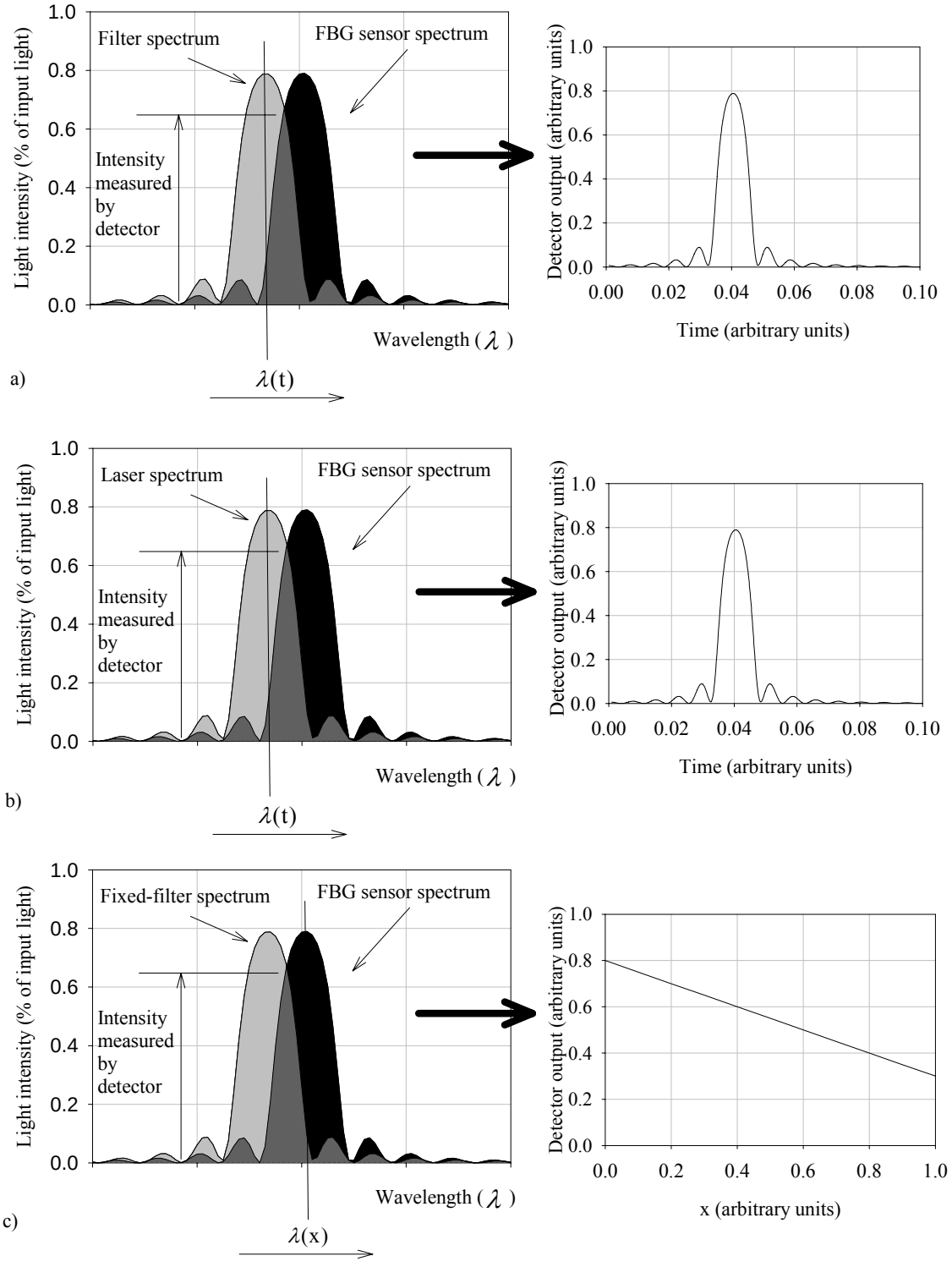

Figure 1.5: reflection spectra from: a) filter and FBG, b) laser and FBG, and c) fixed-filter and FBG. Shown to right of a), b) and c) intensity detector outputs for the various interrogation schemes.

Scanning lasers (Figure 1.4b) can also be used to measure the Bragg wavelength of a FBG-sensor in a similar manner. In this case the intersection of the laser spectrum and FBG spectrum (Figure 1.5b) is measured, through time, using the intensity detectors.

Scanning filters and scanning laser systems are typically more expensive than fixed filters, especially when used with multiplexed or multi-parameter sensors [38]. Both optical spectrum analyzers and interferometers belong to the scanning spectral filter category. The wavelength measurement repeatability (± 1.5 pm) stated earlier was for typical laboratory instruments. Instruments with improved repeatability exist, but can only be acquired at prohibitive costs. The increased cost is accrued because these instruments have high-performance scanning mechanisms that are extremely repeatable and have extremely uniform (through time) scan rates [27]. With more FBG sensors, the range of wavelengths scanned increases which necessitates even higher performance lasers/filters, which adds further to system cost [27]. Conversely, fixed filter interrogation is the lowest cost alternative, has the greatest frequency bandwidth (up to MHz) thereby allowing extremely rapid measurements, and is easily implemented with multi-parameter or multiplexed sensors [38].

An example of a fixed filter interrogation scheme is shown in Figure 1.4c. When the FBG is illuminated using broadband light, the narrow spectrum reflected by the FBG sensor is directed into the fixed filter that is designed to transmit light at a specific wavelength. As shown in Figure 1.5c, the spectrum of the fixed filter is set to partially overlap with the reflected spectrum of the Bragg grating. As the Bragg wavelength varies with changes in the measurand, denoted by $\lambda(\mathrm{x})$, the amount of light captured in the

intersection varies. The variations of the intensity detector output can then be measured as a function of the measurand, x, as shown at the right of Figure 1.4c.

Increased resolution, compared to optical spectrum analyzers, is achieved by using filters that cause large variations in the amount of light in the intersection for a given wavelength shift, $\lambda(x)$. Fixed filter schemes have been reported that can detect wavelength shifts 100 times smaller than typical optical spectrum analyzers [2].

Although pressure measurement repeatability can be improved with high repeatability interrogation schemes alone, FBG sensor systems that achieve repeatabilities appropriate for biomedical applications must also have FBG sensors with increased pressure sensitivity. By increasing the Bragg wavelength shift, $\Delta\lambda_B$, for a given applied pressure, ΔP, the pressure sensitivity increased. If the pressure sensitivity is increased enough, the limitation on wavelength measurement repeatability can be become insignificant relative to the wavelength shift caused by variation in pressure.

Numerous FBG sensor designs have been reported that achieve increased sensitivity through mechanical amplification of pressures applied to the FBG. These designs can take many forms, including pressure diaphragms with cross-sectional area greater than that of the bare-fibre [39] and, more commonly, polymer coated FBGs [40-42] as shown schematically in Figure 1.6.

The polymer coatings on these sensors are formed with diameter, Dp, so large that the material properties of the optical-fibre can be neglected when calculating the pressure induced strain in the sensor [43]. The axial strain, ε_z, is then a function of the applied pressure, P, the Poisson ratio, ν_p, and the Young's modulus of the polymer, E_p [44]:

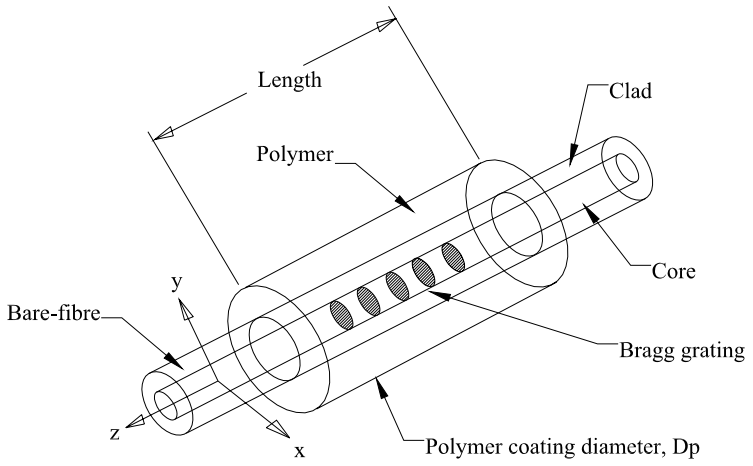

Figure 1.6: schematic showing bare-fibre and polymer coated FBG.

$$\varepsilon_z = \frac{(1-2\nu_p)P}{E_p} \tag{5}$$

For a bare-FBG the pressure-induced axial strain is given by a similar Equation, but the material properties in Equation 5 are replaced by those of the bare-FBG, ν_{FBG} and $E_{FBG,}$ respectively. The strain amplification relative to the case of a bare-FBG can be calculated as the ratio of the axial strain in the polymer coated sensor and the strain in the bare-FBG. To ensure significant strain amplification these sensors are constructed using polymers with Young's modulii much smaller, of the order kPa, than that of a optical-fibre (*i.e.* 70 GPa [27]). Sheng *et al.* (2004) and Zhang *et al.* (2001) have reported on sensors with pressure sensitivities 10,900 and 1,720 times greater than a bare-FBG with sensors that are 22 mm and 13 mm in diameter, respectively [44, 45].

In the context of biomedical pressure measurement applications these sensors have major diameters that are much too large for *in vivo* applications and could therefore have limited utility in *ex vivo* experiments as well. Moreover, sensors of this design do not retain the advantages offered by FBGs, especially small size. To date, no researchers

have presented FBG sensors that have both increased pressure sensitivity and major diameters below 1 mm. If multi-parameter FBG sensors are to be developed for biomedical applications, sensors that have both increased sensitivity and sub-mm diameters must first be developed.

1.5 Thesis objectives

The objective of this work is to develop FBG-based pressure sensors that have increased sensitivity to hydrostatic pressure relative to the case of a bare-FBG, major diameters smaller than 1 mm, and that are mechanically compliant.

1.6 Methods

The objectives of this thesis were fulfilled with the development of two FBG-based pressure sensors. The first FBG sensor (hereafter the IVD pressure sensor) has a major diameter of only 400 μm and pressure sensitivity 7-times greater than that of a bare-FBG. The IVD sensor was used for pressure measurements within porcine (pig) IVDs at the Division of Orthopaedic Engineering Research at UBC, and the results obtained were validated using the current standard strain-gauge sensors. Moreover, when the IVD sensor was applied within IVDs of small disc height it did not interfere with vertebral features, unlike the strain-gage sensors. Finally, the results obtained also suggested that the IVD sensor altered disc mechanics less than the strain-gage sensors.

The second FBG sensor (hereafter the Etched sensor) was constructed with a major diameter of only 200 μm and had pressure sensitivity 20-times greater than that of a bare-FBG. Calibration results obtained from this sensor show that it has appropriate repeatability for measurements ranging over kPa.

1.7 Thesis organization

The work and contributions of this thesis are presented in three manuscripts that are contained in the appendices:

1. **Dennison, CR**, Wild, PM, Wilson, DR, and Cripton, PA, 2008, A minimally invasive in-fibre Bragg grating sensor for intervertebral disc pressure measurements, Measurement Science and Technology, (IN PRESS)
2. **Dennison, CR**, Wild, PM, Dvorak, MFS, Wilson, DR, and Cripton, PA, 2008, Validation of a novel minimally invasive intervertebral disc pressure sensor utilizing in-fibre Bragg gratings in a porcine model: An *ex vivo* study, Spine (IN-PRESS)
3. **Dennison, CR**, and Wild, PM, 2008, Enhanced sensitivity of an in-fibre Bragg grating pressure sensor achieved through fibre diameter reduction, submitted to Measurement Science and Technology, June 2008.

The author conducted all experimental work including sensor construction, calibration and IVD pressure measurements, described in these manuscripts. Sensor modeling, described in manuscripts one and three, was also performed by the author. The majority of each manuscript was written by the author.

The manuscripts are contained in appendices A, B and C, respectively. The body of this thesis contains three chapters, 2 through 4, which describe the key contributions, methods and significant findings of each manuscript. Chapter 5 presents conclusions and future work.

1.8 Other publications

A number of other publications have resulted from application of the IVD sensor in further IVD and other biomechanics studies.

Refereed journal papers:

1. **Dennison, CR**, Wild, PM, Byrnes, PWG, Saari, A, Itshayek, E, Wilson, DC, Zhu, QA, Dvorak, MFS, Cripton, PA, and Wilson, DR, 2008, "*Ex vivo* measurement of lumbar intervertebral disc pressure using fibre-Bragg gratings," Journal of Biomechanics, 41(1), pp. 221-225.

Refereed conference publications: (reverse chronological)

1. Jones, CF, Kwon, BK, **Dennison, C**, Wild, P, Markez, J, and Cripton, PA, A large animal model to measure cerebrospinal fluid pressures associated with spinal cord injury: development and preliminary results, submitted to NWBS 2008, Boise State Univ.
2. Jones, CF, Kwon, BK, Itshayek E, Markez, J, **Dennison, C**, Singlehurst, D, Wild, P, and Cripton, PA, Development and pilot results from a large animal study to measure cerebrospinal fluid pressure before, during and after spinal cord injury, accepted for podium, 4th Annual Injury Biomechanics Symposium, May 2008, Ohio State Univ.
3. Saari, A, **Dennison, C**, Wild, P, Dvorak, MFS, Wilson, D, and Cripton, PA, Intervertebral disc pressure measurements: Influence of disc thickness on disc pressure during lateral bending, presented to the World Forum for Spine Research, Kyoto, Jan. 2008.

4. **Dennison, C**, Saari, A, Wild, P, Dvorak, MFS, Wilson, D, and Cripton PA, Ex vivo measurement of porcine intervertebral disc pressure during compression and lateral bending using a novel in-fibre Bragg grating sensor, presented to the World Forum for Spine Research, Kyoto, Jan. 2008.

5. **Dennison C**, Saari, A, Wild, P, Dvorak, MFS, Wilson, D, and Cripton, PA, Comparison of intervertebral disc pressure measurements made with fibre-Bragg gratings to those made with a contemporary needle mounted sensor *ex vivo*, presented to the 54th Annual Meeting of the Orthopaedic Research Society Sept. 2007.

6. Saari, A, **Dennison, C**, Wild, P, Dvorak, MFS, Wilson, D, and Cripton, PA, Intervertebral disc pressure during lateral bending, presented at the 54th Annual Meeting of the Orthopaedic Research Society Sept. 2007.

7. Wild, P, **Dennison, C**, Wilson, D, and Cripton, PA, Accuracy of disc pressure measurements using a new in-fibre Bragg grating sensor, 53rd Annual Meeting: Orthopaedic Research Society, San Diego, CA, February 2007.

8. Wild, P, **Dennison, C**, Wilson, DC, Zhu, QA, Byrnes, PWGB, Cripton, PA, and Wilson, DR, Measurement of Lumbar Disc Pressure using Fibre Bragg Gratings, Orthopaedic Research Society 52nd Annual Meeting, Chicago, February 2006.

Journal paper 1 describes application of bare-FBG pressure sensors to IVD pressure measurement. The work described in this paper essentially establishes the feasibility of implanting FBGs in IVDs and conducting pressure measurements. The author conducted the experiments and wrote the majority of the paper, including the revisions.

Conference publications 1 and 2 describe another application of the IVD pressure sensor, this time to measurements of cerebrospinal fluid pressure both before and after simulated impacts to the spinal cord. The author assisted in sensor construction and calibration and also helped conduct pressure measurements in the cerebrospinal fluid. The author also assisted in interpreting the results of these studies.

Conference publications 3 through 8 describe various experiments related to the validation of the IVD pressure sensor. In all cases, the author was either the principal experimenter, or assisted in experiments. The author also helped write and edit these publications.

The designs of the IVD and Etched sensor are also protected by two patents as indicated below.

1. Dennison, C. and P. Wild, Pressure sensor for Biological fluids and use thereof, US PCT No. 070213 (IVD sensor)

2. Wild, P., and C. Dennison, Micron scale pressure sensors and use thereof, US patent filed May, 2008.

Chapter 2

Intervertebral disc pressure sensor (IVD sensor)

The design and modeling of the FBG-based IVD sensor are discussed in this chapter. An overview of our previous attempts at measuring IVD pressure with bare-FBG sensors is presented first, to give historical context and establish the need for the new IVD sensor. The complete manuscript containing the discussions outlined in this chapter is included as Appendix A.

2.2 Background: measurements of IVD pressure using bare-FBGs

The mechanical structure of the spine consists of bone vertebrae separated by intervertebral discs (IVDs). Figure 2.1a shows a motion segment of the spine including both a superior (upper) and inferior (lower) vertebra separated by the IVD as well as the bone processes on the posterior of the spine that articulate at the facet joints (Figure 2.1a). To allow application of forces and moments to the motion segment, in *ex vivo* studies, the vertebrae of the motion segment are commonly encased in dental stone (Figure 2.1b). The dental stone fixtures are then secured to materials testing machines, and the entire assembly of the motion segment and the dental stone is called a functional spine unit (FSU). When the spine and, therefore, the motion segment are loaded in compression (Figure 2.1b) the vertical distance between the vertebrae is reduced, thereby reducing the IVD height from its nominal unloaded height (Figure 2.1b). When the IVD height is reduced, there is a corresponding increase in the hydrostatic pressure in the semi-fluid region in the center of the IVD, termed the nucleus pulposus (Figure 2.1c). The nucleus pressure is exerted on both the superior and inferior vertebra and on the

lateral annulus (Figure 2.1c), thereby resulting in equilibrium of loads. In healthy lumbar discs, nucleus pressure increases linearly with applied compressive load (Figure 2.2).

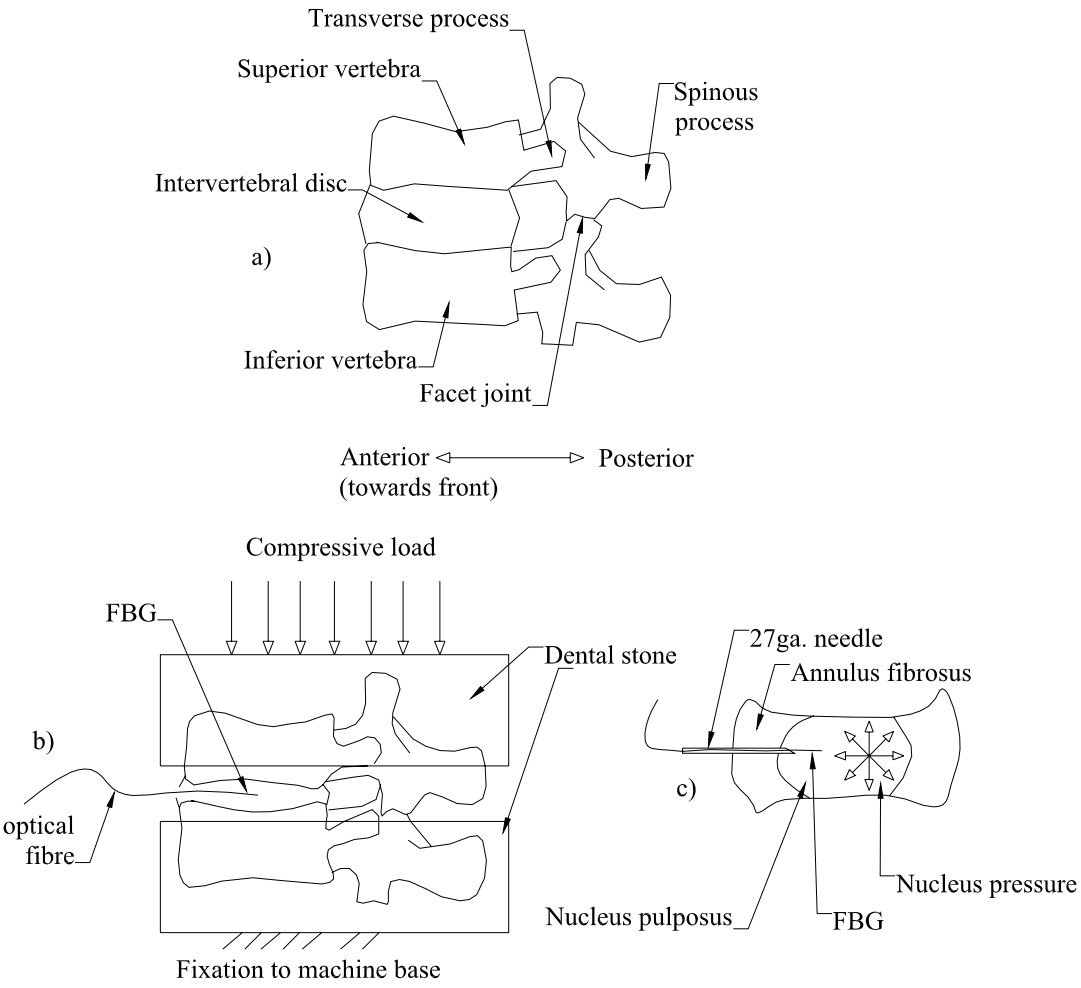

Figure 2.1: a) schematic of motion segment of human spine; b) motion spine with vertebra embedded in dental stone and generic sensor inserted into disc, this assembly is termed a functional spine unit (FSU); and c) hydrostatic pressure created within nucleus of IVD, as a result of compressive load. Bare-FBG sensor inserted through 27ga. hypodermic needle into the center of the nucleus.

In an attempt to establish the feasibility of implanting FBGs within IVDs, pressure measurements were conducted in five human cadaveric specimens using bare-FBGs and the current standard strain-gauge sensors. The results obtained from the bare-

FBG were compared to those presented in previous IVD pressure studies and those obtained from strain-gauge sensors [16].

The bare-FBGs (10 mm length, λ_B of 1550 nm, Blue Road Research, Gresham OR) were calibrated to measure hydrostatic pressure over a 0 MPa to 3 MPa range and were found to have a sensitivity of -5.7 pm/MPa [16]. The FBG insertion process started by first inserting a 27ga. hypodermic needle through the outer annulus and into the nucleus space (Figure 2.1c). The FBG was then inserted into the bore of the needle, and advanced through it until the FBG was located at the approximate center of the nucleus (Figure 2.1b and 2.1c). Compressive loads were then applied (Figure 2.1b) from 0 N to 2000 N to 0 N at 200 N/s; these loads are typical of those presented in the literature [11, 14, 16]. Pressure was measured as a function of applied compressive load using the pre-calibrated bare-FBGs and an optical spectrum analyzer (OSA, Ando AQ6331, Tokyo, Japan). Strain-gauge sensors were also implanted and used to measure IVD pressure in a manner identical to that described in the literature [11, 16].

Although the results (Figure 2.2) agreed with results published in previous disc pressure studies [10, 11, 13, 46] and established that IVD pressure measurement with FBGs was feasible, they also outlined key limitations with the bare-FBG sensors. First, as shown by the error bars in Figure 2.2a, there was significant uncertainty in FBG pressure measurements, partly because pressure measurements were calculated based on wavelength measurements using the OSA. The error bars shown in Figure 2.2a were calculated, using linear-regression, based on the wavelength measurement repeatability of the OSA and the load-cell of the materials testing machine [16]. As discussed in Section 1.4, converting wavelength measurements to pressure can result in poor repeatability over

the pressure ranges experienced in the IVD. Improving the repeatability of pressure measurement is a crucial step in developing FBG sensors capable of resolving subtle pressure variations that may result from various factors affecting disc mechanics.

Another key limitation in this study was the lack of agreement between the bare-FBG-measured (Figure 2.2a) and strain-gauge-measured (Figure 2.2b) IVD pressure [16]. Part of the lack of agreement was attributed to degenerated discs that had inhomogeneous nucleus composition. It was hypothesized that the inhomogeneity could have included solid inclusions in the nucleus that had sizes comparable to that of the bare-FBG sensing length (10 mm). These solid inclusions could have caused non-hydrostatic (*i.e.* directional) pressure within the nucleus. Pressure measurements from the bare-FBG could have had poor accuracy because the bare-FBGs were only calibrated for hydrostatic pressure. To be able to test this hypothesis further, a FBG sensor with a smaller sensing area was required. By limiting pressure measurements to a small sensing area, variations in the pressure throughout the nucleus (caused by inhomogeneity) can be mapped.

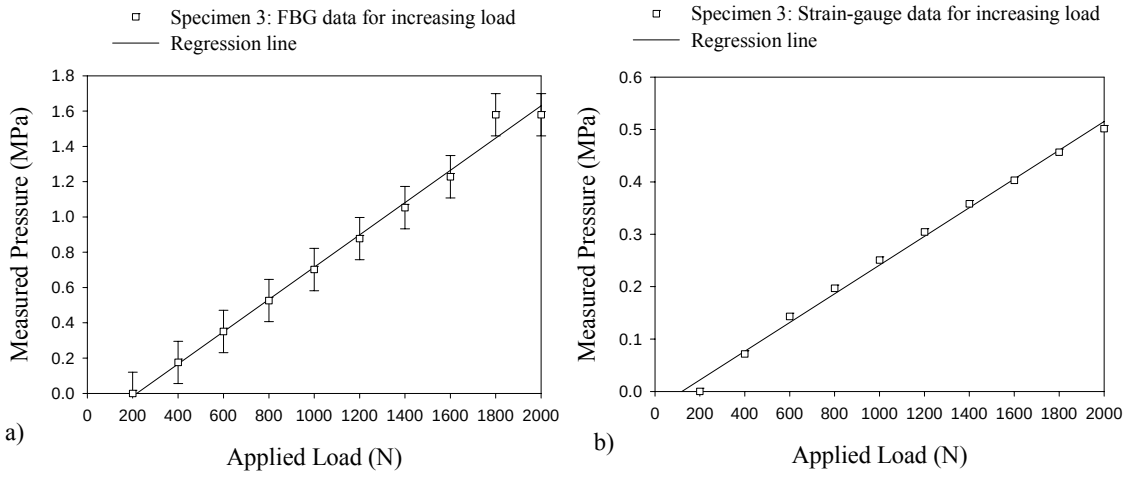

Figure 2.2: a) typical pressure versus compressive load data obtained using bare-FBG; and b) typical data obtained using the strain-gauge sensor [16].

The final limitation of the bare-FBG sensor was poor spatial resolution. Because the effective sensing length of the bare-FBG was 10 mm (*i.e.* the length of the grating) spatial pressure variations over length scales smaller than 10 mm could not be resolved. It is crucial to improve the spatial resolution by reducing the size of the sensing region because current research topics in spine biomechanics rely heavily on data from pressure profilometry within the nucleus [15, 47].

2.2 The IVD pressure sensor

The design of the IVD pressure sensor is shown in Figure 2a and 2b in Appendix A. Hereafter a figure naming convention following the format Figure A2a will be used in reference to Figure 2a in Appendix A, for example. The FBG sensor is comprised of a single-mode optical fibre (Dow Corning SMF-28, Midland MI) housed within a length of stainless steel hypodermic tube (0.4 mm outside diameter and 0.1 mm wall thickness). The fibre is positioned such that it is coaxial with the hypodermic tube and such that its tip is flush with the (inserted) right hand end of the hypodermic tube. A Bragg grating (Blue Road Research, Gresham OR, 10 mm length) is etched into the core of the fibre and is positioned at the right hand end of the fibre. The annular volume between the inside diameter of the hypodermic tube and the outside diameter of the optical fibre is filled with a compliant silicone sealant (Dow Corning 3140 RTV, Midland MI). The silicone is bonded to the inner surface of the hypodermic tube and to the outer surface of the fibre. The *sensing region* of the sensor consists of the exposed surfaces of silicone sealant and optical fibre at the right hand end of the tube and has an area of only 0.03 mm^2. At the left hand end, the hypodermic tube is gripped in a modified optical fibre patch-chord connector within which a connection is made to an optical patch cord. The

length of tube that extends from the fitting is called the *probe*. In the current sensor, the probe is 50 mm in length but the sensor can be constructed with any probe length. The optical patch cord connects to the interrogation system for the sensor.

When the probe of the IVD sensor is exposed to hydrostatic pressure, the pressure acts on the cylindrical outer surface of the hypodermic tube and on the sensing region (Figure A2a and A2b). Relative to the silicone, the tube is rigid and, therefore, shields the optical fibre from the effects of the pressure on the outer cylindrical surface of the tube. The pressure applied to the sensing region causes strains in the silicone sealant and the FBG. Because the FBG is housed within the hypodermic and shielded from pressure along its circumferential surface, the greatest strains along the FBG are compressive and in the z-direction (Figure 1.3a), thereby resulting in large axial strains, ε_z (Figure A9) relative to the transverse strains, ε_x and ε_y (Figure A9). As discussed in Chapter 1 and as shown by Equation 4, pressure-induced strains in the FBG induce changes in its Bragg wavelength, λ_B, the characteristic wavelength of light that is reflected from a FBG [18].

By ensuring that the axial strains are large compared to the transverse strains, the pressure sensitivity is increased relative to the case of a bare-FBG. This can be understood by establishing the relative contributions to the Bragg wavelength shift as given by Equation 4. The first term on the right hand side of the equation is the axial strain, ε_z, therefore the wavelength shift, $\frac{\Delta\lambda_B}{\lambda_B}$ is directly proportional to the axial strain. The second term in Equation 4 relates strain to wavelength shift through the photo-elastic constants, p_{zz} and $p_{zx} = p_{xy}$, which have the values 0.252 and 0.113, respectively [27].

This second term is also pre-multiplied by $\frac{n_0^2}{2}$ which evaluates to 1.04 when n_o=1.44 [27]. Therefore, the contribution to the Bragg wavelength shift, given by this second term, is much smaller than that given by the axial strain because each strain term is pre-multiplied by either 0.252 or 0.113. Because the largest strains in the IVD sensor are axial strains and because axial strains have the greatest contribution to the wavelength shift (Equation 4), the IVD sensor has increased sensitivity as a direct result of shielding the FBG within the hypodermic tube.

2.3 IVD sensor modeling

In an effort to understand the strain-fields within the IVD sensor, as well as to predict the pressure sensitivity, $\Delta\lambda_B / \Delta P$, a combination structural finite-element and strain-optic model was developed. The complete description of this model is detailed in Section 3 of Appendix A, however the details are outlined here.

The structural finite-element model was implemented and solved using ANSYS® (ANSYS®, version 10, Canonsburg PA). Both nodal convergence and mesh independence were established before using the model to predict strains, $\varepsilon_z, \varepsilon_x, \varepsilon_y$ (relative to the coordinate system in Figure A3a), along the optical fibre.

Because the strains were predicted to linearly vary with position along the Bragg grating (Figure A4a) the strain-optic equations presented in Section 1.3, that are suitable only for uniform strains, could not be applied to predict shifts in the Bragg wavelength. Instead, the transfer-matrix formalism presented by Huang *et al.* (1995) was applied [48]. The details of its implementation are described fully in Appendix A.

2.4 Performance of the IVD pressure sensor

Experimental data in the form of Bragg wavelength versus applied hydrostatic pressure, ranging from 0 MPa to 3 MPa, was obtained using a purpose-built calibration apparatus. This experimental data was collected to allow validation of the FBG sensor finite-element/strain-optic model predicted sensor sensitivity.

The calibration apparatus was configured similarly to that described by Xu *et al.* (1993) [30] and included a broad C-band light source (AFC-BBS1550, Milpitas CA), a bi-directional 3 dB optical coupler (Blue Road Research, Gresham OR), an optical spectrum analyzer (OSA) (ANDO AQ6331, Tokyo JP), a purpose built pressure vessel and a reference pressure transducer (OMEGADyne PX01C1, Stamford CT, Acc.: 0.05% FS – 6.9 MPa).

The FBG sensor was inserted into the pressure vessel and sealed *via* a bulkhead fitting. Pressure was manually varied from 0 MPa to 3 MPa to 0 MPa (as reported by the reference transducer) using a manual hydraulic pump (ENERPAC P141, Milwaukee WI) while Bragg wavelength variations were recorded from the OSA. This procedure was repeated five times.

The finite-element strain-optic model (hereafter the model) predicted sensitivity to pressure, $\Delta\lambda_B / \Delta P$, was -23.9 pm/MPa, and the Bragg wavelength shift varied linearly (r^2=1.0) with applied pressure. The experimentally measured pressure sensitivity was found to be -21.5 pm/MPa and the measured variations in Bragg wavelength varied linearly (r^2=0.99) with applied pressure.

We also commissioned optical interrogation equipment designed to convert changes in Bragg wavelength to analogue voltages similar to that described in Nunes *et*

al. (2004) [37]. The *fixed filter demodulation technique* allows direct calibration of the FBG sensor in terms of analogue voltage versus pressure. This demodulation technique, and the calibration apparatus, was used to calibrate the FBG sensor from 0 MPa to 3 MPa. Analogue voltage versus applied pressure was acquired at 60 Hz and the average sensitivity of the sensor, and standard error in pressure measurement, was calculated from 10 calibration datasets acquired using hardware and software implemented in LabView© (Version 8, Austin TX).

2.5 IVD pressure measurements

The IVD sensor was validated against the strain-gauge sensor (shown in Figure A7) by performing pressure measurements within a cadaveric porcine (pig) FSU. Each sensor was inserted along three insertion axes, as shown in Figure A6, using a procedure similar to that described for the bare-FBG. The procedure is described in Section 3.5 of Appendix A.

The disc response to load (Figure A12 and Table A1 and A2) measured by the IVD sensor and strain-gauge sensor showed excellent agreement. The relative difference in the disc response to load, between the IVD and strain-gauge sensors, for insertion axes one through three respectively were 28.4%, 3.73%, and 1.98%. For the maximum measured pressure the relative differences were respectively 37.7%, 6.00%, and 1.99%. The large relative differences for insertion axis 1 were attributed to interference between the strain-gauge and the vertebra of the FSU. The effect of interference will be fully discussed in Chapter 3.

IVD pressure measurements performed using the FBG sensor also showed excellent repeatability (Table A1). For sensor insertions axes one through three,

respectively, the relative difference in the disc response to load between subsequent measurements was only 0.4%, 6.5%, and 1.0% with similar results for the maximum measured pressure.

2.6 Discussion

A key strength of this work is that the FBG sensor has a sensitivity (*i.e.* -21.5 pm/MPa) approximately 7 times greater than that of a bare-FBG sensor (-3.1 pm/MPa) while maintaining extremely small size (400 μm major diameter) and high spatial resolution by limiting the sensing region to the probe tip. This is an improvement relative to other FBG sensors presented in the literature that employ pressure amplification schemes that significantly increase their length or major diameter. Examples include the sensors described in Section 1.4 of this thesis.

This sensor is also smaller than all previously reported IVD pressure sensors of which the smallest had a 1.3mm diameter [49]. Therefore it has the potential to address the limitations associated with needle mounted sensors because of its small size and its mechanical compliance. Unlike the large (1.3 mm to 3 mm diameter) and rigid needle mounted sensors, the FBG sensor could be used in discs with small disc height such as in the cervical spine or in degenerated discs. In cervical spine specifically there is a paucity of experimental data; therefore there is potential contribute new understanding of the biomechanics in this less-studied region of the spine.

2.7 Summary

The IVD pressure measurement results presented established that the IVD sensor was capable of measuring pressure within IVDs. To establish that the IVD sensor

addressed the limitations of the bare-FBG and strain-gauge sensors an in-depth *ex vivo* study was necessary. This study is detailed in Chapter 3.

Chapter 3

Ex vivo validation of IVD sensor

This chapter discusses the disc pressure study designed to validate the IVD sensor for pressure measurements under various loading conditions on the FSU. The structure and methods of the validation study are briefly outlined. Results are then presented that establish the validity of the pressure measurements and suggest that the new IVD sensor impacts disc mechanics less than the current standard strain-gauge sensor. The complete manuscript containing the majority of the discussions outlined in this chapter is included as Appendix B.

3.1 Methods

Structure:

The main methods of the validation study consisted of IVD pressure measurements within the discs of porcine FSUs that were subjected to two different loading protocols. The first protocol (the compression protocol) was designed to establish the accuracy of the IVD sensor. Compressive loads were applied to the FSUs and disc pressure was measured using both the IVD and strain-gauge sensors. The accuracy of the IVD sensor was established by comparing IVD sensor measurements to those obtained using the strain-gauge sensors that are the widely accepted standard tool for disc pressure measurements [11, 17, 49] (shown in Figure B2). By establishing the accuracy of the IVD sensor relative to strain-gauge measurements, it is implied that the strain-gauge sensor measures the true pressure.

After validation in the compression protocol, the IVD sensor was then used to measure disc pressure resulting from applied lateral bending moments (the bending protocol). The results from the bending protocol were then compared to those in the literature to qualitatively validate the IVD sensor measurements. All experimental methods used were consistent with those published in the existing literature for disc pressure measurements for compression [14] and bending [50].

Cadaver material:

Six lumbar FSUs were prepared for the compression protocol, and nine more for the bending protocol. As described in Appendix B, the lumbar spine specimens were harvested fresh and were dissected of all muscle tissues. The spines were then segmented resulting in motion segments consisting of upper and lower vertebrae separated by an IVD. The posterior ligaments (Figure 3.1a) were left intact. The vertebrae of the motion segment were then encased in dental stone, as shown schematically in Figure 3.1b.

Sensor insertions:

As shown in Figure B3a and B3b, the sensors were inserted using a similar method to that already described for the bare-FBG experiments. Both the IVD and strain-gauge sensor insertions were randomized over three insertion locations (Figure B3b).

Loading:

A simple schematic of the FSU-loading geometry is shown in Figure 3.1. The compression protocol consisted of loads from 0N to 500N, with a one-second hold at 500 N, and then back to 0N, at a 40N/s loading rate for both loading and unloading phases. The bending protocol consisted of applied moments ranging from +3 Nm to -3 Nm and

the angular rate of displacement of the load-cell was controlled to be nominally 2 degrees per second with a continuous motion.

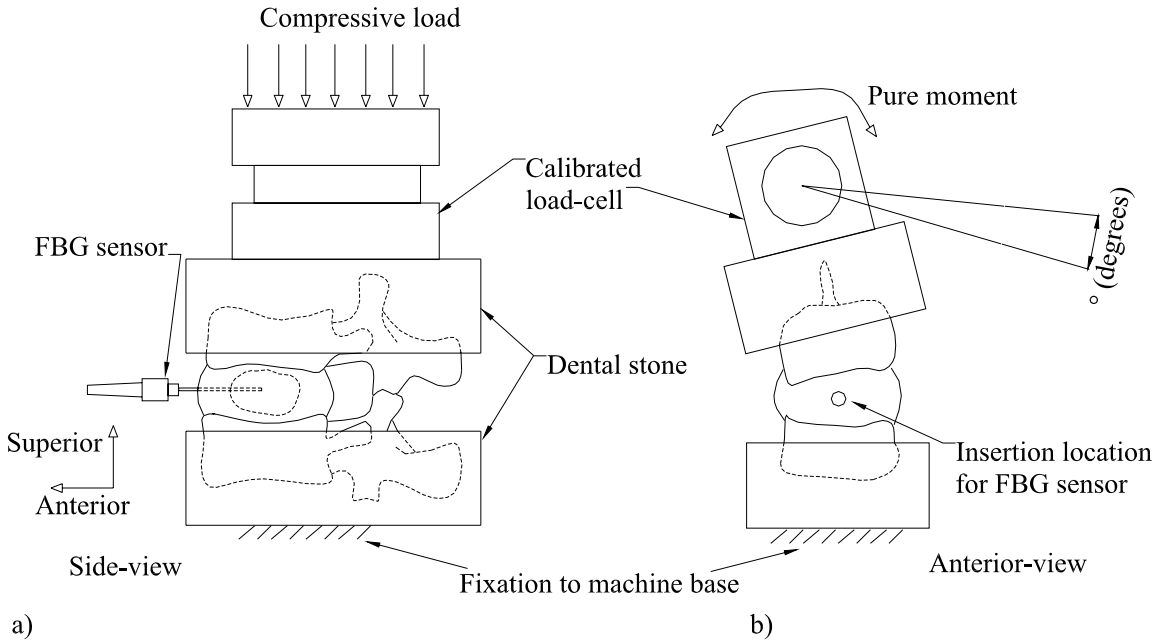

Figure 3.1: a) schematic of FSU and load application in compression protocol; and b) in bending protocol.

3.2 Compression protocol results and discussion

For both the IVD and strain-gauge sensors, disc pressure varied linearly with applied compressive load (Table B1 and B2). The mean coefficient of determination (r^2) for the IVD sensor data was 0.97 and ranged from 0.90 to 0.99, while for the strain-gauge sensor data the mean coefficient of determination was 0.99 with a range from 0.97 to 0.99. This finding is also consistent with data published by previous investigators [13, 14, 49].

In 50 % of all trials the strain-gauge sensor interfered with the upper and lower vertebra during application of compressive loads, as shown schematically in Figure 3.2a. Typical results for these trials are plotted in Figure 3.2b. In these trials, the mean

difference in the disc response to load (Table B2) was 21.4% and ranged from 9.06% to 28.4%, and for the maximum measured pressure (Figure 3.2b) the mean difference was 22.2% and ranged from 12.3% to 30.4% (Table B2).

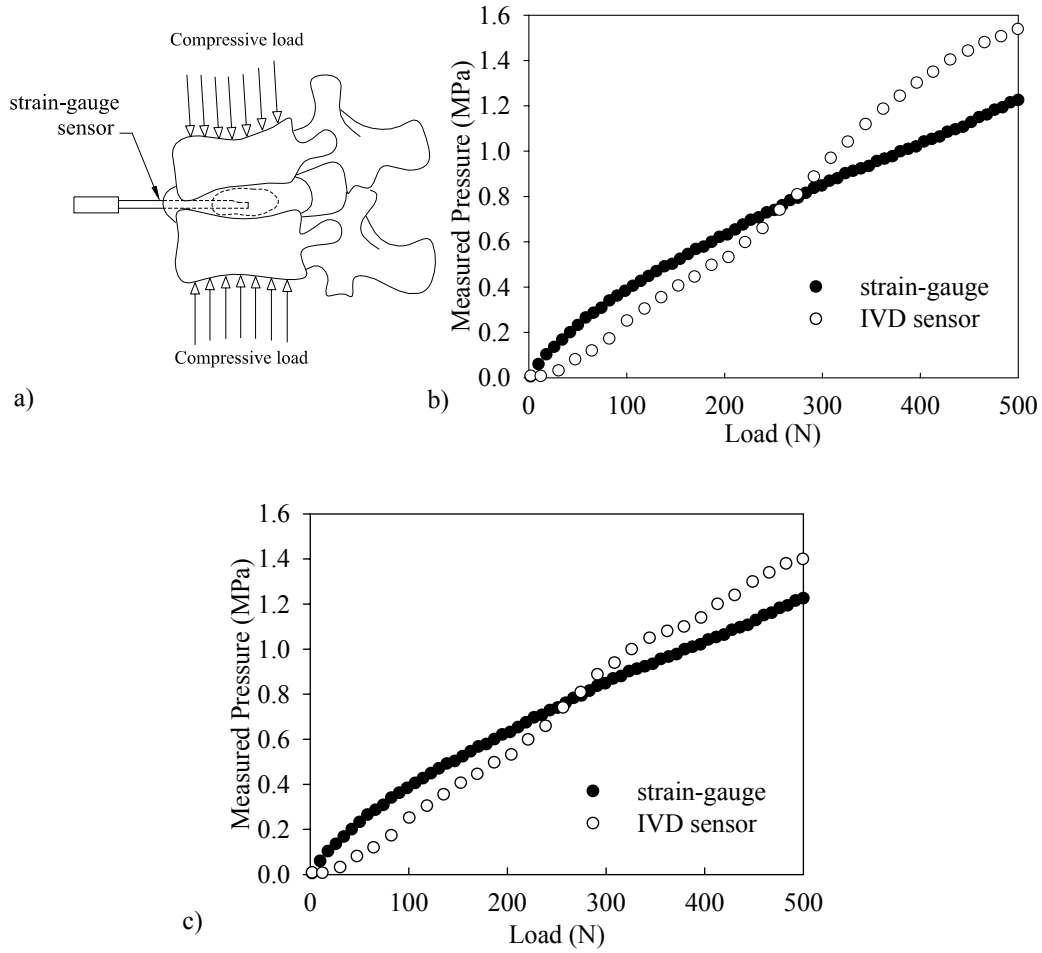

Figure 3.2: a) schematic showing interference of strain-gauge sensor and vertebra; b) typical pressure versus load results for the cases where interference occurred; and c) when it did not. Maximum measured pressure is measured pressure at 500 N. Disc response to load is the regression-calculated slope of pressure versus load data.

Typically, and as shown in Figure 3.2b, when the strain-gauge interfered with the vertebra it measured lower maximum pressures and disc response to load, as compared to the IVD sensor. We hypothesize that interference of the strain-gauge sensor with the vertebra could have caused load transmission through the strain-gauge sensor instead of

the IVD thereby resulting in reduced disc pressure. When interference did not occur, the strain-gauge and IVD sensor measurements showed excellent agreement. The mean relative difference between the disc response to load for the IVD sensor and strain-gauge sensor results was 9.39% and for the maximum measured pressure was 9.11%. We were the first group to obtain experimental data that suggested there is a quantifiable effect of sensor size on disc pressure. This effect has been suggested by previous investigators [12, 14, 16].

3.3 Bending protocol results and discussion

The results presented in this section are not included in the Appendix. They are however detailed in Refereed conference publication three (see Section 1.8) [51].

There was a difference in the variations of disc pressure versus applied moment when the results were suitably categorized based on disc geometry. As shown Figure 3.3a, each disc of each FSU had its disc height, H, and width, W, measured after experimentation was completed. A disc thickness metric was then calculated for each FSU, as the ratio H/W. The average value of thickness metric was 0.12 [51].

When the ratio H/W was greater than 0.12 the shape of the disc pressure versus applied moment profile resembled that shown in Figure 3.3c. As the magnitude of the applied moment increased, the magnitude of the measured pressure had a corresponding increase, and the profile was typically symmetric (Figure 3.3c). When the ratio H/W was less than 0.12 the shape of the disc pressure versus applied moment profile resembled that shown in Figure 3.3d. As the magnitude of the applied moment increased, the magnitude of the measured pressure had a corresponding decrease, and the profile was

typically symmetric (Figure 3.3d). Both of the profile shapes shown in Figure3.3 have been presented in the literature, for FSUs subjected to lateral bending [49, 50].

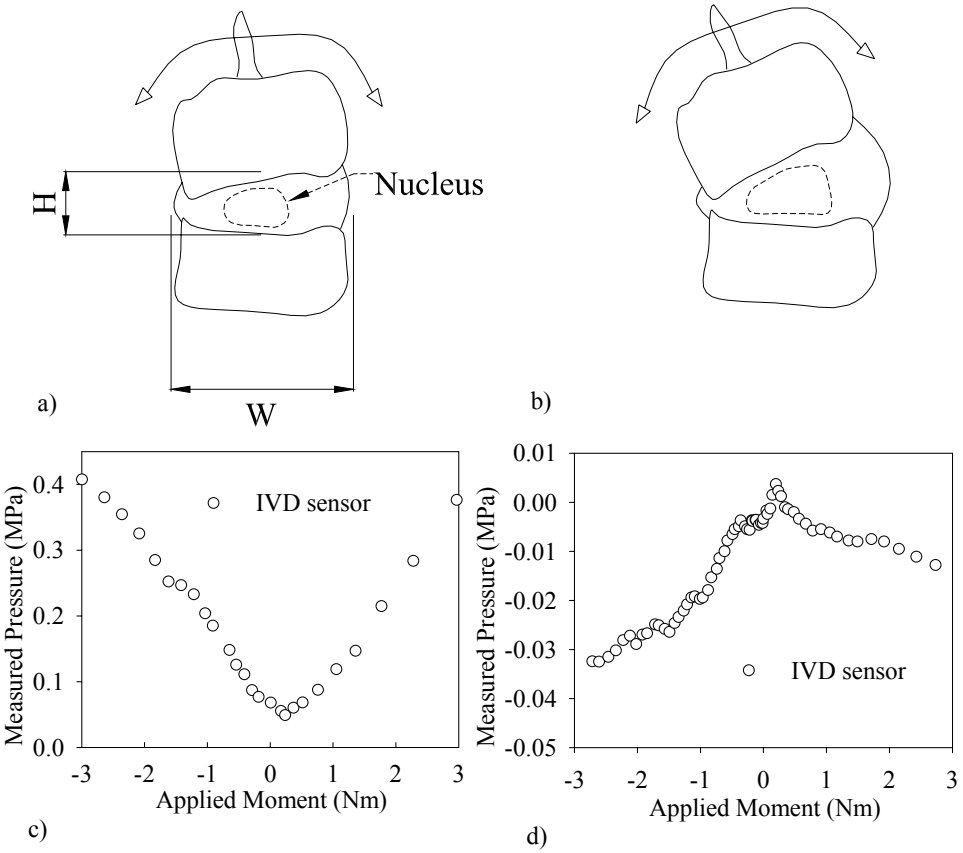

Figure 3.3: a) hypothesized disc deflection in relatively thick disc with H/W > 0.12; and b) for discs with H/W < 0.12; c) typical pressure versus moment profile for H/W > 0.12; and d) for H/W < 0.12.

However, to our knowledge we are the first to measure both profile shapes shown in Figure 3.3 in a single study. We hypothesize that that in discs with H/W > 0.12, because the disc is relatively thick the upper vertebra are free to rotate about an axis of rotation that is essentially static (Figure 3.3a). Conversely, in thinner discs we hypothesize that vertebral contact could occur (Figure 3.3b), resulting in a shift of the axis of rotation to the point of contact. In this scenario, the nucleus volume could potentially increase (Figure 3.3b) leading to pressure decreases (Figure 3.3d). Further

testing of these hypothesis remains for future work. In these future studies, disc displacements will be noted as a function of applied moment to allow experimental verification of these hypotheses.

3.4 Summary

The results of the validation study established the accuracy of the IVD sensor. When strain-gauge interference was not noted the IVD and strain-gauge measured pressures were comparable. The results also suggested that the IVD sensor was less invasive than the strain-gauge and that sensor size, and disc shape, are relevant to disc pressure magnitudes.

From the perspective of spine biomechanics researchers these results are exciting for various reasons. The development of the IVD sensor could equip researchers with a tool that does not alter mechanics to the same degree as the current strain-gauge sensors. A corollary to this is the potential to test historic pressure data obtained using past sensors, and therefore test the accepted understanding of spine biomechanics. There is also potential to make pressure measurements in discs that have, until now, had small discs heights that would not allow insertion of the strain-gauges. There is also potential to measure performance of corrective spine implants (*e.g.* fusion plates, artificial discs) which is a current area of intense research. All of these areas will be the focus of future research.

To allow pressure measurements in the remaining biomedical applications listed in Chapter 1 (*i.e.* cerebrospinal) a pressure sensor with further increased pressure sensitivity is required. The development of a new FBG sensor, the Etched sensor, that possesses the required sensitivity is described in Chapter 4.

Chapter 4

Etched sensor

This chapter describes the development of the Etched sensor. The design is presented first followed by the modeling and then experimental work done to validate the model-predicted pressure sensitivity increases in this new sensor design. The complete manuscript containing the discussions in this chapter is included as Appendix C.

The overall objective of this work was to create a FBG-based pressure sensor with a major diameter smaller than that of the IVD sensor that is capable of measuring pressure variations of the order kPa.

4.1 Design concept

The features of the Etched sensor are shown in Figure 4.1a through 4.1c (also in Figure C1). As shown in Figure 4.1a the Etched sensor is similar in configuration to our previous IVD sensor in as much as both sensors utilize a length of stainless steel hypodermic tube that houses the FBG. The *probe* (Figure 4.1a) is gripped at its left hand end in a strain-relief connector that consists of a modified optical fibre patch-chord connector; within which a connection is made to an optical patch-cord. The optical patch-cord connects to the interrogation system for the sensor. The internal design features unique to the Etched sensor are shown in Figure 4.1b.

A single-mode optical fibre (Dow Corning SMF-28, Midland MI) is housed within, and positioned along the center-line of the stainless steel hypodermic tube. The fibre is positioned such that its terminal end is approximately aligned with the tip of the hypodermic tube. At the right-hand end of the hypodermic tube (Figure 4.1b), there is a

silicone seal (Dow Corning 3140 RTV, Midland MI) that covers the end of the hypodermic tube and occupies the annular volume between the inside diameter of the tube, Dt (Figure 4.1c), and the outside diameter of the optical fibre, Df (Figure 4.1c).

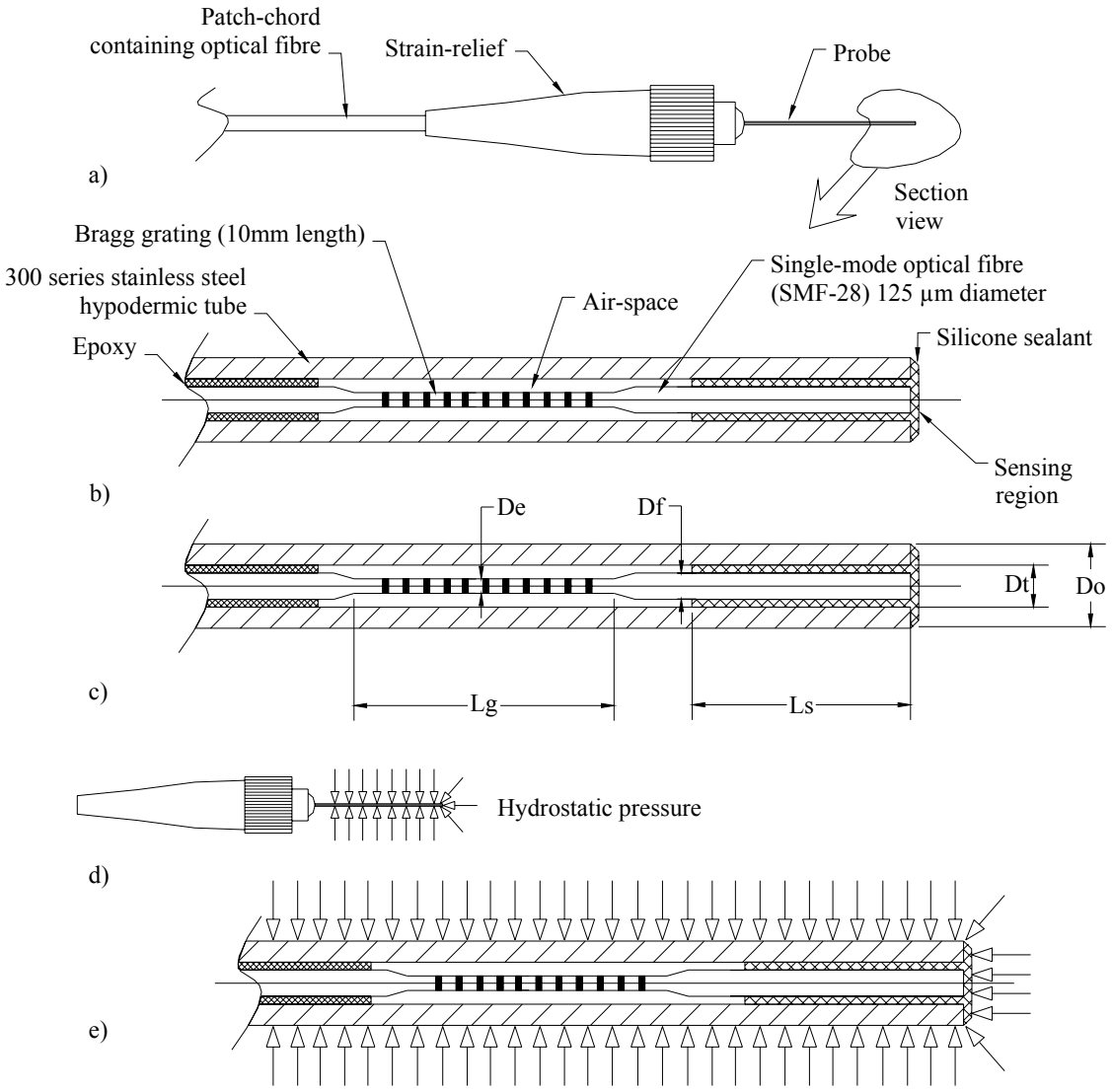

Figure 4.1: a) through c) design features of the Etched sensor; and d), e) Etched sensor with applied hydrostatic pressure.

The length of the silicone seal that extends (from right to left in Figure 4.1b) from the hypodermic tube tip toward the Bragg grating is designated as, Ls (Figure 4.1c). To the left of the length of fibre contained within the silicone, Ls, there is a segment of fibre that has reduced diameter, De (Figure 4.1c), that also contains the Bragg grating (10 mm

length, Micron Optics, Atlanta GA). The diameter of the fibre is reduced through a chemical etching process that is described in Appendix C. The nominal length of the fibre that is reduced in diameter and contains the Bragg grating is designated as, Lg (Figure 4.1c). To the left of the fibre segment of length Lg, the single-mode fibre extends toward the left, is 125 μm in diameter and is fixed in place with epoxy. The volume between the outside diameter of the fibre and the inside diameter of the hypodermic tube, over the length of the sensor between the silicone and epoxy, is occupied by air (Figure 4.1b), nominally at atmospheric pressure.

When the probe of the sensor is exposed to hydrostatic pressure (Figure 4.1d and 4.1e), this pressure acts on the cylindrical outer surface of the hypodermic tube and on the sensing region (Figure 4.1b). Relative to the silicone, the tube is rigid and, therefore, shields the optical fibre from the effects of the pressure on the outer cylindrical surface of the tube. The pressure applied to the sensing region (Figure 4.1b) causes strains in the silicone sealant and the optical fibre. Because there is a reduction in the cross sectional area where the fibre diameter transitions from Df to De, the strains along the region of fibre with length, Lg, and diameter, De, are amplified relative to the strains in the segment of fibre with diameter, Df. As described in the literature, strains in the FBG induce changes in its Bragg wavelength, λ_B, the characteristic wavelength of light that is reflected from a FBG. Consequently, shifts in λ_B are amplified (relative to the case where Df is equal to De) by etching the fibre cross section in the region of the grating. Therefore, the pressure sensitivity is also amplified by etching the fibre as described above.

4.2 Modeling and prototyping

As with the IVD sensor, a combination finite-element strain-optic model was used to predict the pressure induced shifts in the Bragg wavelength and the pressure sensitivity of the Etched sensor. For a given applied pressure on the sensor, the strains within the optical-fibre and along the Bragg grating were calculated using the finite-element model. These strains were then used as inputs to the strain-optic model to predict the corresponding shift in the Bragg wavelength. The pressure sensitivity of the Etched sensor was calculated by finding the Bragg wavelength shift for various applied pressures and using linear-regression to find the slope of the wavelength shift versus applied pressure data. The slope is termed pressure sensitivity, $\Delta\lambda_B / \Delta P$, and is expressed in units of picometers (pm) of wavelength shift versus change in applied pressure (MPa) or pm/MPa. The details of the finite-element and strain-optic model are completely detailed in Sections 2.3 and 2.4 of Appendix C.

The model was also used to study the effect, on sensor sensitivity, of varying the size of the design features shown in Figure 4.1c. Starting with a base-model (hereafter prototype 1), the design features were incrementally varied one at a time, and holding the size of all other features constant, over a range of values listed in Table C1. At each increment the effect, either an increase or decrease, on sensor sensitivity was assessed by calculating the strains along the Bragg grating. For example, if the strains in the Bragg grating of a given model were greater in magnitude than those of prototype 1, the sensor sensitivity was increased because the magnitude of Bragg wavelength shift is directly proportional to strain magnitude.

Three sensor prototypes were constructed and calibrated to test the model-predicted increases/decreases in sensitivity. The design feature sizes for each of the three prototypes are listed in Table 1. All prototypes were constructed with Ls and Lg of approximately 1.4 mm and 15 mm, respectively. Sensors with smaller values of Ls were constructed, however consistent sealing was difficult to achieve with Ls less than 1 mm, partly due to problems with sensor construction methods. Work is currently underway to improve the consistency of sensor construction using dedicated fixtures. Lg was held constant because the Bragg grating manufacturer could only supply gratings of 10 mm nominal length. Lg of 15 mm guaranteed that the gratings would be contained along the etched section of fibre, and also afforded a generous margin of error for chemical etching. The justifications for the rest of the design features are discussed in the next section.

4.3 Model and experimental results

Typical model-predicted strains for prototype 1 (Table C2) are shown in Figure C4a. From right to left along the sensor (Figure C4a), both axial and transverse strains have constant magnitude along Ls until the cross-sectional diameter of the fibre transitions from Df to De. Along the length of the fibre that is etched, the strains are amplified relative to those encountered along the fibre length Ls, as shown by the abrupt increase in strain magnitude at the start of Lg (Figure C4a). Progressing towards the length of fibre supported by the epoxy, the strain magnitudes diminish where the fibre diameter increases from De to Df. The general shape of the strain versus position profiles plotted in Figure C4a are typical of all prototypes, however magnitudes of strains vary between prototypes.

Table 1: Design feature sizes, model-predicted pressure sensitivity and experimentally measured pressure sensitivity for sensor prototypes.

Prototype	Design feature sizes	Predicted pressure sensitivity (pm/MPa) and $(r^2)^+$	Experimentally measured pressure sensitivity (pm/MPa) and $(r^2)^+$
(1) Do=400 μm	De=65 μm Df=125 μm Dt=200 μm Lg=15 mm Ls=1.4 mm	-62.4 1.00	-60.3 0.99
(2) Do=356 μm	De=37 μm Df=125 μm Dt=178 μm Lg=15 mm Ls=1.4 mm	-68.7 1.00	-64.2 0.99
(3) Do=200 μm	De=25 μm Df=25 μm Dt=165 μm Lg=15 mm Ls=1.4 mm	-59.9 1.00	-58.7 0.99

Notes: $^+$ correlation coefficients obtained from regression calculations

Figures C5a through C5e show the increases and decreases in strain along the grating resulting from varying the size of the design features shown in Figure 11c. The range of sizes of the design features correspond to ranges that could be constructed using available tubing and construction methods and are tabulated in Table C1. All increases and decreases in strain are plotted relative to strains in prototype 1. The key design compromises between sensor feature size and sensitivity are summarized below.

Sensors with reduced major diameter, Do, must have reduced inner diameter, Dt, as well. This is because hypodermic tube manufacturers cannot draw tubing of arbitrary wall thickness. As shown in Figure C5b, reductions in Dt result in reduced strain, 65 % relative to prototype 1, and therefore will reduce sensitivity. Reductions in Df also result in decreased strain (23 % in Figure C5c) because as Df decreases more load is born by the silicone and not the fibre. Shorter sensors will have increased sensitivity as shown by Figures C5d and C5e. When Lg or Ls is reduced, there is a corresponding increase in the strain of 42 % and 44 %, respectively. Reductions in the etched section diameter, De, have the greatest impact on sensitivity as shown in Figure C5a and C5c. For example, reducing De from 65 μm (as in prototype 1), to 25 μm results in a predicted strain increase of 947 %.

Both the model and experimental results established that the Etched geometry can result in sensors with diameter smaller than the IVD sensor and pressure sensitivity that is greater. The feature sizes of the three prototypes are shown in Table 1. Prototype 1 was modeled and constructed with Do equal to that of the IVD sensor (i.e. 400 μm) so that sensitivity increases, relative to the IVD sensor, resulting from the new sensor geometry and fibre etching could first be established. As shown in Table 1, the model predicted sensitivity was -62.4 pm/MPa or approximately three-times greater than that of the IVD sensor. The experimentally measured and predicted sensitivities matched to within 3.5 % where the experimental sensitivity is the reference for comparison. The calibration of the Etched sensors was performed using similar protocols and equipment to that utilized for the IVD sensor.

As shown in Table 1, prototypes 2 and 3 also had increased sensitivity compared to the IVD sensor and were constructed with major diameters of 356 μm and 200 μm, respectively. The predicted sensitivity of prototypes 2 and 3 were -68.7 pm/MPa and -59.9 pm/MPa, respectively. To offset the sensitivity reduction that results from decreasing diameter (Figure C5b) the etched fibre diameter was reduced in these prototypes as well (Table 1). The experimentally measured and predicted sensitivities matched to within 7.0 % and 2.0 % for prototypes 2 and 3, respectively.

Calibration results obtained using the fixed-filter demodulation technique, similar to that used with the IVD sensor, suggest that the increased pressure sensitivity of the Etched sensor could allow pressure measurements with sub-kPa repeatability. Example calibration data is plotted in Figure C7, and the regression calculated uncertainty in pressure measurement was found to be ± 0.36 kPa.

4.4 Summary

Significant improvements in sensitivity relative to the IVD sensor, and other FBG sensors in the literature, were achieved with development of the Etched sensor. To our knowledge, the Etched sensor is the only FBG-based sensor that is capable of measuring pressure with sub-kPa repeatability that also has a major diameter small enough for biomedical applications.

Chapter 5 describes the conclusions and future work resulting from the work presented in this thesis.

Chapter 5

Conclusions and Future Work

The objective of this work was to develop FBG-based pressure sensors that have increased sensitivity to hydrostatic pressure, relative to bare-FBGs, that also retain the desirable characteristics of FOSs, including small size and mechanical compliance.

A FBG-based intervertebral disc pressure sensor (IVD sensor shown in Figure A2a) was developed and validated. This sensor has a major diameter of 400 μm, an active sensing area of only 0.03 mm^2, and pressure sensitivity seven times greater than the sensitivity of a bare fibre FBG. When interrogated using fixed-filter demodulation, the IVD sensor was capable of resolving pressure variations smaller than 1 MPa. This sensor is also smaller and more mechanically compliant than any previously reported IVD pressure sensor.

The IVD sensor performance was validated by conducting disc pressure studies at the Department of Orthopaedic Engineering Research at the University of British Columbia. Disc pressure was measured in cadaveric pig FSUs using both the IVD sensor and the current standard strain-gauge sensor as a function of both compressive loads and lateral bending moments. Disc pressure measurements obtained using the IVD sensor agreed with those from the strain-gauge sensor and also those published in the literature.

The disc pressures measured during compressive loading, and the experimental observations, suggested that the IVD sensor impacted disc mechanics less (*i.e.* was less invasive) than the strain-gauge sensor. In general, the IVD sensor measured higher pressures than the strain-gauge sensor. The main cause of this was believed to be interference between the vertebrae of the FSU and the large strain-gauge sensor (2.45 mm

diameter). We hypothesized that loads were partially transmitted through the strain-gauge when the strain-gauge interfered with the vertebrae. This could result in less load transmission through the disc and a corresponding decrease in disc pressure. To our knowledge we were the first to obtain pressure measurements suggesting that sensor size impacts disc pressure. However, the link between sensor size and disc mechanics has long been hypothesized by previous investigators. Interference was not observed for the IVD sensor.

Results obtained from the lateral bending study suggested that disc geometry influenced the variation of disc pressure with applied moment. Pressure was found to increase with increasing moment in thicker discs that had height-to-thickness ratios greater than the average (*i.e.* 0.12). Conversely, in thinner discs it was found to decrease with increasing moment. Both increasing and decreasing pressure with increased moment has been presented in the literature. However to our knowledge we were the first to measure both in a single study and show differences in disc pressures based on disc geometry.

A second pressure sensor, the Etched sensor shown in Figure 4.1, was developed with sensitivity to pressure 20-times greater than a bare-FBG sensor and a major diameter and sensing area of only 200 μm and 0.02 mm^2, respectively. Increases in pressure sensitivity are achieved through mechanical amplification of axial strains experienced by the Bragg grating. Mechanical amplification is achieved by reducing the diameter of the fibre in the region of the Bragg grating, thereby resulting in reduced cross sectional area and therefore increased axial strains for a given applied pressure.

Sensor calibration was also performed using a fixed filter demodulation technique. Results obtained showed this new FBG sensor was capable of resolving pressure variations of the order kPa. To our knowledge, this is the only FBG sensor of this size (200 μm outside diameter) capable of resolving pressure variations of this magnitude.

The sensors presented in this thesis are significant improvements over other FBG pressure sensors with increased sensitivity relative to the case of a bare-FBG. Other FBG pressure sensors achieve increased sensitivity through polymer coating or large pressure diaphragms. The resulting sensors are usually much larger than a bare-fibre, with diameters from many millimeters to centimeters, and due to their size are not suitable for biomedical applications. Both the IVD and Etched sensor achieve increased pressure sensitivity relative to a bare-FBG while maintaining extremely small size. The Etched sensor is only 60 % larger in diameter than a bare-FBG, but has pressure sensitivity 20 times greater.

5.1 Future work

The FBG sensors described above are useful tools for biomedical research and could potentially be used in clinical settings. As with any medical device, before clinical application the potential benefits associated with the sensor must be established and shown to supersede the potential harm. As discussed above, the IVD sensor has already been validated *ex vivo*, and was shown to be less invasive than the current alternative. Therefore, future work aimed at establishing the clinical (*in vivo*) benefits could include establishing disc pressure measurement as a method of increasing the predictive accuracy of discography (described in Chapter 1). This would demonstrate the benefits of

measuring disc pressure *in vivo*, and could potentially allow clinicians to accurately diagnose which discs are sources of pain.

The Etched sensor is capable of resolving pressure variations over kPa. The level of resolution is sufficient for a range of biomedical pressure measurements including cerebrospinal fluid pressure and arterial blood pressure. Future work should attempt to validate the performance of the Etched sensor *ex vivo* in lab or cadaver models. Other work will include development of multiplexed FBG sensors, also with enhanced pressure sensitivity.

References

[1] Mignani, A. G., and Baldini, F., 1996, "Biomedical sensors using optical fibres," Rep. Prog. Phys., 59, pp. 1-28.
[2] Farrell, T., O'Connor, P., Levins, J., and McDonald, D., 2005, "Novel FBG interrogation technique for achieving < 100 n epsilon accuracies at remote distances > 70 km," Proceedings of SPIE, 5826(1), pp. 663-669.
[3] Udd, E., Lawrence, C., and Nelson, D., 1997, "Development of a Three Axis Strain and Temperature Fiber Optic Grating Sensor," Proceedings of SPIE, 3042, pp. 229-236.
[4] Udd, E., Nelson, D., and Lawrence, C., 1996, "Three Axis Strain and Temperature Fiber Optic Grating Sensor," Proceedings of SPIE, 2718, pp. 104-109.
[5] Geoffrey, A. C., 1998, "Temperature sensor based on a single Bragg grating," Proceedings of SPIE, 3483(1), pp. 296-300.
[6] Chuan, S. T., Jianzhong, H., and Rahul, M., 1998, "Fiber optic pressure sensor using a fiber Bragg grating," Proceedings of SPIE, 3429(1), pp. 123-130.
[7] Gander, M. J., MacPherson, W. N., Barton, J. S., Reuben, R. L., and Jones, J. D. C., 2002, "Embedded Micromachined Fibre Optic Fabry-Perot Pressure Sensors in Aerodynamic Applications," IEEE, 0-783-7454-1/02, pp. 1707-1712.
[8] Raskin, P. B., Alperin, N., Sivaramakrishnan, A., Surapaneni, S., and Lichtor, T., 2003, "Noninvasive intracranial compliance and pressure based on dynamic magnetic resonance imaging of blood flow and cerebospinal fluid flow: review of principles, implementation, and other noninvasive approaches," Neurosurgery Focus, 14(4), pp. 1-8.
[9] Warner, D. S., and Borel, C. O., 2004, "Treatment of Traumatic Brain Injury: One Size Does Not Fit All," Anesthesia Analgesia, 99, pp. 1208-1210.
[10] A. Nachemson, M. D., 1966, "The Load on Lumbar Disks in Different Positions of the Body," Clinical Orthopaedics and Related Research, 45, pp. 107-122.
[11] Alf Nachemson, M. D. J. M. M., 1964, "In Vivo Measurements of Intradiscal Pressure," Journal of Bone and Joint Surgery, American Volume 46-A, pp. 1077-1092.
[12] Seo, K.-S., Derby, R., Date, E. S., Lee, S.-H., Kim, B.-J., and Lee, C.-H., 2007, "In vitro measurement of pressure differences unsing manometry at various injection speeds during discography," The Spine Journal, 7, pp. 68-73.
[13] Nachemson, A., 1960, "Lumbar Intradiscal Pressure," Acta Orthopaedica Scandinavica supplementum, 43, pp. 1-104.
[14] P.A. Cripton, G. A. D., L.-P. Nolte, 2001, "A minimally disruptive technique for measuring intervertebral disc pressure in vitro: application to the cervical spine," Journal of Biomechanics, 34, pp. 545-549.
[15] McNally, D. S., and Adams, M. A., 1992, "Internal intervertebral disc mechanics as revealed by stress profilometry," Spine, 17, pp. 66-73.
[16] Dennison, C. R., Wild, P. M., Byrnes, P. W. G., Saari, A., Itshayek, E., Wilson, D. C., Zhu, Q. A., Dvorak, M. F. S., Cripton, P. A., and Wilson, D. R., 2008, "*Ex vivo* measurement of lumbar intervertebral disc pressure using fibre-Bragg gratings," Journal of Biomechanics, 41(1), pp. 221-225.
[17] Wilke, H.-J., Neef, P., Caimi, M., Hoogland, T., and Claes, L. E., 1999, "New in vivo measurements of pressures in the intervertbral disc in daily life," Spine, 24(8), pp. 755-762.

[18] Udd, E., 1991, Fibre Optic Sensors, An Introduction for Engineers and Scientists, Wiley InterScience.
[19] Hocker, G. B., 1979, "Fiber-optic sensing of pressure and temperature," Applied Optics, 18(9), pp. 1445-1448.
[20] Zhao, Y., and Ansari, F., 2001, "Intrinsic single-mode fiber-optic pressure sensor," IEEE Photonics Technology Letters, 13, pp. 1212-1214.
[21] Cibula, E., Donlagic, D., and Stropnik, C., 2002, "Miniature fiber optic pressure sensor for medical applications," IEEE, 0-7803-7454-1/02, pp. 711-714.
[22] Zhu, Y., and Wang, A., 2005, "Miniature fiber-optic pressure sensor," IEEE Photonics Technology Letters, 17, pp. 447-449.
[23] Watson, S., Gander, M. J., N.MacPherson, W., S.Barton, J., Jones, J. D. C., Klotzbuecher, T., Braune, T., Ott, J., and Schmitz, F., 2004, "Laser-machined fibres as ultra-miniature pressure sensors," Proceedings of SPIE, 5502, pp. 112-115.
[24] Tohyama, O., Kohashi, M., Sugihara, M., and Itoh, H., 1998, "A fibre-optic pressure microsensor for biomedical applications," Sensors and Actuators, A 66, pp. 150-154.
[25] Tohyama, O., Kohashi, M., Yamamoto, K., and Itoh, H., 1996, "A fiber-optic silicon pressure sensor for ultra-thin catheters," Sensors and Actuators A, 54, pp. 622-625.
[26] MacPherson, W. N., Gander, M. J., Barton, J. S., Jones, J. D. C., Owen, C. L., Watson, A. J., and Allen, R. M., 2000, "Blast-pressure measurement with a high-bandwidth fibre optic pressure sensor," Measurement Science and Technology, 11, pp. 95-102.
[27] Measures, R. M., 2001, Structural Health Monitoring with Fiber Optic Technology, Academic Press.
[28] Hill, K. O., Fujii, Y., Johnson, D. C., and Kawasaki, B. S., 1978, "Photosensitivity in optical fiber waveguides: Application to reflection filter fabrication," Applied Physics Letters, 32(10), pp. 647-649.
[29] Pieter, L. S., Beatrys, M. L., and Anatoli, A. C., 2005, "Chirped fiber Bragg grating sensor for pressure and position sensing," 44(5), p. 054402.
[30] Xu, M. G., Reekie, L., Chow, Y. T., and Dakin, J. P., 1993, "Optical in-fibre grating high pressure sensor," Electronics Letters, 29, pp. 398-399.
[31] Yeo, T. L., Sun, T., Grattan, K. T. V., Parry, D., Lade, R., and Powell, B. D., 2005, "Characterisation of a polymer-coated fibre Bragg grating sensor for relative humidity sensing," Sensors and Actuators B: Chemical, 110, pp. 148-155.
[32] Tse, F. S., and Morse, I. E., 1989, Measurement and Instrumentation in Engineering, Marcel Dekker Inc., New York.
[33] Taylor, J. R., 1997, An Introduction to Error Analysis, The study of uncertainties in physical measurements, University Science Books, Sausalito, CA.
[34] Liptak, B. G., 1994, Analytical Instrumentation, CRC Press.
[35] Sun, A., Qiao, X. G., Jia, Z. A., Li, M., and Zhao, D. Z., 2005, "Study of simultaneous measurement of temperature and pressure using double fiber Bragg gratings with polymer package," SPIE, p. 034402.
[36] Tjin, S. C., Hao, J. Z., and Malik, R., 1998, "Fiber Optic Pressure Sensor using Fiber Bragg Grating," Proceedings of SPIE, 3429, pp. 123-130.

[37] Nunes, L. C. S., Valente, L. C. G., Llerena, R. W. A., Braga, A. M. B., and Triques, A. L. C., 2004, "Simultaneous measurement of temperature and pressure using single fiber Bragg grating and fixed filter demodulation technique," Proceedings of SPIE, 5622, pp. 906-911.
[38] Wehrle, G., Nohama, P., Kalinowski, H. J., Torres, P. I., and Valente, L. C. G., 2001, "A fibre optic Bragg grating strain sensor for monitoring ventilatory movements," Measurement Science and Technology, 12, pp. 805-809.
[39] Maier, R. R. J., Barton, J. S., Jones, J. D. C., McCulloch, S., and Burnell, G., 2003, "Dual-fibre Bragg grating sensor for barometric pressure measurement," Measurement Science and Technology, 14, pp. 2015-2020.
[40] Hao-Jan, S., Ming-Yue, F., Tzu-Chiang, C., Chia-Min, L., Wen-Fung, L., and Sheau-Shong, B., 2004, "High-sensitivity pressure sensor based on a fiber Bragg grating," C. Brian, A. M. Michael, P. D. John, D. C. Samuel, and E. K. Helmut, eds., SPIE, pp. 248-254.
[41] Liu, L., Zhao, Q., Zhang, W., Zhang, H., Jin, L., Zhao, L., Yan, Y., and Gao, S., 2005, "Fiber Grating Pressure Sensor with Enhanced Sensitivity," Proceedings of SPIE, 5623, pp. 16-19.
[42] Ngoi, B. K. A., Paul, J., Zhao, L. P., and Fang, Z. P., 2004, "Enhanced lateral pressure tuning of fiber Bragg gratings by polymer packaging," Optics Communications, 242, pp. 425-430.
[43] Liu, Y., Guo, Z., Ztiang, Y., Cliiang, K. S., and Dong, X., 2000, "Simultaneous pressure and temperature measurement with polymer-coated fibre Bragg grating," Electronics Letters, 36(6), pp. 564-566.
[44] Zhang, Y., Feng, D., Liu, Z., Guo, Z., Dong, X., Chiang, K. S., and Chu, B. C. B., 2001, "High-sensitivity pressure sensor using a shielded polymer-coated fiber Bragg grating," IEEE Photonics Technology Letters, 13(6), pp. 618-619.
[45] Sheng, H.-J., Fu, M.-Y., Tzu-Chiang, C., Wen-Fung, L., and Sheau-Shong, B., 2004, "A lateral pressure sensor using a fiber bragg grating," IEEE Photonics Technology Letters, 16(4), pp. 1146-1148.
[46] Adams, M. A., McNally, D. S., and Dolan, P., 1996, "'Stress' Distributions Inside Intervertebral Discs," The Journal of Bone and Joint Surgery, 78-B(6), pp. 965-972.
[47] Schmidt, H., Kettler, A., Heuer, F., Simon, U., Claes, L., and Wilke, H.-J., 2007, "Intradiscal pressure, shear strain, and fiber strain in the intervertebral disc under combined loading," Spine, 32(7), pp. 748-755.
[48] Huang, S., LeBlanc, M., Ohn, M. M., and Measures, R. M., 1995, "Bragg intragrating structural sensing," Applied Optics, 34(22), pp. 5003-5009.
[49] Josef Pospiech, M. D. D. S., M.D.; Hans J. Wilke, Ph.D; Lutz E. Claes, Ph.D, 1999, "Intradiscal Pressure Recordings in the Cervical Spine," Neurosurgery, 44, pp. 379-384.
[50] Hans-Joachim Wilke, S. W., Lutz E. Claes, Markus Arand, Alexander Wiesend, 1996, "Influence of Varying Muscle Forces on Lumbar Intradiscal Pressure: An In Vitro Study," Journal of Biomechanics, 29, pp. 549-555.
[51] Saari, A., Dennison, C. R., Wild, P. M., Wilson, D. R., Dvorak, M. F. S., Itshayek, E., and Cripton, P. A., 2008, " Intervertebral disc pressure measurements: Influence of disc thickness on disc pressure during lateral bending," World Forum for Spine ResearchKyoto Japan.

Appendix A: A minimally invasive in-fibre Bragg grating sensor for intervertebral disc pressure measurements

(IN PRESS)

Will appear in Measurement Science and Technology, Volume 19, Issue 8, August 2008

A minimally invasive in-fibre Bragg grating sensor for intervertebral disc pressure measurements

Christopher R. Dennison[1], Peter M. Wild[1], David R. Wilson[2], and Peter A. Cripton[2,3]

[1]*Department of Mechanical Engineering, University of Victoria, British Columbia, Canada*
[2]*Division of Orthopaedic Engineering Research, Departments of Orthopaedics, and*
[3]*Mechanical Engineering, University of British Columbia, Canada*

Corresponding Author:
Chris R. Dennison
University of Victoria
Department of Mechanical Engineering
P.O. Box 3055
Victoria, B.C.
V8W 3P6
Ph: (250) 853-3198
Fax: (250) 721-6051
e-mail: dennison@uvic.ca

Abstract

We present an in-fibre Bragg grating (FBG) based intervertebral disc pressure (IVD) sensor that has pressure sensitivity seven times greater than that of a bare fibre, and a major diameter and sensing area of only 400 μm and 0.03 mm^2, respectively. This is the only optical, the smallest, and the most mechanically compliant disc pressure sensor reported in the literature. This is also an improvement over other FBG pressure sensors that achieve increased sensitivity through mechanical amplification schemes, usually resulting in major diameters and sensing lengths of many millimeters. Sensor sensitivity is predicted using numerical models, and the predicted sensitivity is verified through experimental calibrations. The sensor is validated by conducting IVD pressure measurements in porcine discs and comparing the FBG measurements to those obtained using the current standard sensor for IVD pressure.

The predicted sensitivity of the FBG sensor matched with that measured experimentally. IVD pressure measurements showed excellent repeatability and agreement with those obtained from the standard sensor. Unlike the current larger sensors, the FBG sensor could be used in discs with small disc height (*i.e.* cervical or degenerated discs). Therefore there is potential conduct new measurements that could lead to new understanding of the biomechanics.

1. Introduction

In-fibre Bragg gratings (FBGs) are used extensively as sensors for various parameters including displacement [1], strain [2], temperature [3], pressure [3], humidity [4], and radiation dose [5] among others. FBGs are an attractive alternative to other piezoelectric, resistive or other solid-state sensing technologies because they are: small (typically 125 μm in diameter), mechanically compliant, intrinsically robust, chemically inert, resistant to corrosive environments, immune to electromagnetic interference, and are capable of simultaneous multi-parameter sensing when suitably configured [6]. Moreover, multiple FBG sensors can be multiplexed along a single optical fibre thereby allowing spatially distributed measurements [7].

Despite these characteristics, FBG sensors are applied only on a limited basis in medical pressure measurement applications, primarily because bare FBGs possess low sensitivity to hydrostatic pressure. Mechanical amplification schemes, such as polymer coatings on the fibre circumference [8-10] or pressure diaphragms [11], can be used to increase the pressure sensitivity by increasing the area over which the pressure acts. For example, Xu *et al.* (1996) presented a glass-bubble housed FBG sensor [3] and Liu *et al.* (2000) [12], Sheng *et al.* (2004) [13] and Zhang *et al.* (2001) [14] present polymer coated

FBG sensors all with major diameters of the millimeter order. Because of their increased size, these sensors do not retain the intrinsic benefits offered by FBGs, namely small size, spatial resolution and mechanical compliance. Moreover, and in the context of medical pressure measurement applications, these large sensors would be more invasive than current alternatives [15].

Recently, we were the first to apply bare FBGs (125 μm diameter and 10 mm length, Bragg wavelength 1550 nm) to measurement of intervertebral disc pressure [16] which ranges over 3 MPa in cadaveric human discs [17]. Although the FBG pressure measurements were consistent with those found in previous disc pressure studies [16], they were not always consistent with measurements made using the current standard Strain gauge-based sensor for disc pressure measurement [18-22]. Moreover, the FBGs sensing length (*i.e.* 10 mm) was too large to allow mapping of pressure distributions within the intervertebral disc. Finally, poor pressure sensitivity resulted in highly discretized data over the 3 MPa pressure ranges studied.

The objective of this work was to design and validate the performance of a new FBG pressure sensor (hereafter FBG sensor) that has both improved pressure sensitivity and spatial resolution compared to the bare fibre and a major diameter of only 400 μm. The pressure sensitivity of the sensor is calculated using a combination of finite-element modeling and strain-optic relationships. The calculated sensitivity is experimentally validated and the sensor is applied to intervertebral disc pressure measurements in a porcine cadaveric disc subjected to compressive loading. The results obtained using the FBG sensor are also compared to those made with the current standard strain gauge-based sensor for disc pressure measurement.

2. Pressure measurements in intervertebral discs

The mechanical structure of the spine consists of bone vertebrae separated by intervertebral discs (IVDs). Figure 1a shows a motion segment of the spine including both a superior (upper) and inferior (lower) vertebra separated by the IVD as well as the bone processes on the posterior of the spine that articulate at the facet joints (Figure 1a). When the spine and, therefore, the motion segment are loaded in compression (Figure 1b) the vertical distance between the vertebrae is reduced, thereby reducing the IVD height from its nominal unloaded height (Figure 1b). When the IVD height is reduced, there is a corresponding increase in the hydrostatic pressure in the semi-fluid region in the center of the IVD, termed the nucleus pulposus (Figure 1c). The nucleus pressure is exerted on both the superior and inferior vertebra and on the lateral annulus, thereby resulting in equilibrium of loads.

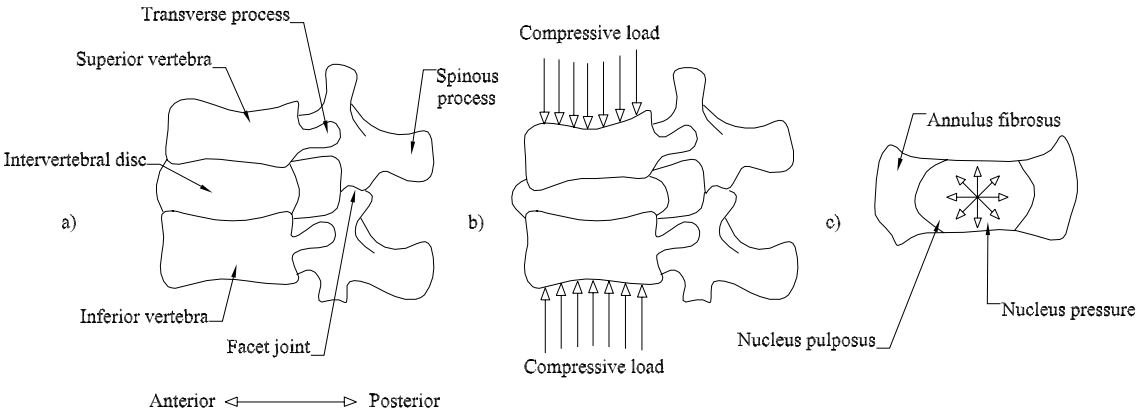

Figure 1: a) schematic of spinal motion segment consisting of superior and inferior vertebra, intervertebral disc (IVD), and bony processes on posterior of spine as well as the facet joint. b) schematic showing exaggerated deformations of motion segment as a result of compressive load. and c) cross section of IVD showing fibrous annulus and semi-fluid nucleus pulposus as well as hydrostatic pressure within nucleus resulting from compressive load.

Degeneration of the IVD can take many forms, including tears in the annulus and/or dehydration of the nucleus. It is a widespread problem in industrialized societies and is often associated with disabling back pain and decreased quality of life. Back pain is among the most frequent causes of workplace absenteeism in North America [21, 22].

The development of disc degeneration is a multi-factorial process in which disc mechanics is thought to play an important role [23, 24]. Therefore, understanding human IVD mechanics is central to understanding the etiology and symptoms of disc degeneration [17]. Pressure distributions in IVDs are an important indicator of disc mechanics that have been measured both *in vivo* (*i.e.* in living subjects, and clinically) [25, 26] and *ex vivo* (*i.e.* in cadaver specimens for research purposes) [17, 27-30]. It is known that, in the lumbar spine, nucleus pressure increases linearly with applied compressive load and is hydrostatic in healthy discs [17], while in degenerated discs this hydrostatic behaviour is disrupted [31].

Investigators have sought to understand disc mechanics and degeneration through pressure measurements using rigid needle-mounted strain gauge (SG) sensors [32]. These SG sensors are the current standard tool and have been used both *ex vivo* and *in vivo.* They are inserted into the IVD by first passing the needle through the annulus and subsequently positioning the tip of the needle in the nucleus [18-22]. These SG sensors are housed in large needles (1.3 mm to 3 mm diameter) that can injure the fibres of the annulus and alter the mechanics of the IVD [32]. In experimental models with disc heights comparable to the sensor diameter (e.g. porcine or human cervical discs), these sensors can interfere with the vertebrae as well as other anatomic features such as the bone processes shown in Figure 1a [32, 33]. These drawbacks limit the utility of the

sensors for *ex vivo* research and, in clinical applications, may have long term effects on disc health and degeneration that are not completely understood [22, 32]. These long term effects have limited the use of pressure measurements to mainly *ex vivo* experiments and thick discs [32].

3. Materials and methods

3.1 FBG sensor

We designed and constructed a FBG pressure sensor that retains the intrinsic benefits of Bragg gratings, namely small size and mechanical compliance (Figure 2a). The sensor is similar to the SG sensors in as much as it is needle-mounted but by virtue of its flexibility and size it is much less invasive. The design of the sensor is provisionally patented [34].

The FBG sensor is comprised of a single-mode optical fibre (Dow Corning SMF-28, Midland MI) housed within a length of stainless steel hypodermic tube (0.4 mm outside diameter and 0.1 mm wall thickness). The fibre is positioned such that it is coaxial with the hypodermic tube and such that its tip is flush with the (inserted) right hand end of the hypodermic tube, as shown in Figure 2a. A Bragg grating (Blue Road Research, Gresham OR, 10 mm length) is etched into the core of the fibre and is positioned at the right hand end of the fibre. The annular volume between the inside diameter of the hypodermic tube and the outside diameter of the optical fibre is filled with a compliant silicone sealant (Dow Corning 3140 RTV, Midland MI). The silicone is bonded to the inner surface of the hypodermic tube and to the outer surface of the fibre. The *sensing region* of the sensor consists of the exposed surfaces of silicone sealant and optical fibre at the right hand end of the tube and has an area of only 0.03 mm^2. At the

left hand end, the hypodermic tube is gripped in a modified optical fibre patch-chord connector within which a connection is made to an optical patch cord. The length of tube that extends from the fitting is called the *probe.* In the current sensor, the probe is 50 mm in length but the sensor can be constructed with any probe length. The optical patch cord connects to the interrogation system for the sensor.

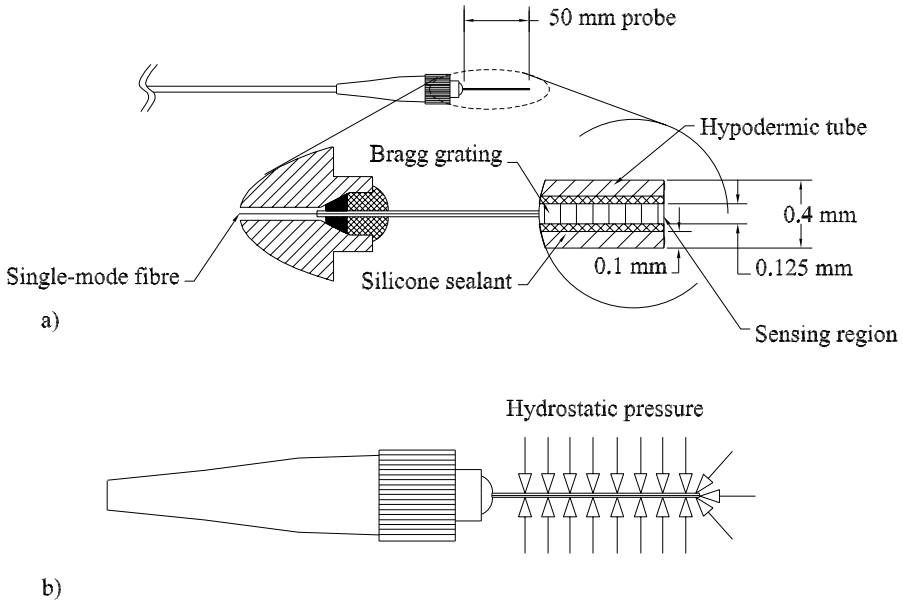

Figure 2: a) Schematic showing construction of the in-fibre Bragg grating pressure sensor. b) Applied hydrostatic pressure over the hypodermic tube and sensing region.

When the probe of the FBG sensor is exposed to hydrostatic pressure, the pressure acts on the cylindrical outer surface of the hypodermic tube and on the sensing region (Figure 2a and b). Relative to the silicone, the tube is rigid and, therefore, shields the optical fibre from the effects of the pressure on the outer cylindrical surface of the tube. The pressure applied to the sensing region causes strains in the silicone sealant and the FBG. The strains in the FBG induce changes in its Bragg wavelength, λ_B, the characteristic wavelength of light that is reflected from a FBG [6].

3.2 Finite-element model

The pressure-induced strains within the FBG sensor were calculated as a function of applied hydrostatic pressure, over the range of physiologic nucleus pressures from 0 MPa to 3 MPa, using a commercially available suite of finite-element structural analysis codes (ANSYS® version 10, Canonsburg PA). Figure 3 is a schematic showing the model geometry as well as the displacement and pressure boundary conditions.

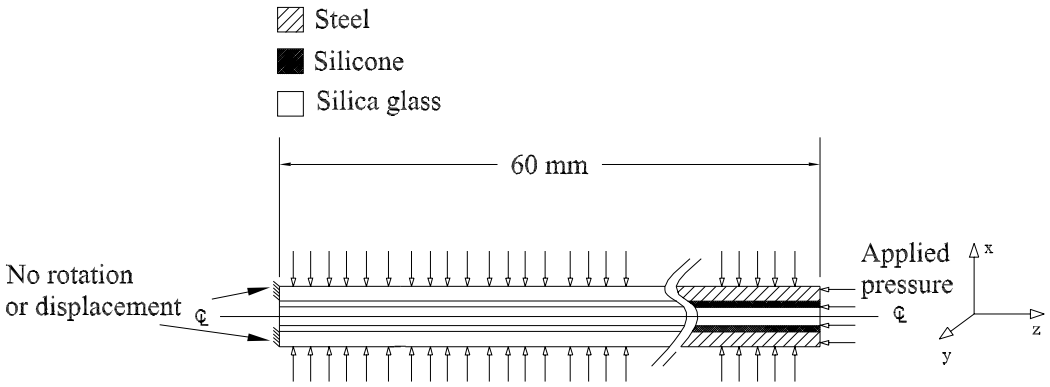

Figure 3: Schematic showing dimensions and displacement/pressure boundary conditions used in the finite-element model. Pressure is applied to entire sensor length.

The hypodermic tubing was specified as 300 series stainless steel with Young's modulus and Poisson ratio of 190 GPa and 0.28, respectively [35]. The Young's modulus and Poisson ration of the silica glass optical fibre were 70 GPa and 0.17, respectively [7]. The Young's modulus and Poisson ratio of the silicone were 372 kPa and 0.49, respectively, based on information supplied by Dow Corning technical staff.

The model was first solved using PLANE182 (tetrahedron) [27] elements for 3 MPa applied pressure to ensure model deflections were maximum. Mesh refinements were subsequently performed until the relative difference in the predicted strain (along the Bragg grating) between the models was less than 1%. Once the mesh convergence was established, the element type was changed to PLANE42 (triangle) [27] elements to

verify element-type independence of the solution by ensuring the relative difference in the average predicted strain along the Bragg grating was less than 1%.

3.3 Strain-optic model

As will be discussed in Section 4.0 and as shown in Figure 4a, pressure applied to the sensing region causes strain gradients along the z-axis (Figure 3) of the Bragg grating. Gradients in the both the axial strain, ε_z, and transverse strain, ε_x and ε_y, have been shown to result in variations in the Bragg wavelength, λ_B, as well as increases in the full-width at half maximum (FWHM) and decreases in the maximum reflectivity of a Bragg grating [36] as shown in Figure 4b. These variations cannot be predicted using Bragg's condition, which is commonly applied to predict Bragg wavelength variations when the strains along a grating are uniform [6].

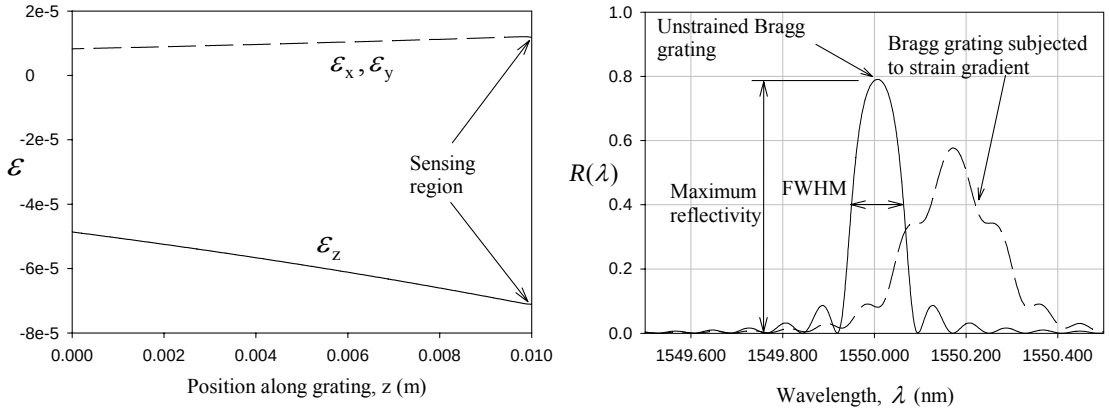

a) b)

Figure 4: a) Example data for axial, ε_z, and transverse, $\varepsilon_x, \varepsilon_y$, strain versus axial position, z, along grating. Strains shown for 3 MPa applied pressure. b) Strain gradients along the FBG result in: shifts in the Bragg wavelength, λ_B; an increase in the Bragg grating's full-width at half maximum reflectivity (FWHM) and a decrease in the maximum reflectivity as compared to an unstrained grating.

Previous investigators have developed models that predict the Bragg wavelength shifts, increases in the FWHM, and decreases in the maximum reflectivity for FBGs subjected to non-uniform strain or, equivalently, for an FBG having non-uniform grating periods and indices of refraction [36-39]. In this research, we employed the transfer-matrix (τ-matrix) formalism presented by Huang *et al.* (1995) [36]. The physical background and mathematical formulation of the τ-matrix method is detailed elsewhere [36]. The details of its implementation are summarized here.

The reflected Bragg wavelength, λ_B, of a grating subjected to uniform strain can be predicted by treating the grating as a discrete volume and using a single equation. For a grating subjected to non-uniform strain, the τ-matrix formulation requires discretization of the original grating into sub-gratings of length, L_i, and average grating pitch, Λ_i (Figure 5b). The intensity of the light entering and leaving the left-side of the grating ($A(0)$ and $B(0)$ respectively) are then related to the light entering and leaving the right side ($A(L)$ and $B(L)$) (Figure 5b) by equation (1):

$$\begin{bmatrix} A(0) \\ B(0) \end{bmatrix} = [\tau_1][\tau_2].....[\tau_n] \begin{bmatrix} A(L) \\ B(L) \end{bmatrix} \quad (1)$$

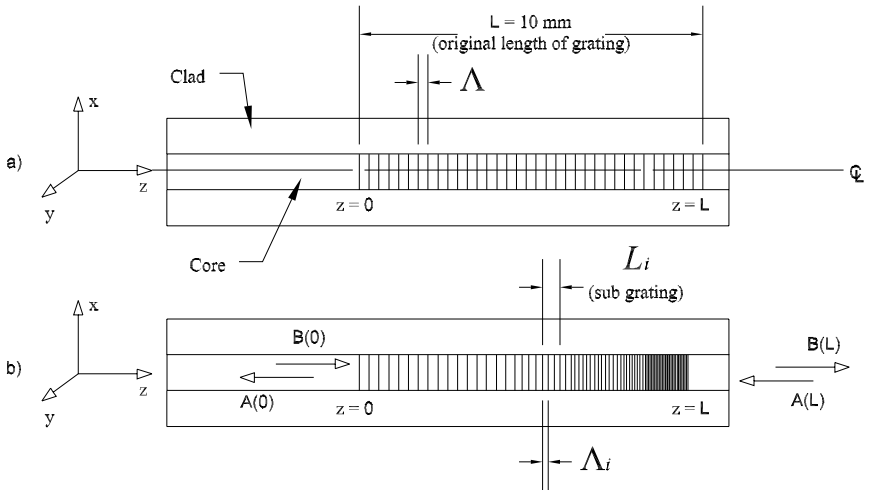

Figure 5: a) Schematic showing Bragg grating pitch Λ and length L of unstrained grating, and b) schematic showing grating with a strain gradient along axis z. L_i and Λ_i are the average length and pitch of each sub-grating element used in the τ -matrix formulation.

where $[\tau_i]$ represent the transfer matrices (τ -matrices) for each sub-grating of length, L_i. The reader is referred to Huang *et al.* (1995) [36] for the functional form of the τ -matrices.

For each sub-grating, calculation of the τ -matrix requires: the average index of refraction, $\bar{n}_i$; the average grating pitch, Λ_i; and the length, L_i. In this model we assume that the periodic modulation in the index of refraction was a sinusoidal function of position z along the grating [36]:

$$n(z) = n_o + \Delta n_o \cos\left(\frac{2\pi z}{\Lambda}\right) \qquad (2)$$

Where, $n(z)$ is the index of refraction at a given location, z; n_o is the nominal index of refraction of the fibre (assumed here to be 1.44) [36]; Δn_o is the amplitude of the index

change (assumed here to be 7 x 10^{-5}) [36] and; Λ is the pitch of the original unstrained grating (assumed to be 517 nm) [36] (Figure 5a).

As mentioned previously, strains within the grating produce a predictable change in the index of refraction. Therefore, the average index of refraction within a given sub-grating is given by equation (3):

$$\bar{n}_i = n_o + \Delta n_o \cos\left(\frac{2\pi z}{\Lambda}\right) - \frac{1}{2} n_o^3 (p_{11}\varepsilon_z + p_{12}\varepsilon_x + p_{12}\varepsilon_y) \tag{3}$$

where p_{11}, p_{12} are elements of the photo-elastic tensor (0.252 and 0.113 respectively [36]) that relate elastic strain to changes in index of refraction [7], $\varepsilon_z, \varepsilon_x, \varepsilon_y$ are the average strains within the grating at the location of the sub-grating and correspond to the coordinate axes shown in Figure 5. The average grating pitch, Λ_i, is also calculated using the strains as:

$$\Lambda_i = \Lambda(1+\varepsilon_z) \tag{4}$$

where Λ is the pitch of the unstrained grating (Figure 5a). The reflected light-intensity versus wavelength spectrum from the grating is found by solving Equation 2 for A(0) assuming B(0) has a constant intensity of unity for all wavelengths (*i.e.* B(0) = 1 and B(L) = 1-A(0)) [36]:

$$R(\lambda) = \left|\frac{A(0)}{B(0)}\right|^2 \tag{5}$$

where $R(\lambda)$ is the wavelength, λ, dependent light intensity reflected by the grating and is the norm of A(0)/B(0).

The strains, $\varepsilon_z, \varepsilon_x, \varepsilon_y$, along the core of the fibre were obtained from the results of the finite-element model and were used in the relations described above to determine the reflected spectrum from the FBG, as a function of applied hydrostatic pressure.

3.4 FBG sensor calibration

Experimental data in the form of Bragg wavelength versus applied hydrostatic pressure, ranging from 0 MPa to 3 MPa, was obtained using a purpose-built calibration apparatus. This experimental data was collected to allow validation of the FBG sensor finite-element/strain-optic model predicted sensor sensitivity.

The calibration apparatus was configured similarly to that described by Xu *et al.* (1993) [3] and included a broad C-band light source (AFC-BBS1550, Milpitas CA), a bi-directional 3 dB optical coupler (Blue Road Research, Gresham OR), an optical spectrum analyzer (OSA) (ANDO AQ6331, Tokyo JP), a purpose built pressure vessel and a reference pressure transducer (OMEGADyne PX01C1, Stamford CT, Acc.: 0.05% FS – 6.9 MPa).

The FBG sensor was inserted into the pressure vessel and sealed *via* a bulkhead fitting. Pressure was manually varied from 0 MPa to 3 MPa to 0 MPa (as reported by the reference transducer) using a manual hydraulic pump (ENERPAC P141, Milwaukee WI) while Bragg wavelength variations were recorded from the OSA. This procedure was repeated five times.

We also commissioned optical interrogation equipment designed to convert changes in Bragg wavelength to analogue voltages similar to that described in Nunes *et al.* (2004) [40]. The *fixed filter demodulation technique* allows direct calibration of the FBG sensor in terms of analogue voltage versus pressure. This demodulation technique,

and the calibration apparatus, was used to calibrate the FBG sensor from 0 MPa to 3 MPa. Analogue voltage versus applied pressure was acquired at 60 Hz and the average sensitivity of the sensor, and standard error in pressure measurement, was calculated from 10 calibration datasets acquired using hardware and software implemented in LabView© (Version 8, Austin TX).

3.5 Intervertebral disc pressure measurements

The experimental work concluded with the application of the FBG sensor to measurements of IVD pressure within a single cadaveric porcine (pig) disc. First, the repeatability of the FBG sensor was established by performing multiple pressure measurements under repeated loading with the FBG sensor location fixed. This process was performed at three non-collinear locations in the IVD. Subsequently, we repeated pressure measurements within the IVD at the three locations using both the FBG and SG sensors.

The functional spine unit (FSU) (Figure 6) was harvested fresh after death and consisted of a superior and inferior vertebra separated by an IVD. Vertebral ligaments were left intact, and the vertebrae adjacent to the disc were set into dental stone in a manner similar to that described by Adams *et al.* (1996) [31].

The dental stone containing the inferior vertebra of the FSU was then secured to a materials testing machine (Instron 8874, Norwood MA) (Figure 6). To allow insertion of the FBG sensor, the annulus was first pierced using a 25ga. (0.5 mm outside diameter) hypodermic needle. The needle was used because it had a cutting tip, unlike the FBG sensor. However, future FBG sensor prototypes will include a cutting tip thereby allowing insertion without the aid of a needle.

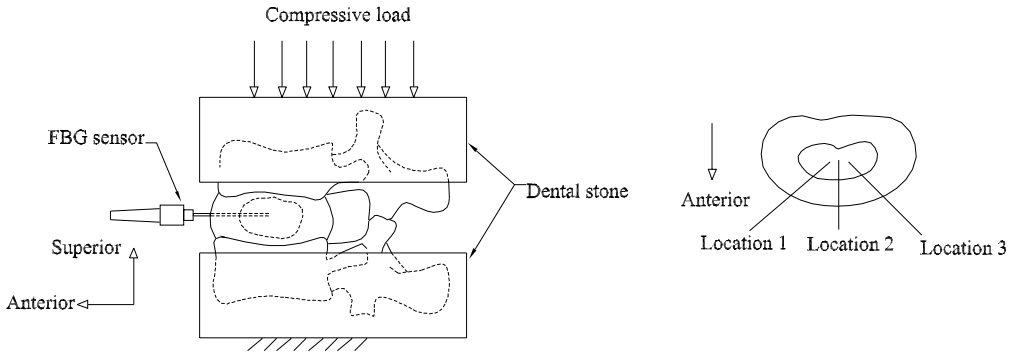

Figure 6: Schematic showing functional spine unit (FSU) embedded in dental stone. Annulus left exposed for sensor insertion. Inferior dental stone fixed to materials testing machine while superior dental stone has compressive load applied to it. Insertion locations also shown to right; sensors inserted along the axes shown.

The tip of the FBG sensor was inserted through the pierced annulus, then into the nucleus such that its sensing region (Figure 2) was at the approximate centre of the nucleus (Figure 6). The centre of the nucleus was estimated using measurements of the IVD, and was assumed to be half of the disc diameter as measured along the sensor insertion axis (Figure 6).

Compressive loads were then applied to the dental stone containing the superior vertebra (Figure 6) ranging from 0 N to 500 N, at 40 N/s. Load data was obtained from a calibrated load-cell (Sensor Data M211-113, Sterling Heights MI, Acc.: 0.05% FS – 10 kN) that was integrated into the materials testing machine. Pressure data was acquired from the FBG sensor using the fixed-filter demodulation technique already described.

We repeated the procedures above using a needle-mounted strain gage sensor (SG sensor, Figure 7) (Model 060S; pressure range, 0–3.5 MPa; 2.45mm diameter; Precision Measurement Co., Denton, Ann Arbor, USA). This type of sensor has been widely used by other investigators studying IVD pressure [18-22]. Each sensor was used to measure pressure 3 times at each insertion location.

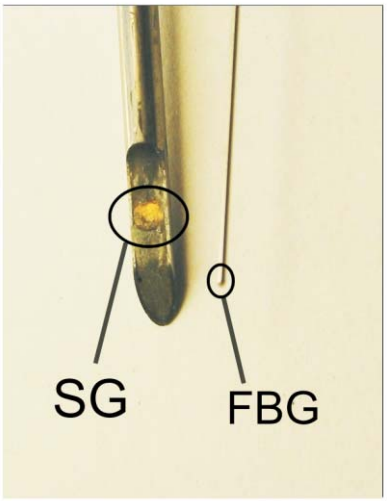

Figure 7: Image showing relative diameters of SG sensor and FBG sensor. Sensing region of SG sensor consists of circular strain-gage element near tip of needle.

4. Results

4.1 Finite-element model

The linear model satisfied all convergence criteria (outlined in the Methods) with an axisymmetric mesh of 240,000 PLANE182 elements of the following nominal distance between element nodes: Steel: 15 x 10^{-6} m; silicone: 5 x 10^{-6} m; and fibre: 15 x 10^{-6} m. This mesh also satisfied all ANSYS® aspect ratio criteria [28] both before the model was solved and after the model was solved and the mesh had deflected.

The relative difference in the predicted strains of the linear model using PLANE182 (tetrahedron) [27] elements and PLANE42 (triangle) [27] elements was 0.089 % (ε_z) and 0.20 % ($\varepsilon_x, \varepsilon_y$) and satisfied the element independence criteria outlined in the Methods.

Figure 8 qualitatively shows the deflections of the silicone and fibre as revealed by the finite element model. As applied pressure is increased from 0 MPa to 3 MPa, the silicone and fibre deflect mainly in the z-direction (to the left of the undeformed edge in

Figure 8), with the highest magnitude deflections occurring at the probe tip (Bottom Figure 8). The deflections in the z-direction decrease in magnitude along the sensor (from right to left in Figure 8), and are at their minimum at the left hand side of the sensor. The silicone has the highest magnitude of deflections because its Young's modulus is several orders of magnitude smaller than both the optical fibre and steel.

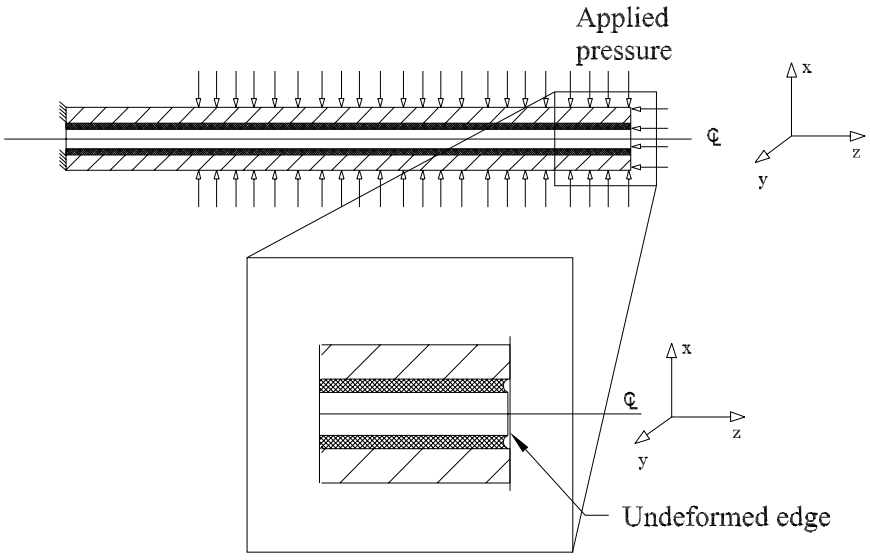

Figure 8: Top: Probe of FBG sensor subjected to applied pressure; and Bottom: section view showing scaled deformations around the FBG sensor tip.

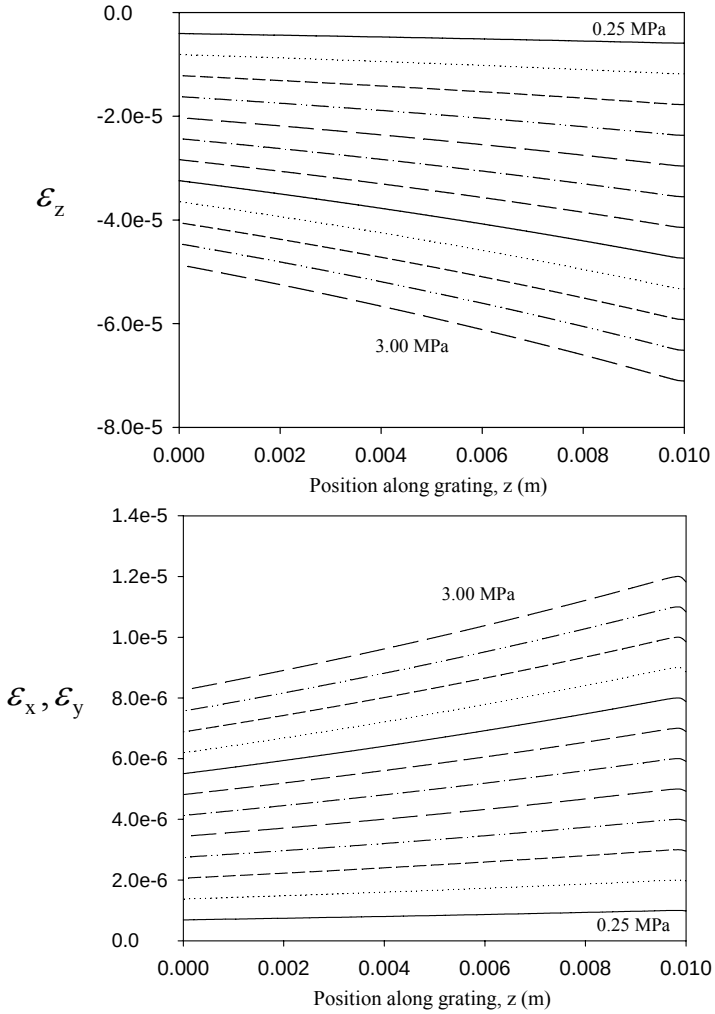

Figure 9: Predicted axial (ε_z) and transverse ($\varepsilon_x, \varepsilon_y$) strain along the z-axis of the Bragg grating for various applied hydrostatic pressures ranging from 0.25 MPa to 3.00 MPa at 0.25 MPa increments. Results for 0 MPa not plotted as this is the unstrained configuration. Refer to Figure 5 for z positions along grating.

Figure 9 shows the predicted axial and transverse strains along the length of the Bragg grating (axis z, x=y=0 in Figure 6). Axial strains are compressive, maximum at the sensor tip or sensing region (z = 0.01 m) and have a monotonically decreasing magnitude toward the opposite end of the grating (z = 0.00 m) (Figure 9). Conversely, transverse

strains are tensile, maximum at the sensor tip and decrease monotonically toward the opposite end of the grating. Shear strains were two orders of magnitude smaller than both the axial and transverse strains presented; therefore their contribution to the strain-optic response of the sensor is negligible and we have not presented these in detail.

Figure 9 shows only the strains at the center-line of the fibre core, along the Bragg grating (axis z, x=y=0 in Figure 6). However, the grating occupies the entire core which has a outside diameter of 8.2 μm [41]. To establish that the strains within the core were approximately constant we calculated the maximum difference between the predicted strains along the center-line of the grating and the strains along the outside diameter of the core and found a maximum difference of 8.0 nε (0.04 %) for the axial strain, ε_z, and 3.3 nε (0.12 %) for the transverse strains, $\varepsilon_x, \varepsilon_y$, respectively.

4.2 Comparison: calculated and experimentally measured FBG sensor sensitivity

The Bragg wavelength reflected by the FBG sensor, as calculated using the predicted strains and the τ-matrix model, is shown for various applied pressures in Figure 10. As pressure increases from 0 MPa to 3 MPa the Bragg wavelength is blue-shifted (shorter wavelengths) and the FWHM increases by only 0.0010 nm from 0.11 nm.

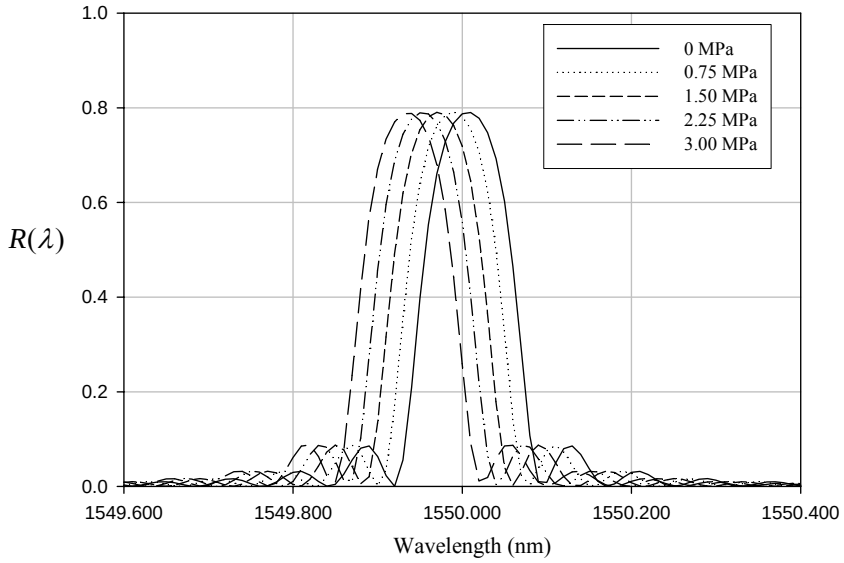

Figure 10: Calculated reflection spectra of the FBG sensor obtained from the strain-optic model with predicted strains from finite-element model. With increasing pressure spectra are blue-shifted with negligible increase in the FWHM.

Figure 11 shows the experimental and calculated variations in Bragg wavelength versus applied hydrostatic pressure for our FBG sensor. Experimental data points for each pressure are averaged from the five trials and the magnitude of the error bars (± 5 pm) corresponds to the published absolute-wavelength measurement reproducibility for the OSA [42]. The standard deviation of wavelength measurements obtained from linear regression calculations is ± 0.3 pm. The sensitivity of the FBG sensor is calculated as the slope of these data sets, or the change in Bragg wavelength over the change in applied pressure ($\Delta\lambda / \Delta P$) . From linear-regression calculations the finite element/strain optic calculated sensitivity is -23.9 pm/MPa (r^2=1) whereas the experimental sensitivity is -21.5 ± 0.07 pm/MPa (mean ± standard error from five trials) (r^2=0.99). The relative difference between these sensitivities is 11.1 % where the experimental sensitivity is the reference for comparison.

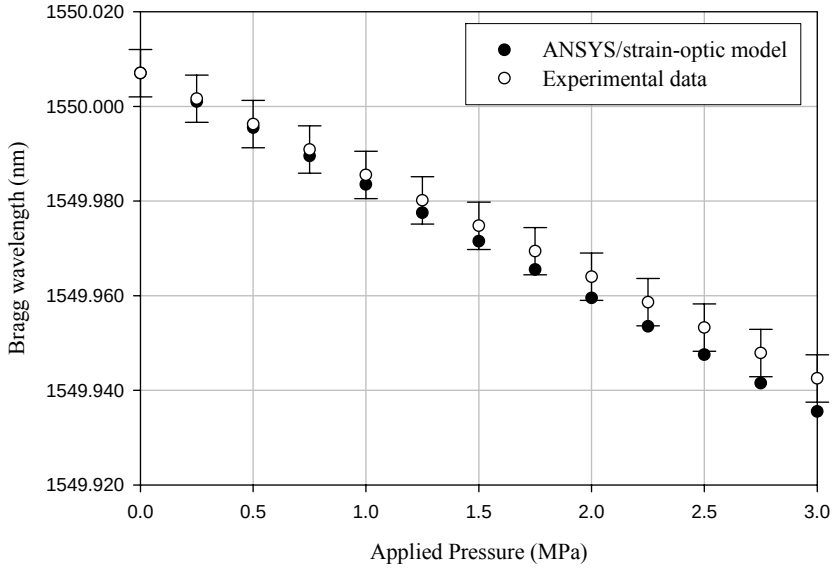

Figure 11: Experimentally measured and calculated variations in Bragg wavelength versus applied hydrostatic pressure (for our FBG sensor). Slope of each data-set is expressed as the sensitivity to hydrostatic pressure. Vertical error bars for experimental data (± 5 pm) correspond to the published measurement reproducibility of the OSA. Horizontal error bars (± 3.5 kPa) not visible at this scale.

4.3 Intervertebral disc pressure measurements

Figure 12 shows typical results obtained from both the FBG and SG sensors for measured pressure versus applied compressive load in the porcine IVD. The disc response to load (kPa/N) is the regression-calculated slope of the pressure versus load data. Maximum measured pressure is the measured pressure (MPa) at 500 N of compressive load.

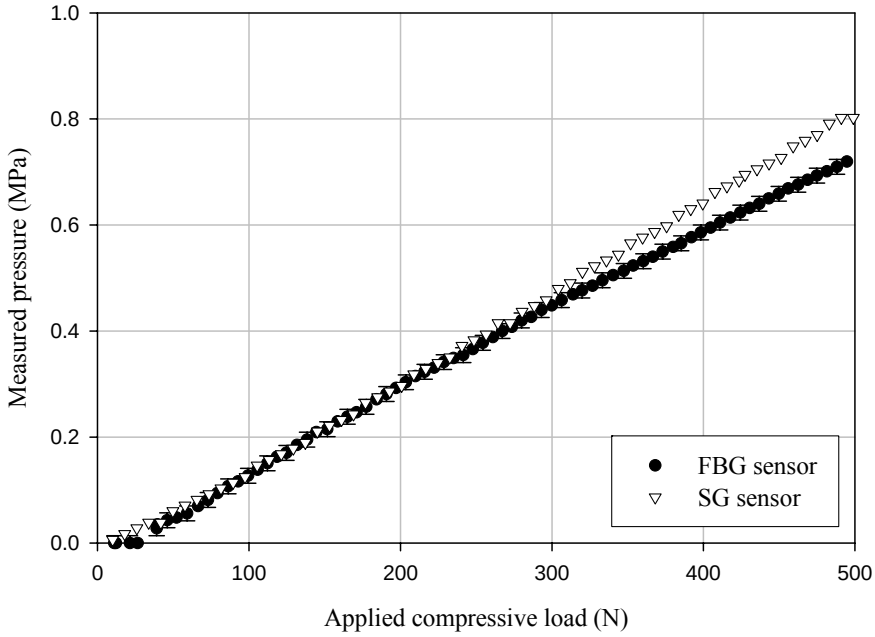

Figure 12: Example data of FBG and SG sensor measured pressure versus compressive load on one porcine FSU. Regression-calculated slope of data is termed the disc response to load (kPa/N). Maximum measured pressure is measured pressure at 500 N compressive load. Vertical error bars on FBG sensor data (± 0.014 MPa) calculated as the standard error in pressure measurement from the FBG sensor calibration experiments. Horizontal error bars (± 5.6 N) were not clearly visible at the given scale but they reflect the accuracy of load cell.

IVD pressure measurements performed using the FBG sensor showed excellent repeatability (Table 1). For sensor insertions 1 through 3, respectively, the relative difference in the disc response to load between load cycle 1 and 2 was only 0.4%, 6.5%, and 1.0% with similar results for the maximum measured pressure.

Table 2 shows the results obtained from both the FBG and SG sensors from three insertion locations within the IVD. The relative difference in the disc response to load for insertions 1 through 3 respectively are 28.4%, 3.73%, and 1.98%. For the maximum measured pressure the relative differences were respectively 37.7%, 6.00%, and 1.99%.

Table 1: Regression calculated disc response to load (kPa/N) with standard deviation (SD), coefficient of determination (r^2), and maximum measured pressure for the IVD pressure data obtained in the repeatability study. Row-headers 1 through 3 correspond to each FBG insertion location in the IVD.

Location		Disc response to load (kPa/N) (mean ± SD)	(r^2)	Maximum pressure measured (MPa)
1	Cycle 1	2.78±2.18E-3	0.99	1.52
	Cycle 2	2.79±3.11E-3	0.99	1.52
2	Cycle 1	2.94±1.39E-3	0.99	1.48
	Cycle 2	2.76±2.79E-3	0.99	1.49
3	Cycle 1	3.20±1.87E-3	0.99	1.63
	Cycle 2	3.17±1.62E-3	0.99	1.59

Table 2: Regression calculated disc response to load (kPa/N) with standard deviation (SD), coefficient of determination (r^2), and maximum measured pressure for the IVD pressure data obtained using the FBG and SG sensors. Data shown for each insertion location is averaged from three measurements.

Location	Disc response to load (kPa/N) (mean ± SD)		(r^2)		Maximum pressure measured (MPa)	
	FBG	SG	FBG	SG	FBG	SG
1	2.67±2.34E-3	2.08±3.77E-4	0.98	0.99	1.46	1.06
2	2.84±1.66E-3	2.95±1.93E-3	0.99	0.97	1.41	1.50
3	3.09±5.38E-3	3.03±1.35E-3	0.92	0.99	1.48	1.51

5. Discussion

A key strength of this work is that the FBG sensor has a sensitivity (*i.e.* -21.5 pm/MPa) approximately 7 times greater than that of a bare-FBG sensor (-3.1 pm/MPa) while maintaining extremely small size (400 μm major diameter) and high spatial resolution by limiting the sensing region to the probe tip. This is an improvement relative to other FBG sensors presented in the literature that employ mechanical amplification schemes that significantly increase their length or major diameter. Examples include the glass sphere FBG sensor of Xu *et al.* (1996) that has major diameter of 5.5 mm and sensitivity 4 times greater than a bare-fibre [43]. Liu *et al.* (2000) present a polymer

coated FBG sensor with a major diameter of 15 mm, length of 50 mm and sensitivity 30 times that of a bare fibre [44]. Sheng *et al.* (2004) and Zhang *et al.* (2001) report sensitivities 10,900 and 1,720 times greater than a bare for polymer coated sensors with major diameters of 22 mm and 13 mm, respectively [13, 14]. In the context of biomedical pressure measurement applications these sensors are too large for *in vivo* applications and could have limited utility in *ex vivo* experiments for the same reasons already attributed to the needle mounted strain-gage sensor.

Intervertebral disc pressure measurements performed using the FBG also show excellent repeatability (average 2.6 % error between measurements) and agreement to those obtained using the strain-gage sensor (average difference of 11.37 % in disc response to load).

This sensor is also smaller than all previously reported IVD pressure sensors of which the smallest had a 1.3mm diameter [18]. Therefore it has the potential to address the limitations associated with needle mounted sensors because of its small size and its mechanical compliance**.** Unlike the large (1.3 mm to 3 mm diameter) and rigid needle mounted sensors, the FBG sensor could be used in discs with small disc height such as in the cervical spine or in degenerated discs. In cervical spine specifically there is a paucity of experimental data; therefore there is potential contribute new understanding of the biomechanics in this less-studied region of the spine.

6. Conclusions

In this paper we describe the design of a FBG pressure sensor that has pressure sensitivity much greater than that of a bare FBG while maintaining both small size and mechanical compliance. We also present a theoretical model and experimental calibration

results to validate its sensitivity to hydrostatic pressure. The model includes both a strain-optic model based on the τ-matrix approach of calculating FBG reflection spectra for non-uniform strain fields as well as a structural finite-element model designed to predict the strains throughout the sensor. The FBG sensor was applied to intervertebral disc pressure measurements in a cadaveric porcine functional spinal unit and the results obtained were compared to measurements made with the current standard strain-gage sensor that has been widely used for disc pressure measurements. Intervertebral disc pressure measurements performed using the FBG also show excellent repeatability and agreement to those obtained using the strain-gage sensor.

References

[1] Pieter, L. S., Beatrys, M. L., and Anatoli, A. C., 2005, "Chirped fiber Bragg grating sensor for pressure and position sensing," SPIE, p. 054402.

[2] Udd, E., Lawrence, C., and Nelson, D., 1997, "Development of a Three Axis Strain and Temperature Fiber Optic Grating Sensor," Proceedings of SPIE, 3042, pp. 229-236.

[3] Xu, M. G., Reekie, L., Chow, Y. T., and Dakin, J. P., 1993, "Optical in-fibre grating high pressure sensor," Electronics Letters, 29, pp. 398-399.

[4] Yeo, T. L., Sun, T., Grattan, K. T. V., Parry, D., Lade, R., and Powell, B. D., 2005, "Characterisation of a polymer-coated fibre Bragg grating sensor for relative humidity sensing," Sensors and Actuators B: Chemical, 110, pp. 148-155.

[5] Fernandez, A. F., Brichard, B., Berghmans, F., and Decreton, M., 2002, "Dose-Rate Dependencies in Gamma-Irradiated Fiber Bragg Grating Filters," IEEE Transactions on Nuclear Science, 49(6), pp. 2874-2878.

[6] Udd, E., 1991, Fibre Optic Sensors, An Introduction for Engineers and Scientists, Wiley InterScience.

[7] Measures, R. M., 2001, Structural Health Monitoring with Fiber Optic Technology, Academic Press.

[8] Hao-Jan, S., Ming-Yue, F., Tzu-Chiang, C., Chia-Min, L., Wen-Fung, L., and Sheau-Shong, B., 2004, "High-sensitivity pressure sensor based on a fiber Bragg

grating," C. Brian, A. M. Michael, P. D. John, D. C. Samuel, and E. K. Helmut, eds., SPIE, pp. 248-254.

[9] Liu, L., Zhao, Q., Zhang, W., Zhang, H., Jin, L., Zhao, L., Yan, Y., and Gao, S., 2005, "Fiber Grating Pressure Sensor with Enhanced Sensitivity," Proceedings of SPIE, 5623, pp. 16-19.

[10] Ngoi, B. K. A., Paul, J., Zhao, L. P., and Fang, Z. P., 2004, "Enhanced lateral pressure tuning of fiber Bragg gratings by polymer packaging," Optics Communications, 242, pp. 425-430.

[11] Maier, R. R. J., Barton, J. S., Jones, J. D. C., McCulloch, S., and Burnell, G., 2003, "Dual-fibre Bragg grating sensor for barometric pressure measurement," Measurement Science and Technology, 14, pp. 2015-2020.

[12] Liu, Y., Guo, Z., Zhang, Y., Seng, K., Dong, C., and Dong, X., 2000, "Simultaneous pressure and temperature measurement with polymer-coated fibre Bragg grating," Electronics Letters, 36(6), pp. 564-566.

[13] Sheng, H.-J., Fu, M.-Y., Tzu-Chiang, C., Wen-Fung, L., and Sheau-Shong, B., 2004, "A lateral pressure sensor using a fiber bragg grating," IEEE Photonics Technology Letters, 16(4), pp. 1146-1148.

[14] Zhang, Y., Feng, D., Liu, Z., Guo, Z., Dong, X., Chiang, K. S., and Chu, B. C. B., 2001, "High-sensitivity pressure sensor using a shielded polymer-coated fiber Bragg grating," IEEE Photonics Technology Letters, 13(6), pp. 618-619.

[15] Mignani, A. G., and Baldini, F., 1996, "Biomedical sensors using optical fibres," Rep. Prog. Phys., 59, pp. 1-28.

[16] Dennison, C. R., Wild, P. M., Byrnes, P. W. G., Saari, A., Itshayek, E., Wilson, D. C., Zhu, Q. A., Dvorak, M. F. S., Cripton, P. A., and Wilson, D. R., 2008, "*Ex vivo* measurement of lumbar intervertebral disc pressure using fibre-Bragg gratings," Journal of Biomechanics, 41(1), pp. 221-225.

[17] Nachemson, A., 1960, "Lumbar Intradiscal Pressure," Acta Orthopaedica Scandinavica supplementum, 43, pp. 1-104.

[18] Josef Pospiech, M. D. D. S., M.D.; Hans J. Wilke, Ph.D; Lutz E. Claes, Ph.D, 1999, "Intradiscal Pressure Recordings in the Cervical Spine," Neurosurgery, 44, pp. 379-384.

[19] Steffen, T., Baramki, H. G., Rubin, R., Antoniou, J., and Aebi, M., 1998, "Lumbar intradiscal pressure measured in the anterior and posterolateral annular regions during asymmetrical loading," Clinical Biomechanics, 13, pp. 495-505.

[20] S. Hattori, H. O., S. Kawai, Ube-Shi, 1981, "Cervical Intradiscal Pressure in Movements and Traction of the Cervical Spine," Zeitschrift Fur Orthopadic, 119, pp. 568-569.

[21] Yantzer, B. K., Freeman, T. B., Lee, W. E., Nichols, T., Inamasu, J., Guiot, B., and Johnson, W. M., 2007, "Torsion-induced pressure distribution changes in human intervertebral discs," Spine, 32(8), pp. 881-884.

[22] Wilke, H.-J., Neef, P., Caimi, M., Hoogland, T., and Claes, L. E., 1999, "New in vivo measurements of pressures in the intervertbral disc in daily life," Spine, 24(8), pp. 755-762.

[23] Schmidt, H., Kettler, A., Heuer, F., Simon, U., Claes, L., and Wilke, H.-J., 2007, "Intradiscal pressure, shear strain, and fiber strain in the intervertebral disc under combined loading," Spine, 32(7), pp. 748-755.

[24] Panjabi, M. M., and White, A. A., 2001, Biomechanics in the muscoloskeletal system, Churchill Livingstone.

[25] A. Nachemson, M. D., 1966, "The Load on Lumbar Disks in Different Positions of the Body," Clinical Orthopaedics and Related Research, 45, pp. 107-122.

[26] Alf Nachemson, M. D. J. M. M., 1964, "In Vivo Measurements of Intradiscal Pressure," Journal of Bone and Joint Surgery, American Volume 46-A, pp. 1077-1092.

[27] Bryan W. Cunningham, M. Y. K., MD; Patrick S. McNulty, MD; Andrew Cappuccino, MD; Paul C. McAfee, MD, 1997, "The Effect of Spinal Destabilization and Instrumentation on Lumbar Intradiscal Pressure," SPINE, 22(22), pp. 2655-2663.

[28] Mark A. Fye, E. P. S., Manohar M. Panjabi, Jacek Cholewicki, 1998, "Quantitative Discomanometry:

Technique and Reproducibility In Vitro," Journal of Spinal Disorders, 11(4), pp. 335-340.

[29] McNally, D. S., and Adams, M. A., 1992, "Internal intervertebral disc mechanics as revealed by stress profilometry," Spine, 17, pp. 66-73.

[30] Hans-Joachim Wilke, S. W., Lutz E. Claes, Markus Arand, Alexander Wiesend, 1996, "Influence of Varying Muscle Forces on Lumbar Intradiscal Pressure: An In Vitro Study," Journal of Biomechanics, 29, pp. 549-555.

[31] Adams, M. A., McNally, D. S., and Dolan, P., 1996, "'Stress' Distributions Inside Intervertebral Discs," The Journal of Bone and Joint Surgery, 78-B(6), pp. 965-972.

[32] Seo, K.-S., Derby, R., Date, E. S., Lee, S.-H., Kim, B.-J., and Lee, C.-H., 2007, "In vitro measurement of pressure differences unsing manometry at various injection speeds during discography," The Spine Journal, 7, pp. 68-73.

[33] P.A. Cripton, G. A. D., L.-P. Nolte, 2001, "A minimally disruptive technique for measuring intervertebral disc pressure in vitro: application to the cervical spine," Journal of Biomechanics, 34, pp. 545-549.

[34] Wild, P., and Dennison, C., 2007, "Pressure sensor for biological fluids and use thereof, US PCT No. 070213."

[35] Norton, R. L., 2000, Machine Design, An integrated approach, Prentice Hall.

[36] Huang, S., LeBlanc, M., Ohn, M. M., and Measures, R. M., 1995, "Bragg intragrating structural sensing," Applied Optics, 34(22), pp. 5003-5009.

[37] Weller-Brophy, L. A., and Hall, D. G., 1985, "Analysis of waveguide gratings: application of Rouard's method," Journal of the Optical Society of America A, 2(6), pp. 863-871.

[38] Poladian, L., 1993, "Graphical and WKB analysis of nonuniform Bragg gratings," Physical Review E, 48(6), pp. 4758-4767.

[39] Hill, K. O., 1974, "Aperiodic distributed-parameter waveguides for integrated optics," Applied Optics, 13(8), pp. 1853-1856.

[40] Nunes, L. C. S., Valente, L. C. G., Llerena, R. W. A., Braga, A. M. B., and Triques, A. L. C., 2004, "Simultaneous measurement of temperature and pressure using single fiber Bragg grating and fixed filter demodulation technique," Proceedings of SPIE, 5622, pp. 906-911.

[41] 2001, "Corning SMF-28 optical fibre: Product Information," Corning Incorporated, Midland MI, www.corning.com/opticalfibre.

[42] Issachar Gilad, P., and Moshe Nissan, P., 1986, "A Study of Vertebra and Disc Geometric Relations of the Human Cervical and Lumbar Spine," SPINE, 11(2), pp. 154-157.

[43] Xu, M. G., Geiger, H., and Dakin, J. P., 1996, "Fibre grating pressure sensor with enhanced sensitivity using a glass-bubble housing," Electronics Letters, 32, pp. 128-129.

[44] Liu, Y., Guo, Z., Ztiang, Y., Cliiang, K. S., and Dong, X., 2000, "Simultaneous pressure and temperature measurement with polymer-coated fibre Bragg grating," Electronics Letters, 36(6), pp. 564-566.

Appendix B: Validation of a novel minimally invasive intervertebral disc pressure sensor utilizing in-fibre Bragg grating in a porcine model: An *ex vivo* study

(IN PRESS)

Will appear in Spine, Volume 33, Issue 16, August 2008.

Validation of a novel minimally invasive intervertebral disc pressure sensor utilizing in-fibre Bragg gratings in a porcine model: An *ex vivo* study

Chris R. Dennison[a], Peter M. Wild[a], Marcel F. Dvorak[b], David R. Wilson[c], and Peter A. Cripton[c,d]

[a] *Department of Mechanical Engineering, University of Victoria, Canada*
Divisions of [b]*Orthopaedic Spine Surgery and* [c]*Orthopaedic Engineering Research , Department of Orthopaedics, University of British Columbia, Vancouver Canada*
[d]*Department of Mechanical Engineering, University of British Columbia, Vancouver, Canada*

Corresponding Author:
Christopher R. Dennison, B.Eng
Department of Mechanical Engineering
University of Victoria
P.O. Box 3055
Victoria, B.C.
V8W 3P6
Ph: (250) 853-3198
Fax: (250) 721-6051
e-mail: dennison@uvic.ca

Structured Abstract

Study Design

Nucleus pressure was measured within porcine intervertebral discs (IVDs) with a novel in-fibre Bragg grating (FBG) sensor (0.4 mm diameter) and a strain gauge (SG) sensor (2.45 mm) to validate the accuracy of the FBG sensor.

Objective

To validate the accuracy of a new FBG pressure sensor we have designed and constructed for minimally invasive measurements of nucleus pressure.

Summary of Background Data

Although its clinical utility is controversial, it is possible that the predictive accuracy of discography can be improved with IVD pressure measurements. By virtue of their size

SG sensors alter disc mechanics, injure annulus fibres, and can potentially initiate or accelerate degenerative changes thereby limiting their utility particularly clinically.

Methods

Six functional spinal units were loaded in compression from 0 N to 500 N and back to 0 N; nucleus pressure was measured using the FBG and SG sensors at various locations along anterior and right and left antero-lateral axes.

Results

On average maximum IVD pressures measured using the FBG and SG sensors were within 9.39% of each other. However, differences between maximum measured pressures from the FBG and SG sensors were larger (22.2%) when the SG sensor interfered with vertebral endplates ($p<0.05$). The insertion of the FBG sensor did not result in visible damage to the annulus, whereas insertion of the SG sensor resulted in large perforations in the annulus through which nucleus material was visible.

Conclusions

The new FBG sensor is smaller and less invasive than any previously reported disc pressure sensor and gave results consistent with previous disc pressure studies and the SG sensor. There is significant potential to use this sensor during discography while avoiding the controversy associated with disc injury as a result of sensor insertion.

Key Words: spine, intervertebral disc, back pain, discography, nucleus pulposus, disc degeneration, pressure sensor

Key Points:

- Nucleus pressure measured using the FBG sensor showed good agreement to pressure measurements made with the SG sensor
- The FBG sensor did not interfere with vertebral endplates upon insertion, However, the SG sensor did interfere with the endplates and this confounded the associated pressure measurements

- This FBG sensor is 83% smaller and more flexible than any previously reported disc pressure sensor and could potentially be used to improve accuracy of discography while minimizing trauma to the annulus fibrosus

1. Introduction

Acute back pain, a widespread problem affecting the population of industrialized societies, is at least partially caused by intervertebral disc (IVD) degeneration or other pathologies in the form of annular tears or prolapses. It is estimated that 70% of the population will experience back pain in their lives [1] and back pain is among the most frequent causes of workplace absenteeism in North America [2, 3]. The development of symptomatic disc degeneration is a multi-factorial process in which disc mechanics plays an important role [4, 5]. Therefore, understanding human IVD mechanics is central to understanding the etiology of disc degeneration [6]. Pressure distributions in IVDs are an important indicator of disc mechanics that have been measured both *in vivo* [7, 8] and *ex vivo* [6, 9-12]. In the lumbar spine, disc pressure increases linearly with applied compressive load and is hydrostatic in healthy discs [6], while in degenerated discs this hydrostatic behaviour is disrupted [13].

In an attempt to improve the outcomes of spinal fusion for degenerative disc disease, provocative discography has been used to determine whether a specific disc is a potential source of acute pain [14]. Although pain provocation and the morphological appearance of the disc have been widely utilized, the measurement of disc pressures is not widely used in part due to the limitations of current disc pressure measurement technology. Investigators have sought to improve the predictive accuracy of discography by performing pressure measurements using needle mounted strain gauge (SG) sensors [14]. These SG sensors have been used both *ex vivo* and *in vivo* [2, 3, 15-17]. These SG

sensors are housed in large needles (20 gauge to 11 gauge) that injure the fibres of the annulus and alter the mechanics of the IVD [14]. In experimental models with disc heights comparable to the sensor diameter (e.g. porcine or human cervical discs), these sensors can interfere with the vertebral endplates and other anatomic features such as the uncinate processes and inferior protuberance [14, 18]. These drawbacks limit the utility of the sensors for *ex vivo* research and have long term effects on disc health and degeneration [2, 14]. These long term effects have limited the utility of pressure measurements in conjunction with the other aspects of discography to mainly *ex vivo* experiments [14].

An emerging fibre-optic strain measurement technology, in-fibre Bragg gratings (FBGs), has the potential to overcome some of these limitations. FBGs consist of an optical fibre (0.125 mm diameter) with a Bragg grating photo-inscribed into a short length of the optical fibre core. FBGs have excellent potential for biomechanical applications because they are small, mechanically compliant, immune to electromagnetic interference, and biocompatible. They can be implanted in regions of the IVD where anatomic features may otherwise prevent sensor insertion and, because of their size, they will minimize the injury to annular fibres and the affect on disc mechanics. FBGs are commonly used to measure physical parameters such as strain [19, 20], temperature [21-23], and pressure [24-26]. We recently used bare FBG and SG sensors to measure IVD pressure in human cadaveric specimens [27]. Results obtained using the bare FBG sensor agreed with those found in previous studies but not with measurements conducted using the SG sensor. We hypothesized that the disagreement was caused primarily by nucleus material inhomogeneity which could have disrupted hydrostatic behaviour within the

nucleus and over the 10 mm length of the FBG would also disrupt pressure measurement [27]. In this study we have constructed a new FBG sensor, suitable for mapping pressure distributions, with increased spatial resolution as compared to the bare FBG that will not be affected by nucleus inhomogeneity because the sensor's active sensing region is limited to a circular plane of only 0.4 mm diameter.

The objectives of the current study were: a) to assess the linearity, sensitivity and hysteresis of a new FBG sensor that we have constructed; b) to develop methods for calibrating the new FBG sensor and for implanting it in IVDs and c) to determine the accuracy of the new FBG sensor in measurements of disc pressure as a function of compressive load in six porcine functional spinal units.

2. Materials and methods

Six porcine cadaveric functional spine units (FSUs) were obtained from two lumbar spines that were harvested fresh. The FSUs were prepared by stripping muscle tissue while maintaining disc and ligaments. The vertebrae of each FSU were embedded in dental cement and the intervertebral discs were kept free. Anterior and antero-lateral sensor insertion was performed in a configuration similar to that described in Adams, McNally, and Dolan [13].

We constructed a new FBG sensor (Figure 1) with a diameter of 0.4 mm (27 gauge). The 50 mm long probe (Figure 1) has an outer housing made of a hypodermic stainless steel tube with a major diameter of 0.4 mm (27 gauge). An optical fibre (0.125 mm diameter) with a single FBG (10mm length, Blue Road Research, Gresham OR) was positioned inside the tube such that the FBG is at the end of the probe (Figure 1, Section

A-A). A compliant silicone sealant (Dow Corning 3140 RTV, Midland MI) occupied the annular volume between the steel tube and the FBG (Figure 1, Section A-A).

In this sensor configuration, pressure applied to the active sensing region (Figure 1, Section A-A) causes deflections within the silicone sealant which induce strains in the FBG. Strains in the FBG induce changes in the characteristic wavelength of light reflected from the FBG. The optical principles governing this process are described in Udd (1991) [28]. The design of the FBG sensor described above is provisionally patented (US Provisional Patent Application No. 60/766,600 and PCT/CA2007/000286).

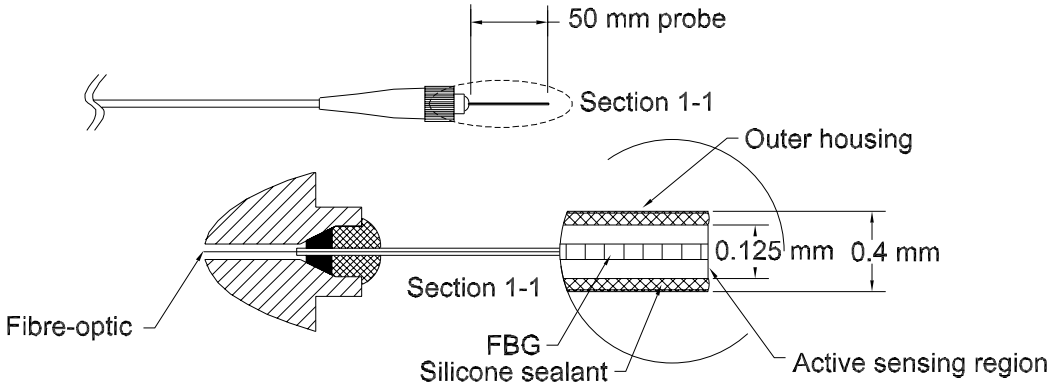

Figure 1: Schematic diagram of FBG pressure sensor. This new FBG sensor was constructed with a 50 mm probe that houses the FBG and a compliant silicone seal that occupies the annular volume between the 0.4 mm tubing and the FBG (Section A-A). The active sensing region is limited to the tip of the probe.

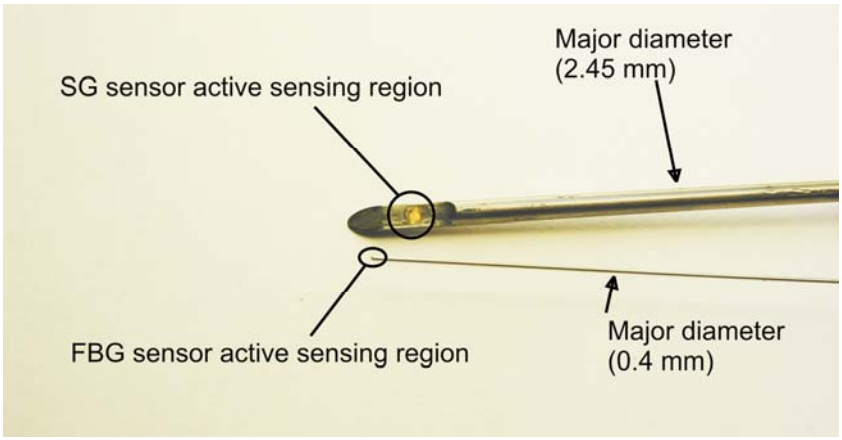

Figure 2: Relative lengths of the active sensing regions and probe diameters for both the SG and FBG pressure sensors.

The FBG sensor was calibrated between 0 MPa to 2 MPa in a custom calibration apparatus. We also calibrated a strain gauge (SG) sensor (Model 060S; pressure range, 0-3.5 MPa; Precision Measurement Company, Denton, Ann Arbor USA). The SG sensor had a major probe diameter of 2.45 mm and an active sensing region located near the end of the probe (Figure 2).

We aligned each FSU in a materials testing machine (Instron 8874, Norwood MA) and then performed three preconditioning loading cycles, consisting of loads from 0 N to 500 N to 0 N at a rate of 40 N/s. The displacements of the superior vertebrae were visually monitored to verify that torsions were not applied to the disc.

Prior to FBG sensor insertion, the outer annulus was pierced by inserting a 25 gauge (0.51 mm major diameter) hypodermic needle to an approximate depth of 3 mm past the outside surface of the annulus. The hypodermic needle was used first because it had a cutting tip and the FBG sensor did not. The 25 gauge hypodermic needle was then withdrawn, and the FBG sensor was inserted into the hole just created. The FBG sensor probe was advanced through the annulus into the nucleus. The sensor was then positioned to a depth equal to one-half the diameter of the intervertebral disc (IVD) along the insertion axis (Figure 3a). Finally, a reference mark was made on the FBG sensor probe where it emerged from the annulus. The location of the reference mark relative to the outside of the annulus was visually monitored to ensure that the FBG sensor location was held constant throughout each test.

We then loaded the FSU in compression using a saw-tooth loading profile from 0N to 500N, with a one second hold at 500 N, and then back to 0N, at a 40N/s loading rate for both loading and unloading phases. Applied compressive force was measured using a

calibrated load cell (Sensor Data M211-113, Sterling Heights MI). Pressure was measured using the FBG sensor and a Bragg-grating filter, similar to that described in Nunes *et al.* (2004),[22] throughout the entire range of applied loads continuously at 40 Hz.

After testing with the FBG sensor, we removed the FBG sensor and inserted a SG sensor positioning it at the center of the nucleus. The sensor was inserted through the same hole in the outer annulus, and using the same procedure as was previously used for the FBG sensor. In some instances, interference between the SG sensor and the vertebral endplates caused movement of the superior vertebra from its nominal unloaded position. In each instance of the interference, the specimen number and insertion axis was recorded prior to taking pressure measurements. We loaded each disc using the same protocol used with the FBG sensor.

The FBG and SG sensor insertion procedure described above was performed along three separate insertion axes in each FSU as shown in Figure 3b. Pressure was measured as a function of compressive load along one anterior axis, and along the two antero-lateral axes from the left and right sides of the intervertebral disc (Figure 3b). After each loading cycle, the sensors were removed and re-inserted into the IVD along a different insertion axis. This process was repeated until three sets of pressure data were obtained for each insertion axis in all specimens for both the FBG and SG sensors.

We also verified that our FBG sensor produced repeatable results by performing multiple pressure measurements over multiple cycles of loading within a single IVD while the FBG sensor location remained fixed. The insertion was conducted as described above, and the FSU was subsequently loaded and pressure data were acquired. After this

first load cycle the FBG instrumentation was powered-down, and subsequently power was restored. The instrumentation settings were re-established and the FSU was loaded again while pressure data was acquired. This procedure was performed along all three insertion axis using a single FSU.

Linear regression was performed on the disc pressure data (example FBG data shown in Figure 4) obtained from both the FBG and SG sensors using SigmaPlot™. Coefficients of determination (r^2) and the disc response to load (kPa/N) (i.e. the slope of the pressure versus force data) were determined for each data set. We also tested the hypothesis that the differences between FBG and SG sensor maximum measured pressures, between the cases where SG interference with vertebral endplates did and did not occur, were distributed about the same mean difference by conducting a heteroscedastic t-test.

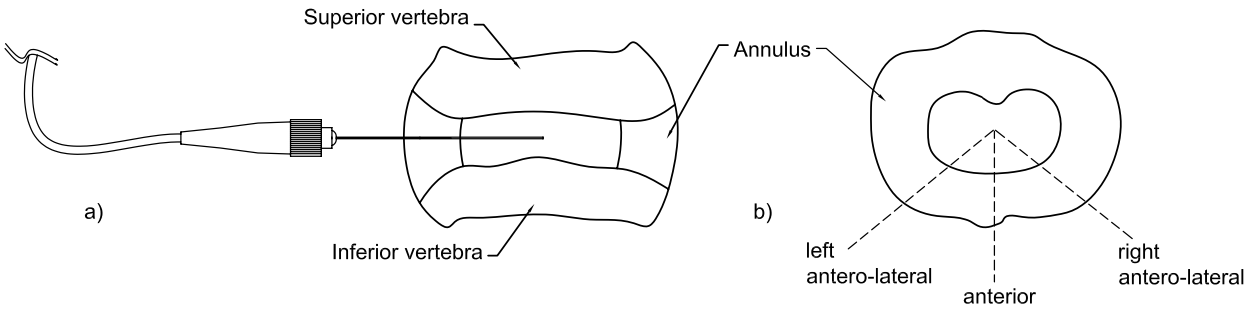

Figure 3: a) schematic showing sagittal cross-section of IVD and the geometry of sensor insertion within the IVD; and b) schematic showing superior view of mid-IVD cross section and the sensor insertion axes (anterior and left and right antero-lateral).

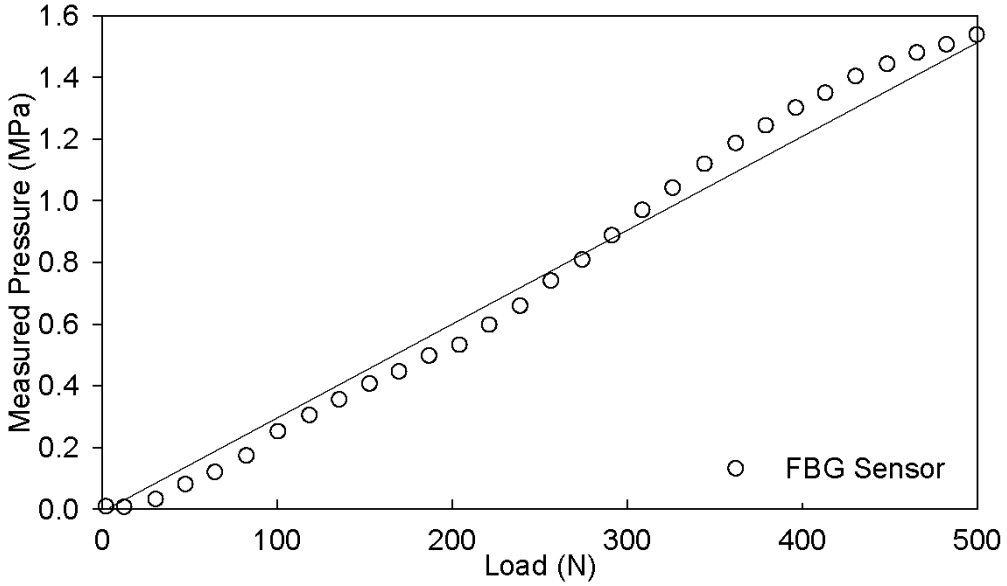

Figure 4: Example data for FBG measured pressure versus compressive load showing maximum measured pressure at 500 N and regression line. Slope of regression line is reported as disc response to load (kPa/N).

3. Results

3.1 FBG sensor calibration

The mean sensitivity to pressure, from the calibration data acquired before the *ex vivo* experiments was -22.7 ± 1.5E-5 mV/MPa (mean ± S.D.). The coefficients of determination (r^2) for the calibration data sets were always greater than 0.99, and the mean hysteresis in the calibration data was 2.24% of the full scale sensor response.

3.2 Intervertebral disc pressure measurements

Pressure measurements made with the FBG sensor in one specimen (specimen 3) showed good repeatability (Table 1). For the left antero-lateral insertion axis, the difference in the disc response to load between cycles 1 and 2 was 0.36%, and the maximum measured pressures were identical (within the resolution of the sensor). For the right antero-lateral axis, the difference in the disc response to load between cycles 1 and 2 was 6.1%, and for the maximum measured pressure was 0.68%. For the anterior

insertion axis the difference in the disc response to load between cycles 1 and 2 was 0.94%, and for the maximum measured pressure the difference in the disc response was 2.5%

For both the FBG and SG sensors disc pressure varied linearly with applied compressive load (Table 1 and 2). The mean coefficient of determination (r^2) for the FBG was 0.97 and ranged from 0.90 to 0.99, while for the SG the mean coefficient of determination was 0.99 with a range from 0.97 to 0.99.

Table 1: FSU response to load (kPa/N), coefficient of determination (r^2), and maximum measured pressure (MPa) obtained from the FBG sensor repeatability study. All measurements were performed using specimen 3, L5 37 mm major diameter.

Insertion axis		Disc response to load (kPa/N) (mean ± SD)	Coefficient of determination (r^2)	Maximum pressure measured (MPa)
left antero-lateral	Cycle 1	2.78±2.18E-3	0.99	1.52
	Cycle 2	2.79±3.11E-3	0.99	1.52
right antero-lateral	Cycle 1	2.94±1.39E-3	0.99	1.48
	Cycle 2	2.76±2.79E-3	0.99	1.49
anterior	Cycle 1	3.20±1.87E-3	0.99	1.63
	Cycle 2	3.17±1.62E-3	0.99	1.59

Pressure measurements made with the FBG sensor showed good agreement with those made with the SG sensor when interference between the vertebral endplates and SG sensor did not occur (Table 2). The mean relative difference between the disc response to load for the FBG sensor and SG sensor results was 9.39% and ranged from 0.424% to 33.2% for results where SG interference was not observed. The mean relative difference between the FBG sensor and SG sensor maximum measured pressure was 9.11% and ranged from 1.35% to 35.2%.

The results obtained from the FBG and SG sensors did not generally agree when the SG sensor interfered with vertebral endplates (Table 2). Considering only these results, the mean difference in the disc response to load was 21.4% and ranged from

9.06% to 28.4%, and for the maximum measured pressure the mean difference was 22.2% and ranged from 12.3% to 30.4%.

In some specimens we noticed a decrease in the maximum disc pressure measured after the initial insertion of the SG sensor. In specimens 1, 4, and 6, insertion of the SG sensor eventually resulted in an apparent decrease in the maximum disc pressure. In specimen 1, the left antero-lateral axis was used first with the FBG sensor and subsequent measurements using both the FBG and SG sensors show a drop in the maximum measured pressure when SG interference was not noted. A similar trend was observed in specimen 4, where the SG sensor was first used on the left antero-lateral axis; subsequently, when interference was not noted along the anterior axis, the maximum disc pressure was reduced. This trend is repeated in specimen 6 where the SG sensor was first used along the right antero-lateral axis.

The results of the heteroscedastic t-test showed that on average the differences in maximum measured pressure obtained from the FBG and SG sensors when interference was not observed, 9.39%, were statistically lower than the differences when interference did occur, 22.2% ($p<0.05$).

After the FBG sensor was withdrawn from the annulus, the location of sensor insertion was visually indistinguishable from the rest of the annulus. However, after SG sensor insertion and withdrawal, a circular perforation was noted in the annulus at the insertion site (Figure 5). In some cases, nucleus material was observed extruding from these perforations after multiple loading cycles.

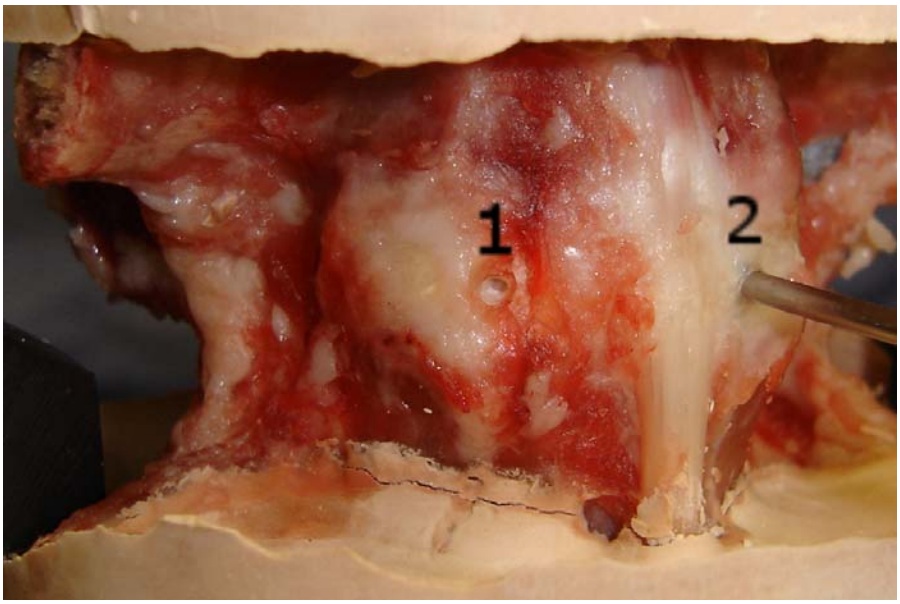

Figure 5: Left antero-lateral view of porcine intervertebral disc showing perforation (location 1) left in annulus as a result of SG (location 2) sensor insertion.

4. Discussion

We developed a new intervertebral disc pressure sensor employing in-fibre Bragg gratings that has a small major diameter (0.4 mm) as compared to previously reported disc pressure sensors of which the smallest had a diameter of 1.3 mm [2, 15, 16, 18]. We attempted to validate the accuracy of the FBG sensor by comparing pressure measurements made with the FBG sensor to those made with a needle mounted SG sensor used in previous studies.

Pressure measurements made with the FBG sensor showed good agreement with SG sensor results. The linear variation in intervertebral disc pressure with increasing and decreasing compressive load obtained from the FBG-measured pressure data was consistent with the results obtained from the SG sensor. The observed linear FSU response to load is also consistent with previous studies using different types of sensors [6, 11, 18]. Nachemson (1960) measured nucleus pressure in human cadaveric

specimens and found a disc pressure response to load of 0.840 kPa/N in a L2-L3 specimen. McNally and Adams measured a disc response to load of 1.00 kPa/N (L2-L3 human specimen), and Cripton *et al.* (2001) measured disc responses to load ranging from 3.00 kPa/N to 4.38 kPa/N, with coefficients of determination exceeding 0.99, in human cervical specimens. Our results for disc response to load in porcine lumbar specimens are higher than those reported above for human lumbar specimens, but generally fall below those from human cervical specimens reported by Cripton *et al.* (2001). A possible explanation for this is the well-known inverse relationship between IVD pressure and disc cross-sectional area [6]. Our lumbar specimens did have lateral diameters smaller than those reported for human lumbar discs (mean: 55.9 mm) [29] but larger than those reported for human cervical discs (mean: 20 mm) [30].

The consistency of results with previous studies and between load cycles in the current study also represents a significant improvement from the results obtained in our previous study where we used bare FBGs (10 mm in length) in human cadaveric discs.[27] These previous results did not generally agree with those from the SG sensors, partially due to poor spatial resolution of pressure measurements using the bare 10 mm FBGs. The new FBG sensor that we report in the current study has increased spatial resolution because its active sensing region is limited to the end of the probe (0.4 mm diameter).

We have not found any studies in the literature that attempt to measure effects on disc pressure due to sensor insertion and interference with disc structures. However, our results suggest interference between the vertebral endplates and the SG sensor may explain the majority of results showing disagreement between the FBG and SG sensor

measured disc pressure. We hypothesize that interference of the SG sensor with the vertebral endplates could have caused load transmission through the SG sensor instead of the annulus and nucleus thereby resulting in reduced disc pressure.

Our results also suggest that, in some specimens, the SG sensor damages the disc in such a way that its mechanics are disrupted. Decreases in maximum disc pressure after initial insertion of the SG sensor, found in three of the six specimens used in this study, is not outlined in the current literature. However our results indicate damage as a result of SG sensor insertion; the annular perforations mentioned previously could compromise the ability of the nucleus to sustain hydrostatic pressure and result in load transfer to the annulus.

A key strength of our work is that the new FBG sensor has the potential to address the limitations associated with needle mounted sensors because of its small size and its mechanical compliance and therefore could potentially be used to make minimally invasive measurements of disc pressure in vivo and during discography. A limitation of the current study is that we have not directly tested whether the SG sensor transmitted load between the vertebrae when we observed interference. This motivates future work on the SG sensor's influence on disc displacements and rotations.

Table 2: Mean values for disc response to load (kPa/N), coefficient of determination (r^2), and maximum measured pressure (MPa) along each sensor insertion axis. Disc diameter and observations of SG interference are also tabulated.

Specimen	Level	Major Disc Diameter (mm)		Disc response to load[1] (kPa/N) (mean ± SD)		Coefficient of determination[1] (r^2)		Maximum pressure measured[1] (MPa)		Disc distraction[2] (Yes/No)
				FBG	SG	FBG	SG	FBG	SG	
1	L3	36.2	left antero-lateral	3.06±2.36E-3	2.19±3.83E-4	0.99	0.99	1.58	1.10	Yes
			right antero-lateral	1.60±1.51E-3	2.08±2.36E-4	0.98	0.99	0.767	1.04	No
			anterior	1.82±1.30E-3	1.93±4.52E-4	0.99	0.99	0.901	0.980	No
2	L1	37.2	left antero-lateral	3.58±2.73E-3	2.61±1.94E-3	0.98	0.97	1.68	1.39	Yes
			right antero-lateral	2.79±2.09E-3	2.27±5.34E-4	0.98	0.99	1.42	1.19	Yes
			anterior	2.85±2.97E-3	2.69±4.18E-4	0.98	0.99	1.57	1.37	No
3	L5	37.0	left antero-lateral	2.67±2.34E-3	2.08±3.77E-4	0.98	0.99	1.46	1.06	Yes
			right antero-lateral	2.84±1.66E-3	2.95±1.93E-3	0.99	0.97	1.41	1.50	No
			anterior	3.09±5.38E-3	3.03±1.35E-3	0.92	0.99	1.48	1.51	No
4	L3	37.5	left antero-lateral	3.19±1.25E-3	2.33±4.72E-4	0.99	0.99	1.62	1.20	Yes
			right antero-lateral	2.78±3.17E-3	2.31±2.44E-4	0.97	0.99	1.47	1.16	Yes
			anterior	2.34±1.90E-3	2.30±4.47E-4	0.98	0.99	1.11	1.15	No
5	L5	38.1	left antero-lateral	2.50±3.18E-3	2.40±4.03E-4	0.96	0.99	1.23	1.22	No
			right antero-lateral	2.68±4.81E-3	2.49±3.73E-4	0.90	0.99	1.23	1.28	No
			anterior	3.40±2.86E-3	2.27±1.19E-3	0.95	0.99	1.46	1.23	No
6	L1	36.5	left antero-lateral	2.76±1.68E-3	2.51±4.28E-4	0.99	0.99	1.43	1.26	Yes
			right antero-lateral	3.11±2.64E-3	2.43±6.56E-4	0.97	0.99	1.64	1.21	Yes
			anterior	2.36±1.77E-3	2.37±3.38E-4	0.99	0.99	1.17	1.18	No

Notes: [1] Values tabulated are the mean of three measurements for each insertion axis

[2] Distraction was noted only for SG sensor insertion

We acknowledge that the correlations between internal disc pressure, the extent and degree of disc degeneration, and potential clinical symptoms related to degeneration are poorly understood. The new FBG sensor could potentially increase our understanding of these correlations and may eventually lead to the clinical application of

these sensors with the ultimate goal being an increase in the predictive power of discography procedures while avoiding iatrogenic injury to the disk annulus as a result of sensor insertion.

Acknowledgements:

The authors would like to thank Amy Saari for her work in preparing the porcine specimens.

This work was supported in part by the Natural Sciences and Engineering Research Council of Canada (Discovery Grant, Research Tools and Instruments Grant, and Undergraduate Research Fellowship), the Canadian Institutes of Health Research (Interdisciplinary Capacity Enhancement Grant), the Canadian Arthritis Network (Network Scholar Award) and the Michael Smith Foundation for Health Research (Research Unit Award).

References

[1] Waters, T. R., Putz-Anderson, V., Garg, A., and Fine, L. J., 1993, "Revised NIOSH equation for the design and evaluation of manual lifting tasks," Ergonomics, 36(7), pp. 749-776.

[2] Wilke, H.-J., Neef, P., Caimi, M., Hoogland, T., and Claes, L. E., 1999, "New in vivo measurements of pressures in the intervertbral disc in daily life," Spine, 24(8), pp. 755-762.

[3] Yantzer, B. K., Freeman, T. B., Lee, W. E., Nichols, T., Inamasu, J., Guiot, B., and Johnson, W. M., 2007, "Torsion-induced pressure distribution changes in human intervertebral discs," Spine, 32(8), pp. 881-884.

[4] Schmidt, H., Kettler, A., Heuer, F., Simon, U., Claes, L., and Wilke, H.-J., 2007, "Intradiscal pressure, shear strain, and fiber strain in the intervertebral disc under combined loading," Spine, 32(7), pp. 748-755.

[5] Panjabi, M. M., and White, A. A., 2001, Biomechanics in the muscoloskeletal system, Churchill Livingstone.

[6] Nachemson, A., 1960, "Lumbar Intradiscal Pressure," Acta Orthopaedica Scandinavica supplementum, 43, pp. 1-104.

[7] A. Nachemson, M. D., 1966, "The Load on Lumbar Disks in Different Positions of the Body," Clinical Orthopaedics and Related Research, 45, pp. 107-122.

[8] Alf Nachemson, M. D. J. M. M., 1964, "In Vivo Measurements of Intradiscal Pressure," Journal of Bone and Joint Surgery, American Volume 46-A, pp. 1077-1092.

[9] Bryan W. Cunningham, M. Y. K., MD; Patrick S. McNulty, MD; Andrew Cappuccino, MD; Paul C. McAfee, MD, 1997, "The Effect of Spinal Destabilization and Instrumentation on Lumbar Intradiscal Pressure," SPINE, 22(22), pp. 2655-2663.

[10] Mark A. Fye, E. P. S., Manohar M. Panjabi, Jacek Cholewicki, 1998, "Quantitative Discomanometry:

Technique and Reproducibility In Vitro," Journal of Spinal Disorders, 11(4), pp. 335-340.

[11] McNally, D. S., and Adams, M. A., 1992, "Internal intervertebral disc mechanics as revealed by stress profilometry," Spine, 17, pp. 66-73.

[12] Hans-Joachim Wilke, S. W., Lutz E. Claes, Markus Arand, Alexander Wiesend, 1996, "Influence of Varying Muscle Forces on Lumbar Intradiscal Pressure: An In Vitro Study," Journal of Biomechanics, 29, pp. 549-555.

[13] Adams, M. A., McNally, D. S., and Dolan, P., 1996, "'Stress' Distributions Inside Intervertebral Discs," The Journal of Bone and Joint Surgery, 78-B(6), pp. 965-972.

[14] Seo, K.-S., Derby, R., Date, E. S., Lee, S.-H., Kim, B.-J., and Lee, C.-H., 2007, "In vitro measurement of pressure differences unsing manometry at various injection speeds during discography," The Spine Journal, 7, pp. 68-73.

[15] Josef Pospiech, M. D. D. S., M.D.; Hans J. Wilke, Ph.D; Lutz E. Claes, Ph.D, 1999, "Intradiscal Pressure Recordings in the Cervical Spine," Neurosurgery, 44, pp. 379-384.

[16] Steffen, T., Baramki, H. G., Rubin, R., Antoniou, J., and Aebi, M., 1998, "Lumbar intradiscal pressure measured in the anterior and posterolateral annular regions during asymmetrical loading," Clinical Biomechanics, 13, pp. 495-505.

[17] S. Hattori, H. O., S. Kawai, Ube-Shi, 1981, "Cervical Intradiscal Pressure in Movements and Traction of the Cervical Spine," Zeitschrift Fur Orthopadic, 119, pp. 568-569.

[18] P.A. Cripton, G. A. D., L.-P. Nolte, 2001, "A minimally disruptive technique for measuring intervertebral disc pressure in vitro: application to the cervical spine," Journal of Biomechanics, 34, pp. 545-549.

[19] Udd, E., Nelson, D., and Lawrence, C., 1996, "Three Axis Strain and Temperature Fiber Optic Grating Sensor," Proceedings of SPIE, 2718, pp. 104-109.

[20] Tom, F., Peter, O. C., John, L., and David, M., 2005, "Novel FBG interrogation technique for achieving < 100 n epsilon accuracies at remote distances > 70 km," J. B. Hugh, L. Elfed, D. M. Brian, M. Enda, A. M. James, D. O. S. Gerard, G. R. Alan, and E. W. James, eds., SPIE, pp. 663-669.

[21] Geoffrey, A. C., 1998, "Temperature sensor based on a single Bragg grating," C. Brian, and D. C. J. Julian, eds., SPIE, pp. 296-300.

[22] Nunes, L. C. S., Valente, L. C. G., Llerena, R. W. A., Braga, A. M. B., and Triques, A. L. C., 2004, "Simultaneous measurement of temperature and pressure using single fiber Bragg grating and fixed filter demodulation technique," Proceedings of SPIE, 5622, pp. 906-911.

[23] Yunqi, L., Zhuanyun, G., Xiaoyi, D., Zhiguo, L., Donghui, Z., and Chunfeng, G., 1999, "Enhanced pressure and temperature sensitivity of a fiber Bragg grating with polymer packaging," Y. Ichirou, ed., SPIE, pp. 284-287.

[24] Xu, M. G., Reekie, L., Chow, Y. T., and Dakin, J. P., 1993, "Optical in-fibre grating high pressure sensor," Electronics Letters, 29, pp. 398-399.

[25] Xu, M. G., Geiger, H., and Dakin, J. P., 1996, "Fibre grating pressure sensor with enhanced sensitivity using a glass-bubble housing," Electronics Letters, 32, pp. 128-129.

[26] Chuan, S. T., Jianzhong, H., and Rahul, M., 1998, "Fiber optic pressure sensor using a fiber Bragg grating," E. F. Robert, M. G. Lawrence, E. H. Alson, M. Malachy, and J. S. Warren, eds., SPIE, pp. 123-130.

[27] Dennison, C. R., Wild, P. M., Byrnes, P. W. G., Saari, A., Itshayek, E., Wilson, D. C., Zhu, Q. A., Dvorak, M. F. S., Cripton, P. A., and Wilson, D. R., 2007, "*Ex vivo* measurement of lumbar intervertebral disc pressure using fibre-Bragg gratings," Journal of Biomechanics, doi: 10.1016/j.biomech.2007.07.015.

[28] Udd, E., 1991, Fibre Optic Sensors, An Introduction for Engineers and Scientists, Wiley InterScience.

[29] Grace D. O'Connell, B., Edward J. Vresilovic, M., and Dawn M. Elliott, P., 2007, "Comparison of Animals Used in Disc Research to Human Lumbar Disc Geometry," Spine, 32(3), pp. 328-333.

[30] Skrzypiec, D. M., Pollintine, P., Przybyla, A., Dolan, P., and Adams, M. A., 2007, "The internal mechanical properties of cervical intervertebral discs as revealed by stress profilometry," European Spine Journal, doi: 10.1007/s00586-007-0458-z.

Appendix C: Enhanced sensitivity of an in-fibre Bragg grating sensor achieved through fibre diameter reduction

Submitted to Measurement Science and Technology, June 2008.

Enhanced sensitivity of an in-fibre Bragg grating pressure sensor achieved through fibre diameter reduction

Christopher R. Dennison and Peter M. Wild

Department of Mechanical Engineering, University of Victoria, British Columbia, Canada

Corresponding Author:
Chris R. Dennison
University of Victoria
Department of Mechanical Engineering
P.O. Box 3055
Victoria, B.C.
V8W 3P6
Ph: (250) 853-3198
Fax: (250) 721-6051
e-mail: dennison@uvic.ca

Abstract

Biomedical pressure measurement is important in the context of both research and clinical settings. Contemporary biomedical pressure sensors are based on miniaturized piezo-resistive, strain-gauge or other solid-state sensing technologies. All of these technologies have key limitations, when packaged into miniaturized sensors, including fragility and long term instability. In-fibre Bragg gratings (FBGs) are an attractive alternative to these electronics technologies because FBGs are: biocompatible, robust, immune to electromagnetic interference and are mechanically compliant. FBGs can also be used to measure multiple physical parameters and distributions of parameters.

We present a FBG-based pressure sensor that has pressure sensitivity 20 times greater than that of a bare fibre, and a major diameter and sensing area of only 200 μm and 0.02 mm^2, respectively. Increases in pressure sensitivity are achieved by reducing the diameter of the fibre in the region of the Bragg grating, thereby resulting in reduced cross sectional area and therefore increased axial strains for a given applied pressure. The

presented design is an improvement over other FBG pressure sensors that achieve increased sensitivity through mechanical amplification schemes, usually resulting in major diameters and sensing lengths of many millimeters. Sensor sensitivity is predicted using numerical models, and the predicted sensitivity is verified through experimental calibrations. Calibration results demonstrate the FBG sensor's ability to measure pressure with sub-kPa repeatability. To our knowledge, this is the only FBG-based pressure sensor of its size to achieve this repeatability.

1. Introduction

In-fibre Bragg gratings (FBGs) are used extensively as sensors for various parameters including displacement [1], strain [2], temperature [3], pressure [3], humidity [4], and radiation dose [5] among others. FBGs are an attractive alternative to other piezoelectric, resistive or other solid-state sensing technologies because they are: small (typically 125 μm in diameter), mechanically compliant, robust, chemically inert, resistant to corrosive environments, immune to electromagnetic interference, and are capable of simultaneous multi-parameter sensing when suitably configured [6]. Moreover, multiple FBG sensors can be multiplexed along a single optical fibre thereby allowing spatially distributed measurements [7].

These qualities also make FBGs attractive for medical pressure measurement applications; mainly because there is potential to create minimally invasive sensors that address the limitations of current miniature sensors that have exhibited fragility, inconsistency and excessive drift [8]. Clinically relevant applications include pressure measurement in: cerebrospinal fluid (CSF), muscle compartments and blood-vessels. Elevated cranial CSF pressure is caused by brain swelling after head-trauma [9] and can

result in brain damage or death if it exceeds safe levels. It is also hypothesized that elevated CSF pressure in the spinal-cord, which can be caused by various traumas, can lead to cord or brain injury [10]. In muscle compartment syndrome, elevated pressure during and after exercise interferes with blood flow and oxygen diffusion into the muscle [11]. Differential pressures in arteries are caused by blood-flow constrictions such as lesions or plaque deposits; therefore differential pressure measurements can indicate the severity these constrictions. Pressure measurements across arterial stents, devices that are implanted to restore the arterial diameter after constrictions are removed, can be used to assess improvement in blood-flow.

Pressures within the CSF and blood, in the applications mentioned above, vary over several kPa. However, FBG sensors with both the required pressure measurement repeatability and small size do not exist. FBGs are applied only on a limited basis in medical pressure measurement applications; primarily because bare FBGs possess low sensitivity to hydrostatic pressure and are only capable of resolving pressure variations of the order MPa.

In an effort to increase FBG sensitivity to pressure, mechanical amplification schemes, such as polymer coatings on the fibre circumference [12-14] or pressure diaphragms [15], have been developed. Sensors utilizing these schemes have increased pressure sensitivity because the strain along the Bragg grating is amplified relative to the case of a bare-FBG. For example, Xu *et al.* (1996) presented a glass-bubble (4 mm diameter) housed FBG sensor [3] and Liu *et al.* (2000) [16], Sheng *et al.* (2004) [17] and Zhang *et al.* (2001) [18] present polymer coated FBG sensors all with major diameters of the millimeter order. Because of their increased size, these sensors do not retain the

intrinsic benefits offered by FBGs: small size, spatial resolution and mechanical compliance. In the context of medical pressure measurement applications, these large sensors would be more invasive than current alternatives.

Recently, we were the first to develop a FBG-based IVD pressure sensor that had both amplified sensitivity to pressure (*i.e.* seven times that of a bare fibre) as well as a major diameter of only 400 μm and a sensing area of only 0.03 mm^2. This sensor was successfully validated against, and shown to be less invasive than, the current standard sensor used in IVD pressure studies [19]. When this sensor was interrogated using fixed-filter demodulation [20] it had a repeatability of 14 kPa [21]. To our knowledge no FBG sensors have been presented with the pressure sensitivity and small size required for the CSF or arterial blood-pressure measurements previously discussed.

The objective of this work was to design a new FBG sensor that has both increased sensitivity to pressure as well as reduced major diameter, compared to our previous IVD pressure sensor. This was achieved using a five step process. First, a new conceptual design for a FBG sensor was developed to enable pressure sensitivity amplification without increasing the sensor major diameter. Second, the pressure sensitivity of this new conceptual design was calculated using a combined structural finite-element (FE) and strain-optic model. Third, this model was used to study the effect on pressure sensitivity of varying the size of several prototype design features. This was accomplished by incrementally varying the size of the design features over ranges that could be constructed in prototypes and then re-calculating the strains along the Bragg grating for each incremental value of the design feature. Fourth, the model predictions were verified by constructing two sensor prototypes (prototypes 1 and 2) and

experimentally verifying that their sensitivities matched those predicted. Finally, based on design insight gained from the models and verified through testing of prototypes 1 and 2, a third prototype (prototype 3) was constructed that has both increased pressure sensitivity as well as reduced major diameter (as compared to the IVD pressure sensor). The sensitivity of this final sensor was calculated using the FE/strain-optic model and experimentally validated.

2. Materials and methods

2.1 FBG sensor conceptual design

A FBG pressure sensor design was developed to simultaneously satisfy four design goals that are critical for low-pressure medical applications: small size, mechanical compliance, high spatial resolution, and high sensitivity to pressure (Figure 1).

As shown in Figure 1a the sensor design is similar in configuration to our previous IVD pressure sensor [19, 21] in as much as both sensors utilize a length of stainless steel hypodermic tube that houses the FBG. The *probe* (Figure 1c) is gripped at its left hand end in a strain-relief connector that consists of a modified optical fibre patch-chord connector; within which a connection is made to an optical patch cord. The optical patch cord connects to the interrogation system for the sensor. The internal design features unique to the new FBG sensor are shown in Figure 1b.

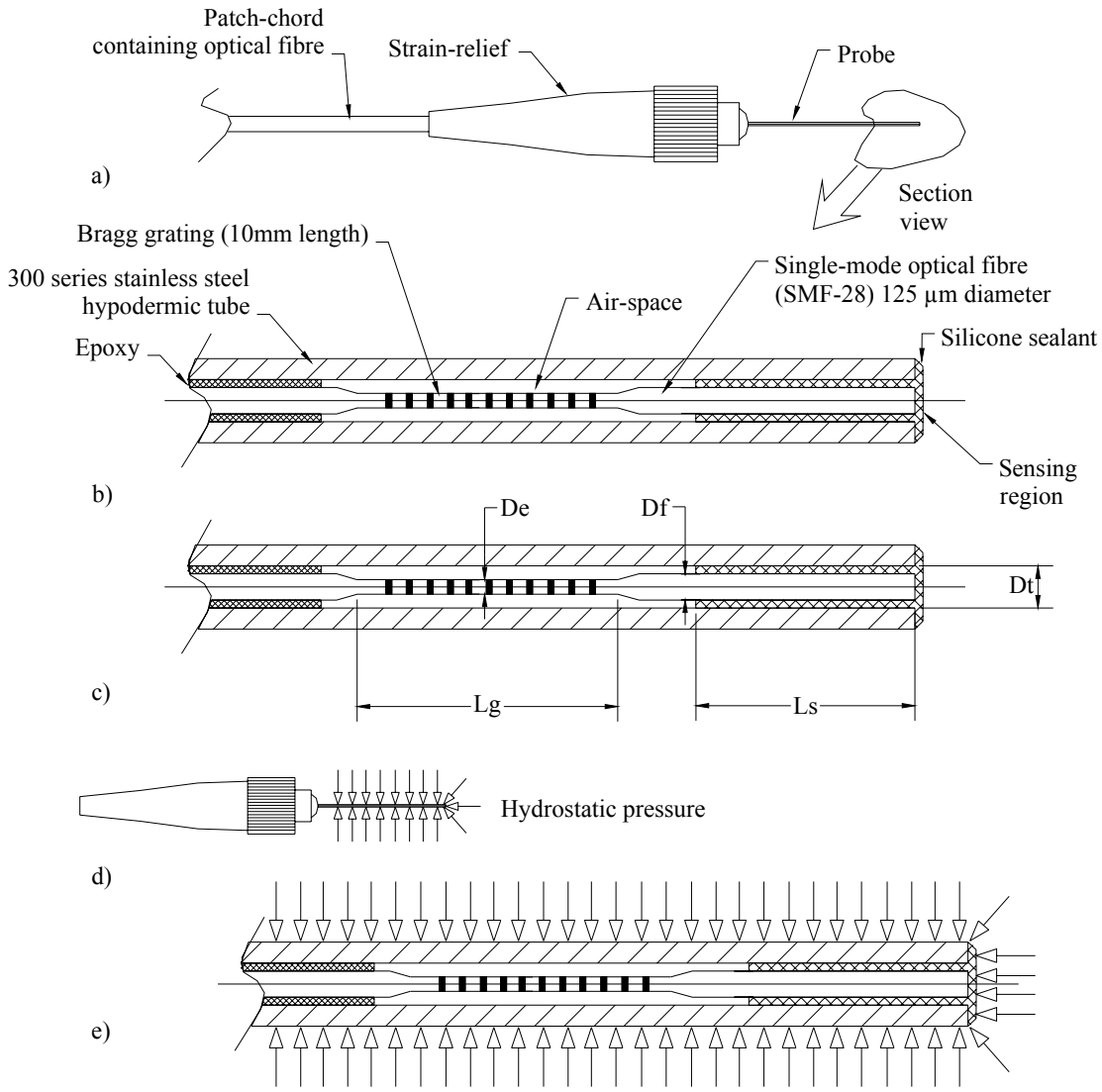

Figure 1: a) schematic of FBG sensor showing external features: probe, strain-relief, and patch-chord b) section view of probe tip showing internal construction of sensor; c) section view of probe tip showing sensor design features that were varied in the finite-element study; d) schematic showing applied hydrostatic pressure on the probe; and e) schematic showing that hydrostatic pressure is applied to both the outer surface of the hypodermic tube and the exposed silicone.

A single-mode optical fibre (Corning SMF-28, Corning NY) is housed within, and positioned along the center-line of the stainless steel hypodermic tube. The fibre is positioned such that its terminal end is approximately aligned with the tip of the

hypodermic tube. At the right-hand end of the hypodermic tube (Figure 1b), there is a silicone seal (Dow Corning 3140 RTV, Midland MI) that covers the end of the hypodermic tube and occupies the annular volume between the inside diameter of the tube, Dt (Figure 1c), and the outside diameter of the optical fibre, Df (Figure 1c). The length of the silicone seal that extends (from right to left in Figure 1b) from the hypodermic tube tip toward the Bragg grating is designated as, Ls (Figure 1c). To the left of the length of fibre contained within the silicone, Ls, there is a segment of fibre that has reduced diameter, De (Figure 1c), that also contains the Bragg grating (10 mm length, Micron Optics, Atlanta GA). The diameter of the fibre is reduced through a chemical etching process that will be described subsequently. The nominal length of the fibre that is reduced in diameter and contains the grating is designated as, Lg (Figure 1c). To the left of the fibre segment of length Lg, the single-mode fibre extends toward the left, is 125 μm in diameter and is fixed in place with epoxy. The volume between the outside diameter of the fibre and the inside diameter of the hypodermic tube, over the length of the sensor between the silicone and epoxy, is occupied by air (Figure 1b), nominally at atmospheric pressure.

When the probe of the sensor is exposed to hydrostatic pressure (Figure 1d and 1e), this pressure acts on the cylindrical outer surface of the hypodermic tube and on the sensing region (Figure 1b). Relative to the silicone, the tube is rigid and, therefore, shields the optical fibre from the effects of the pressure on the outer cylindrical surface of the tube. The pressure applied to the sensing region (Figure 1b) causes strains in the silicone sealant and the optical fibre. Because there is a reduction in the cross sectional area where the fibre diameter transitions from Df to De, the strains along the region of

fibre with length, Lg, and diameter, De, are amplified relative to the strains in the segment of fibre with diameter, Df. As described in the literature, strains in the FBG induce changes in its Bragg wavelength, λ_B, the characteristic wavelength of light that is reflected from a FBG [6]. Consequently, shifts in λ_B are amplified (relative to the case where Df is equal to De) by etching the fibre cross section in the region of the grating. Therefore, the pressure sensitivity is also amplified by etching the fibre as described above.

2.2 Chemical etching

Prior to sensor construction and in preparation for chemical etching, the polyimide jacket that protects the clad of the optical fibre is stripped by immersing the fibre in a mixture of 1-part (by volume) hydrogen peroxide and 3-parts sulfuric acid for 4 minutes. The length of fibre stripped of its polyimide jacketing is approximately 200% of the combined length Ls and Lg, extending from the terminal end of the fibre toward the Bragg grating. The length of the fibre extending from the terminal end toward the Bragg grating, nominally of length Ls, is then re-jacketed (to prevent HF etching along this length) by applying polyethylene glue to the outside diameter of the fibre. The length of the fibre stripped of its polyimide jacket is then immersed into hydrofluoric (HF) acid (48% concentration) to etch the silica glass over the length, Lg, to the new reduced diameter, De. The rate of fibre diameter reduction by HF etching was determined through experiments to be 3.4 μm of silica glass per minute. A specified diameter for the etched section, De, can be obtained by etching for a pre-determined period, this period is calculating based on the rate of diameter reduction (*i.e.* 3.4 μm/min). The etching process was stopped by removing the fibre from the HF bath and immediately submerging it into

a saturated aqueous solution of calcium hydroxide for ten minutes. Previous investigators have shown that Bragg grating performance is not compromised by acid etching [22, 23] to diameter as small as 25 μm [24].

2.3 Finite-element model

The pressure-induced strains within the FBG sensor were calculated as a function of applied hydrostatic pressure using a commercially available suite of finite-element structural analysis codes (ANSYS® version 11, Canonsburg PA). Figure 2 is a schematic that shows the model geometry as well as the displacement and pressure boundary conditions.

A model of prototype 1 was created first, with the following dimensions for the design features shown in Figure 1c: De=65 μm, Df=125 μm, Dt=200 μm, Lg=15 mm and Ls= 1.4 mm. The hypodermic tube outside diameter was 400 μm. Applied pressures were modeled from 0 kPa to 250 kPa to ensure that the strains experienced by the Bragg grating would result in Bragg wavelength variations of greater magnitude than the wavelength measurement accuracy of our interferometer (*i.e.* ± 1.5 pm) (Wavemeter, Burleigh WA-7000, Fishers NY). However, in our calibration studies using the fixed filter demodulation technique, applied pressures were limited to the range associated with the applications listed in the introduction.

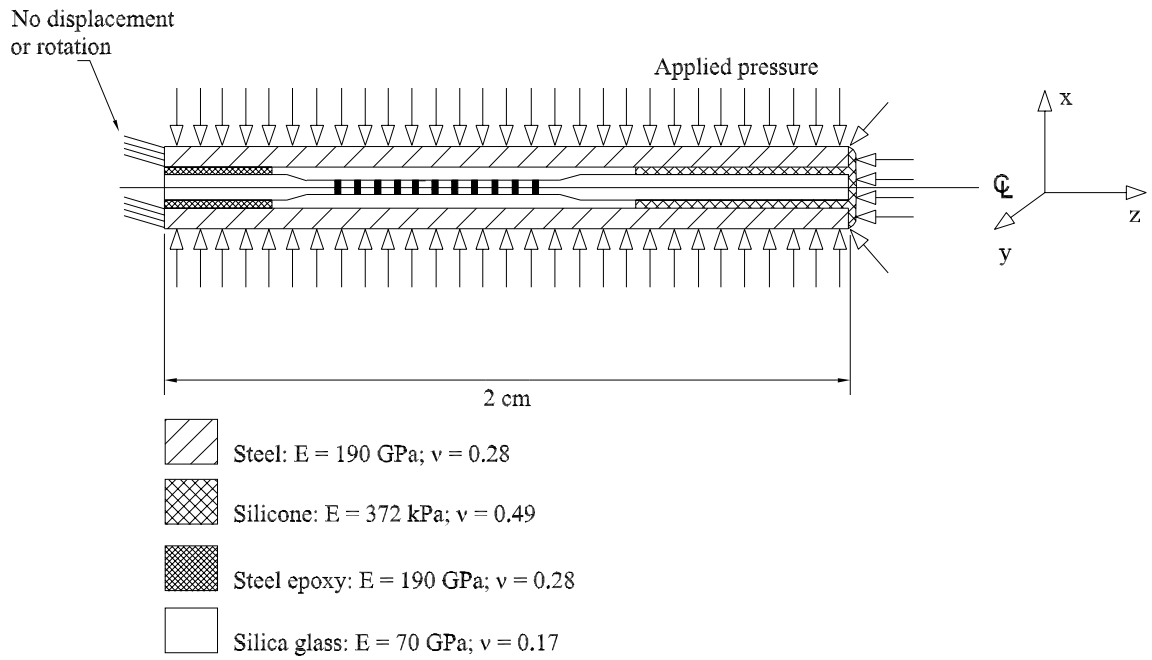

Figure 2: Schematic showing dimensions and displacement/pressure boundary conditions used in the finite-element model. Pressure is applied to entire sensor length. Displacement constraints applied at left-hand-end of hypodermic tube. Materials and properties as indicated.

The pressure induced strains for the prototype 1 model were first obtained by solving a model meshed using PLANE182 (tetrahedron) [25] elements for 250 kPa applied pressure to ensure model deflections were maximum. Mesh refinements were subsequently performed until the relative difference in the predicted strain (along the Bragg grating) between subsequent models was less than 1%. Once the mesh convergence was established, the element type was changed to PLANE42 [25] (triangle) elements to verify element-type independence of the solution by ensuring the relative difference in the average predicted strain along the Bragg grating was less than 1%.

The effect on sensor sensitivity of varying the size of the design features (Figure 1c) was also calculated. Starting with the dimensions of prototype 1, each design feature was incrementally varied over a range of values (Table 1) that could be achieved using

the sensor construction methods available, while holding the size of all other features constant. At each increment, the increase or decrease on sensor sensitivity was assessed by calculating the strains along the Bragg grating. FE models were also solved as part of the development of prototypes 2 and 3. Details of these prototypes will be presented in the results.

Table 1: minimum size, size increment value, and maximum size of design features modeled in finite-element study. Overall sensor length was constant (2cm).

Design feature	Minimum size (μm unless noted)	Increment (μm unless noted)	Maximum size (μm unless noted)
De	25	20	125
Df	65	20	165
Dt	139.7	*	280
Lg	2.5 mm	2.5 mm	15 mm
Ls	0.25 mm	**	2 mm

* Specified for commercially available hypodermic tube sizes
** Variable increment used

2.4 Strain-optic model

As will be discussed in Section 3, and as shown in Figure 3a, pressure applied to the sensing region (Figure 1b) causes uniform compressive strain along the z-axis of the Bragg grating. Uniform axial strain, ε_z, and transverse strain, ε_x and ε_y, have been shown to result in predictable variations in the Bragg wavelength, λ_B, while the full-width at half maximum (FWHM) and the maximum reflectivity remain constant [26], as shown in Figure 3b. Because the strains are uniform along the grating, variations in the Bragg wavelength can be predicted by treating the grating as a whole and using a single equation [7]. Conversely, FBG sensors that have non-uniform strains along the Bragg grating (such as our previous IVD pressure sensor [21]) require more complicated, and

computationally onerous, strain-optic formulations [26-29] to predict wavelength, FWHM and peak reflectivity variations.

Shifts in the Bragg wavelength, denoted by $\Delta\lambda_B$, can be predicted from the strain along the grating using the following closed-form relation that has been extensively discussed/derived by previous investigators [3, 7, 30]:

$$\frac{\Delta\lambda_B}{\lambda_B} = \varepsilon_z - \frac{n_0^2}{2}\left[p_{zz}\varepsilon_z + p_{zx}\varepsilon_x + p_{zy}\varepsilon_y \right] \quad (1)$$

where n_0 is the nominal index of refraction of the fibre specified in the model at 1.44 and p_{zz}, $p_{zx} = p_{zy}$ are elements of the photo-elastic tensor specified at 0.252 and 0.113, respectively [7]. The strains, $\varepsilon_z, \varepsilon_x, \varepsilon_y$, along the core of the fibre were obtained from the results of the FE models and were used in Equation (1) to determine the shift in the Bragg wavelength, $\Delta\lambda_B$, as a function of applied hydrostatic pressure.

2.5 FBG sensor calibration

Two calibration protocols were used to allow collection of two types of calibration data. In the first protocol, data was collected as a function of applied pressures in the form of Bragg wavelength variations. This data was collected because FBG sensor sensitivity is usually reported in terms of wavelength shift versus applied pressure; therefore, by collecting data in this format increases in sensor sensitivity relative to other sensors can be assessed. In the second protocol, we used fixed filter demodulation to collect calibration data in the form of voltages as a function of applied pressures.

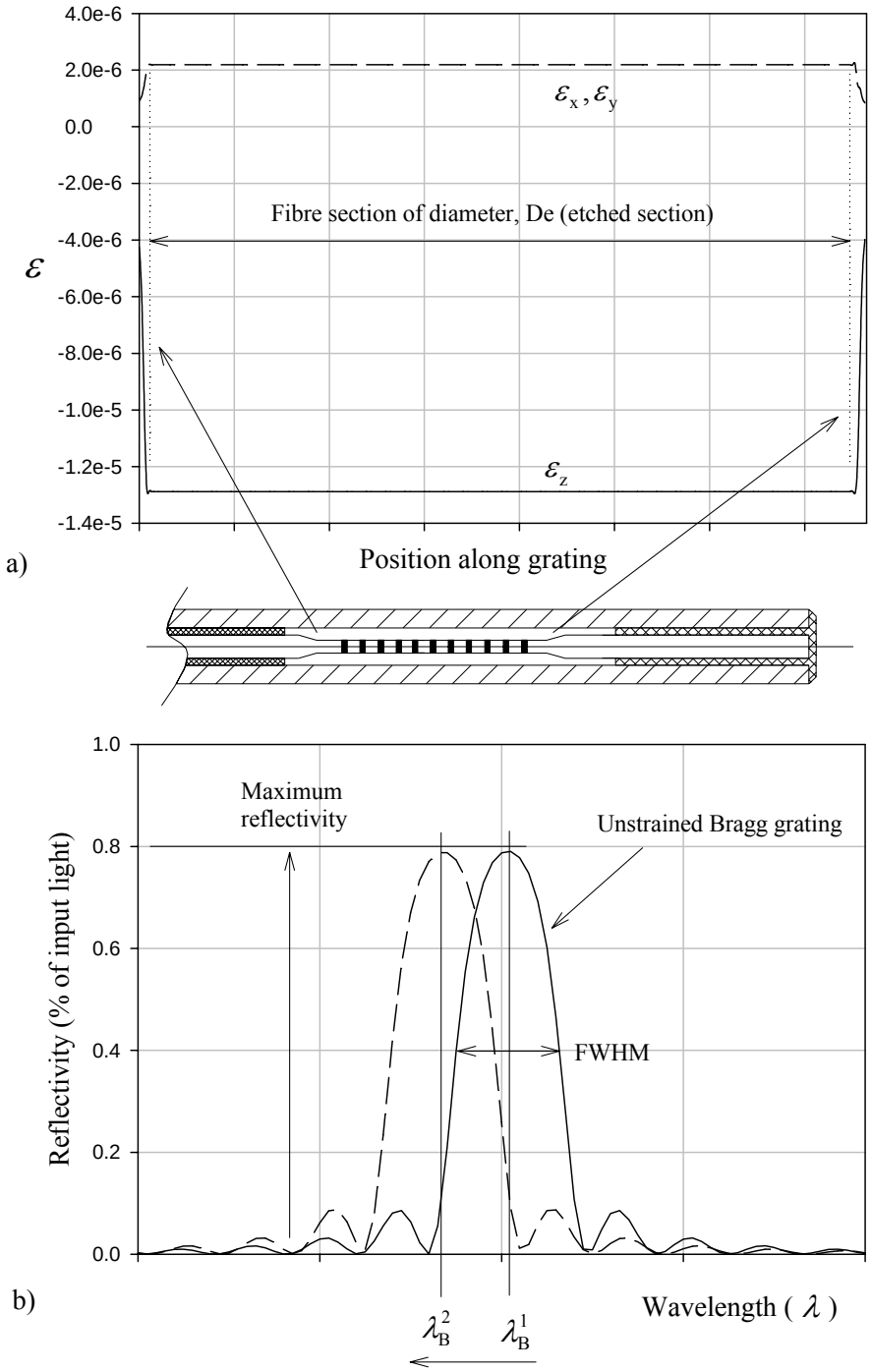

Figure 3: a) Example data for uniform axial, ε_z, and transverse, $\varepsilon_x, \varepsilon_y$, strain versus axial position along grating. Strains shown for 250 kPa applied pressure. b) Uniform strains along the FBG result in shifts in the Bragg wavelength, λ_B while the full-width at half maximum reflectivity (FWHM) and maximum reflectivity remain constant.

Fixed filter demodulation is known to offer higher repeatability than that offered by wavelength measurement with Wavemeters or optical spectrum analyzers [20]. By collecting data in this format we can assess improvements to pressure measurement repeatability achieved by using a commonly employed FBG interrogation method.

Experimental data in the form of Bragg wavelength versus applied hydrostatic pressure, ranging from 0 kPa to 250 kPa, was obtained using a purpose-built calibration apparatus. This experimental data was collected to allow validation of the FBG sensor FE/strain-optic model predicted sensor sensitivity.

The calibration apparatus was configured similarly to that described by Xu *et al.* (1993) [3] and included a broad C-band light source (AFC-BBS1550, Milpitas CA), a bi-directional 3 dB optical coupler (Blue Road Research, Gresham OR), a Wavemeter (specified previously), a purpose built pressure vessel and a reference pressure transducer (OMEGADyne PX01C1, Stamford CT, Acc.: 0.05% FS 70 kPa).

The FBG sensor was inserted into the pressure vessel and sealed *via* a bulkhead fitting. Pressure was manually varied from 0 kPa to 250 kPa to 0 kPa (as reported by the reference transducer) using a manual hydraulic pump (ENERPAC P141, Milwaukee WI) while Bragg wavelength variations were recorded from the Wavemeter. This procedure was repeated three times for each sensor that was tested.

We also commissioned optical interrogation equipment, designed to convert changes in Bragg wavelength to analogue voltages similar, to that described in Nunes *et al.* (2004) [20]. The fixed filter demodulation technique [20] allows direct calibration of the FBG sensor in terms of analogue voltage versus pressure. This demodulation technique and the calibration apparatus were used to calibrate the FBG sensor from 0 kPa

to approximately 13 kPa. Analogue voltage versus applied pressure was acquired at 60 Hz and the average sensitivity of the sensor was calculated, using linear-regression from 3 calibration datasets acquired using hardware and software implemented in LabView© (Version 8, Austin TX).

3. Results

3.1 Finite-element predicted strains

The prototype 1 model (described in Section 2.3: De=65 μm, Dt=200 μm, tube outside diameter 400 μm) satisfied all convergence criteria (outlined in the Methods) with an axisymmetric mesh of 28,000 PLANE182 elements and with nominal distance of 1.25 x 10^{-5} m between element nodes. This mesh also satisfied all ANSYS® aspect ratio criteria [31] both before the model was solved and after the model was solved and the mesh had deflected. The relative difference in the predicted strains using PLANE182 [25] (tetrahedron) elements and PLANE42 [25] (triangle) elements was 0.08 % (ε_z) and 0.00 % ($\varepsilon_x, \varepsilon_y$) and satisfied the element independence criteria outlined in the Methods.

Figure 4a shows the strains along the core of the optical fibre (Figure 2: x=y=0) for 250 kPa applied pressure. Progressing from right to left along the sensor (Figure 4), both axial and transverse strains have constant magnitude along Ls until the cross-sectional diameter of the fibre transitions from Df to De. Along the length of the fibre that is etched (which contains the Bragg grating of length Lg) the strains are amplified relative to those encountered along the fibre length Ls as shown by the abrupt increase in strain magnitude at 18.6 mm. Progressing towards the length of fibre supported by the epoxy, the strain magnitudes diminish where the fibre diameter increases from De to Df again (position of 3.6 mm). The variations in strains shown in Figure 4a are typical of all

the sensor prototypes modeled. Figure 4b shows that both the axial and transverse strain magnitudes along Lg are linear functions (r^2=1.00) of the applied pressure on the sensor. It is also worth noting that the transverse strains plotted have magnitude equal to the product of the Poisson ratio of the fibre and the axial strain (*i.e.* they are due to transverse expansion of the fibre resulting from axial compression). The predicted variation in the strains shown in Figure 4b will result in a linear variation of the Bragg wavelength with pressure.

We also verified that the strains were uniform over the entire cross-section of the core of the single-mode fibre (diameter 9 μm) that contains the Bragg grating (over Lg, and $0<x,y<9$ μm). The average difference between the strains predicted along the center-line of the core (over Lg, and x=y=0) and the outside diameter of the core was less than 0.01 % of the strain magnitude over Lg, for both axial and transverse strains.

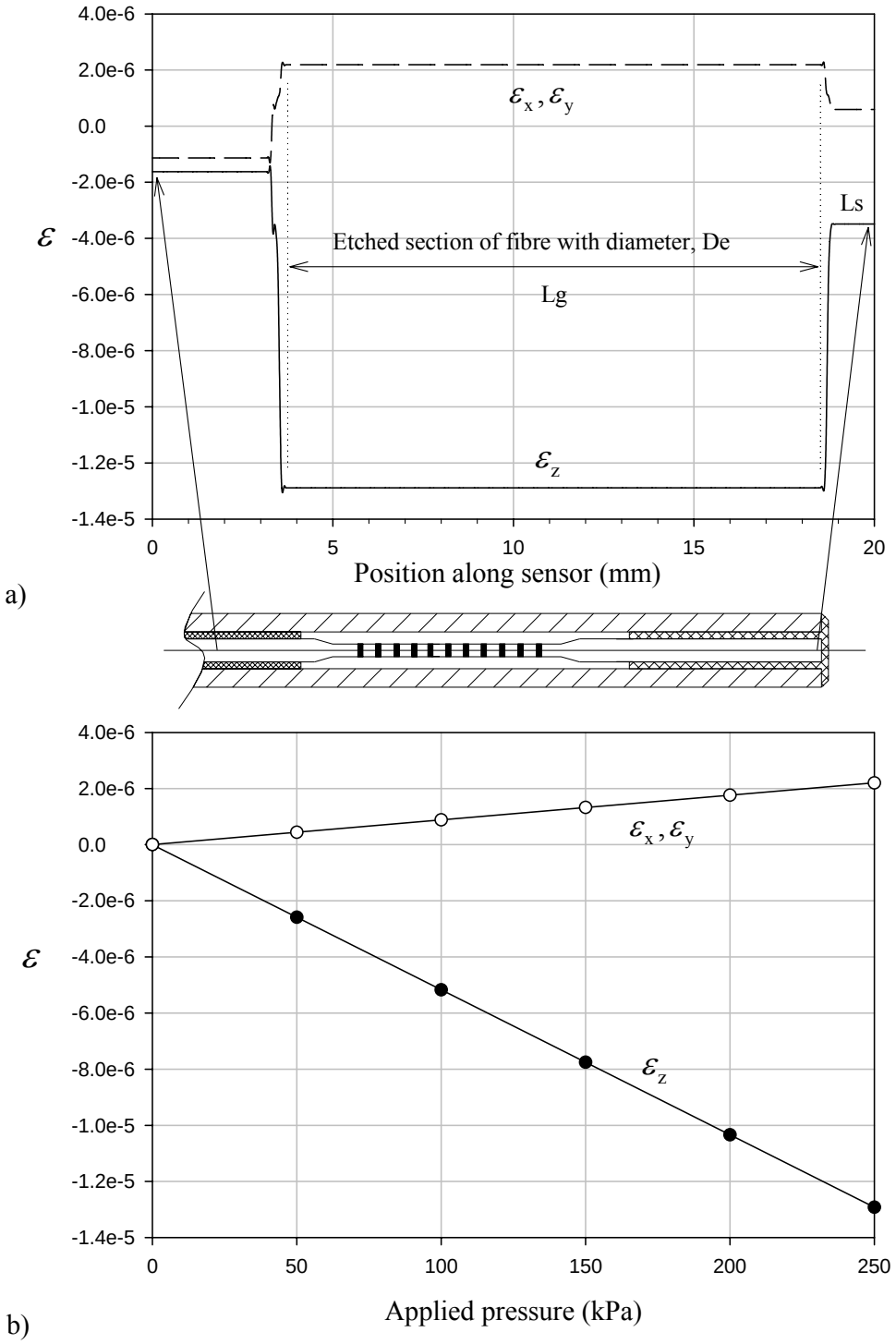

Figure 4: a) Strain data plotted versus position along sensor, for 250 kPa applied pressure on the prototype 1 model described in the Methods; b) magnitude of strains along the etched region of the fibre (corresponding to the Bragg grating location) plotted versus varying applied pressure.

3.2 Effects of feature size on strain along FBG

Figure 5 shows the effect (increase/decrease in axial strain along grating) of varying the size of the design features shown in Figure 1c. The results shown were obtained from the FE study where the initial value of all design parameters matched those of prototype 1. The sizes of the design features were varied one at a time, incrementally, while holding the size of all other features constant. To avoid plotting negative strain magnitudes throughout the balance of this paper, all strains are plotted as positive quantities.

As shown in Figure 5b, reducing the diameter Dt from 200 μm to 139.7 μm leads to 65 % decrease (normalized to strain of the prototype 1 model) in the axial strain. Conversely, reduction in overall sensor length increases the axial strain, as shown by Figures 5d and 5e for Lg and Ls, respectively. Reducing the length of the Bragg grating, Lg, from 15 mm to 2.5 mm results in a 42 % increase in the axial strain. Furthermore, reducing the length of the silicone, Ls, from 1.4 mm to 0.25 mm results in a 44 % increase in the axial strain (Figure 5e).

As shown in Figure 5c, if Df is etched so that it is equal to De, there is only a 23 % decrease in the axial strain along the grating (relative to the prototype 1 model). Furthermore, reductions in De result in the most drastic increases in the axial strain along the grating (Figure 5a). Reducing De from 65 μm to 25 μm results in a strain magnitude increase of 947 %, which is far more than any reduction in strain that results from varying other design parameters (Figure 5f).

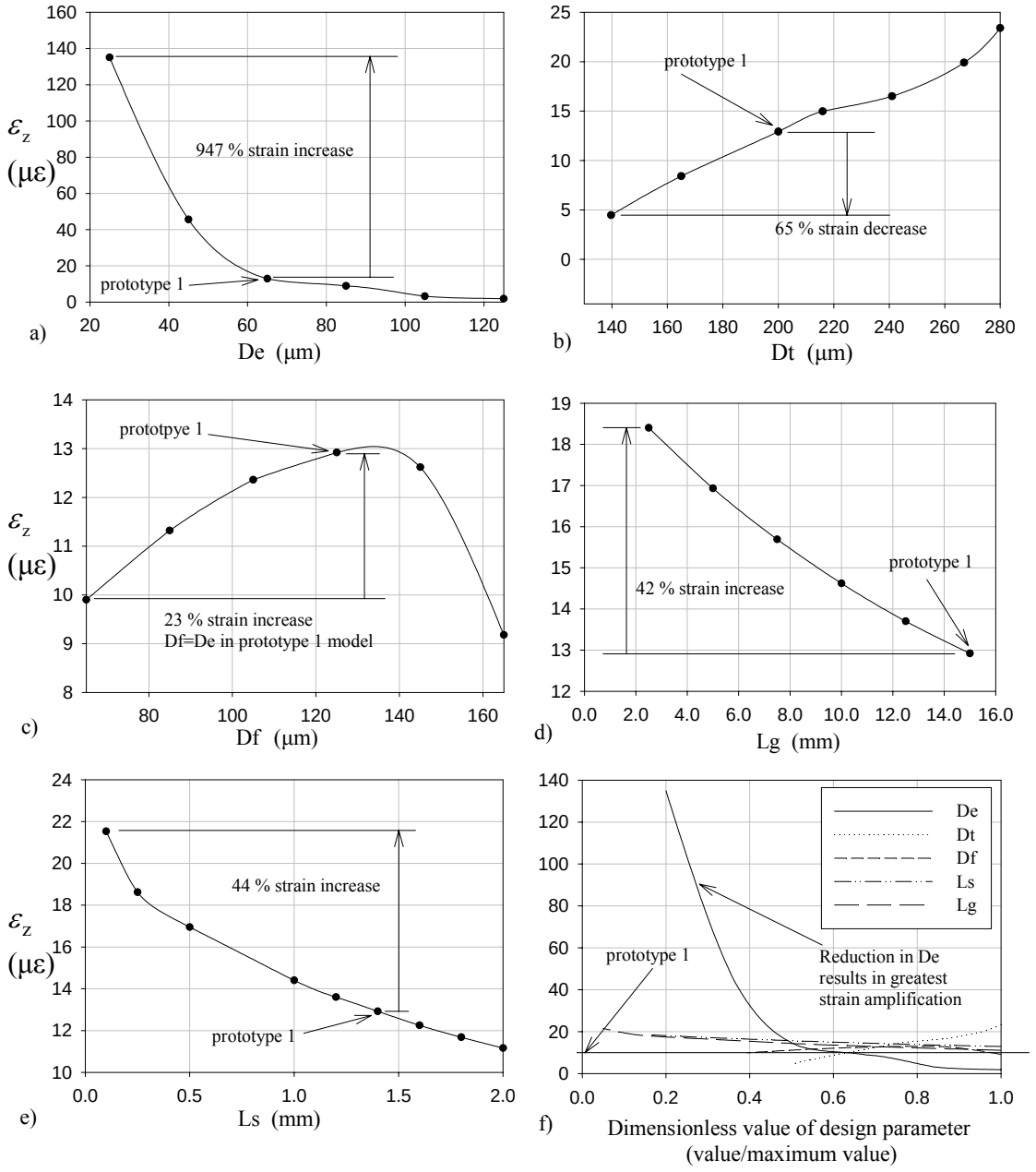

Figure 5: Variations in the axial strain along Bragg grating for various sizes of the design features, and for 250 kPa applied pressure. Strain levels for the prototype 1 model denoted in each plot. Shown at bottom-right, Variations in axial strain for all design parameters plotted against non-dimensional values of the parameter values. More than any other design parameter, reduction in de amplifies strain along Bragg grating.

The principal design objectives of the sensor development were to increase sensitivity to applied pressure as well as to reduce the major diameter of the sensor. The

latter objective is achieved by constructing sensors with reduced hypodermic tube diameter. Reducing Df to equal De could potentially allow sensors having the smallest major diameters. By constructing sensors in such a manner, the fibre segments Lg and Ls would have identical diameters, thereby allowing smaller hypodermic tubes than may otherwise be achievable when Df is greater than De. The results presented above show that FBG sensors of the presented design could achieve both reduced sensor diameter as well as amplified pressure sensitivity.

3.3 FE/strain-optic predicted pressure sensitivity and experimental validation

To verify the results obtained from the FE study, the pressure sensitivities ($\Delta\lambda_B / \Delta P$) of the prototype 1 model and two additional prototypes (prototypes 2 and 3) were calculated using the predicted strains and the strain-optic model. The dimensions of these prototypes are given in Table 2. Figure 6 shows the FE/strain-optic-predicted and experimentally measured variations in the Bragg wavelength, $\Delta\lambda_B$, versus applied pressure, ΔP, for prototype 1. As shown, the predicted and experimentally measured sensitivities match to within 3.5 % (experimental result is reference for comparison) (Table 2). The sensitivity of the prototype 1 is approximately 20 times that of a bare FBG, as shown in Figure 6 [3]. Table 2 shows the predicted and measured pressure sensitivities of prototypes 2 and 3. As shown, the predicted and measured sensitivities are all approximately 20 times that of a bare-FBG and match extremely well, with relative differences of 7.01 % and 2.04% for prototype 2 and 3, respectively.

Table 2: Predicted and experimentally measured pressure sensitivities for the three FBG sensor prototypes. Design features sizes are specified for each prototype. Pressure sensitivities (pm/MPa) and correlation coefficients (r^2) obtained from regression calculations.

Prototype	Design feature sizes	Predicted pressure sensitivity (pm/MPa) $(r^2)^+$	Experimentally measured pressure sensitivity (pm/MPa) $(r^2)^+$	Sensitivity: Bare-FBG sensitivity
(1) 400 μm outside diameter	De=65 μm Df=125 μm Dt=200 μm Lg=15 mm Ls=1.4 mm	-62.4 1.00	-60.3 0.99	19.5
(2) 356 μm outside diameter	De=37 μm Df=125 μm Dt=178 μm Lg=15 mm Ls=1.4 mm	-68.7 1.00	-64.2 0.99	20.7
(3) 200 μm outside diameter	De=25 μm Df=25 μm Dt=165 μm Lg=15 mm Ls=1.4 mm	-59.9 1.00	-58.7 0.99	19.0

Notes: $^+$ correlation coefficients obtained from regression calculations

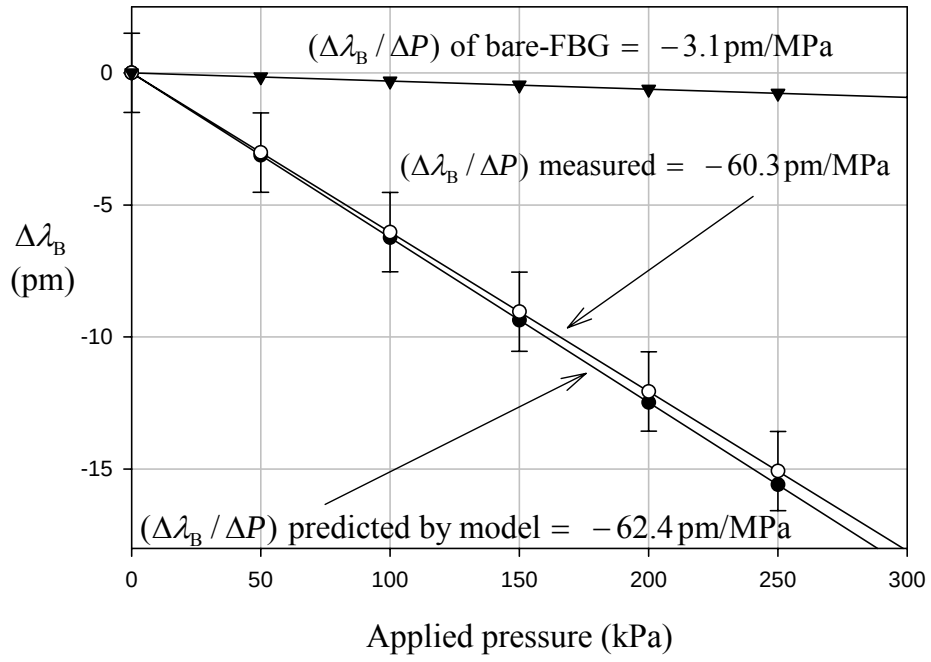

Figure 6: Predicted and experimentally measured change in Bragg wavelength versus applied pressure for prototype 1. Vertical error bars (± 1.5 pm) correspond to absolute accuracy of Wavemeter. Horizontal error bars (± 0.034 kPa) are not visible at scale shown but correspond to the accuracy of the reference transducer. Data points also plotted based on published sensitivity of bare-FBG pressure sensor to show scale of sensitivity increases.

3.4 Fixed filter demodulation

The calibration data presented to this point has been in terms of Bragg wavelength variations versus applied hydrostatic pressure. Wavelength variations were measured using the Wavemeter. The results presented in this section were collected using the fixed filter demodulation technique mentioned in the Methods. Calibration results, for prototype 3, obtained using the fixed filter demodulation technique demonstrate the sensor's ability to measure pressure variations of the order kPa, as shown in Figure 7. The average regression-calculated slope from the three calibration data sets was 1.43 ± 0.023 mV/V/kPa (mean ± standard deviation). The regression-calculated vertical error

bars (Figure 7) increase in size as applied pressure increases based on the uncertainty in the regression-calculated slope [32]. The minimum value is ± 0.20 mV/V which increases at a rate of 0.023 mV/V/kPa to ± 0.51 mV/V at 13.64 kPa. The uncertainty in pressure measurement is estimated as the maximum error (*i.e.* ± 0.51 mV/V) divided by the regression-calculated slope (*i.e.* 1.43 mV/V/kPa) and has a value of ± 0.36 kPa.

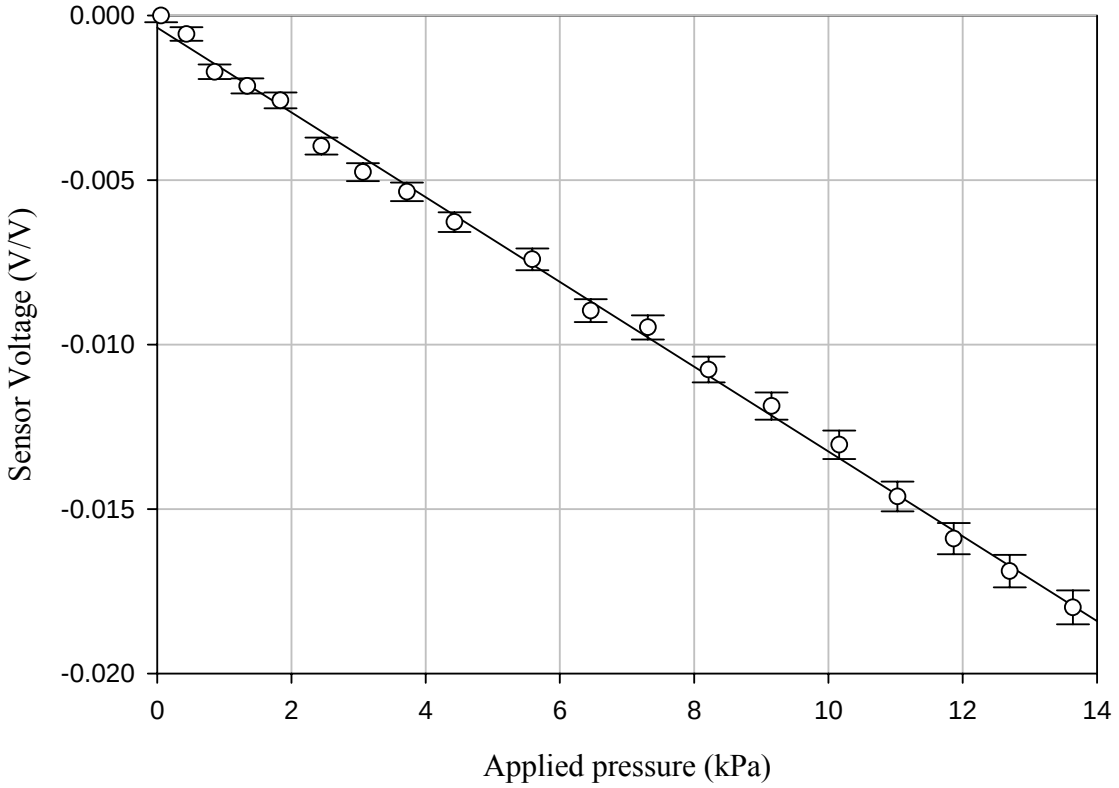

Figure 7: Example calibration results showing variations in voltage versus applied pressure obtained using the FBG sensor and fixed filter demodulation technique. Vertical error bars obtained from regression, horizontal error bars (± 0.034 kPa) not visible at scale shown, but correspond to accuracy of reference transducer.

5. Discussion

We have shown, through both modeling and experimental validation, that reduction in the fibre diameter over the length of the grating can lead to significant strain amplification. By amplifying the strain experienced by the Bragg grating, sensor

sensitivity is amplified compared to the case of a bare-FBG with a typical single-mode fibre diameter. As shown in Figure 5a through 5f, reductions in the etched diameter, De, lead to the greatest increases in axial strain along the grating.

This new FBG sensor design simultaneously achieves increased pressure sensitivity, reduced major diameter and high spatial resolution. The 200 μm diameter prototype (shown in Figure 8) has a sensitivity ($\Delta\lambda_B / \Delta P$) of 58.7 pm/MPa, which is approximately 19 times that of a bare-FBG (*i.e.* 3.1 pm/MPa) and approximately 3 times that of our previous IVD pressure sensor which had an outside diameter of 400 μm (*i.e.* 20 pm/MPa). Furthermore, the sensing region of this 200 μm diameter prototype is only 0.02 mm^2. The bare-fibre, 400 μm prototype and 200 μm prototype are shown in Figure 8.

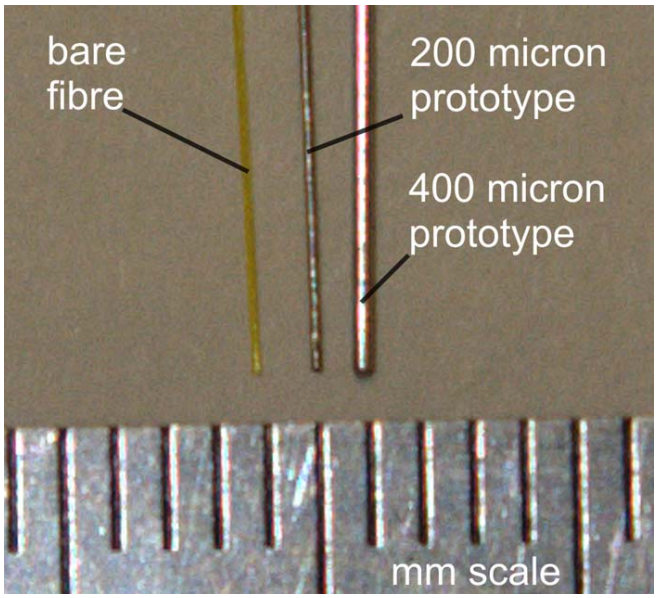

Figure 8: Image showing relative diameters of prototype 1 (400 μm outside diameter), smallest FBG sensor prototype (200 μm outside diameter) and bare single-mode fibre (nominal 125 μm outside diameter).

To compare the performance of the etched FBG sensor to other FBG sensors presented in the literature, the pressure sensitivities of the various FBG sensors were

plotted versus sensor major diameter. Figure 9 shows, for some of the FBG sensors in the literature, the ratio of FBG sensor sensitivity to bare-FBG sensitivity plotted against the ratio of FBG sensor diameter to bare-FBG diameter. The polymer coated FBG sensors presented by Sheng *et al.* (2004) and Zhang *et al.* (2001) have the greatest sensitivities (Figure 9) however they also have the greatest major diameters [17, 18]. For example the polymer coated sensor of Zhang *et al.* (2001) is 100 times larger than a bare-FBG and the sensor presented by Sheng *et al.* (2004) is almost 200 times larger. In the context of biomedical pressure measurement applications these sensors have major diameters that are much too large for *in vivo* applications [8] and likely also have limited utility in *ex vivo* experiments.

The IVD sensor and etched sensors are the only sensors plotted in Figure 9 that have both increased pressure sensitivity and sub-mm major diameters, as required for biomedical applications [8]. The IVD pressure sensor [Spine ref] has increased sensitivity, approximately seven times that of a bare-FBG, and a major diameter only 3.2 times that of a bare-FBG (*i.e.* 400 μm). The new FBG sensor prototypes 1, 2 and 3 have even greater sensitivities, approaching those of the smallest polymer jacketed sensors (Figure 9) [18]. Prototypes 1 through 3 all have sensitivities approximately 20 times that of a bare-FBG. Prototype 3 (200 μm outside diameter) has a major diameter that is only 60 % greater than a bare-fibre (Figure 9).

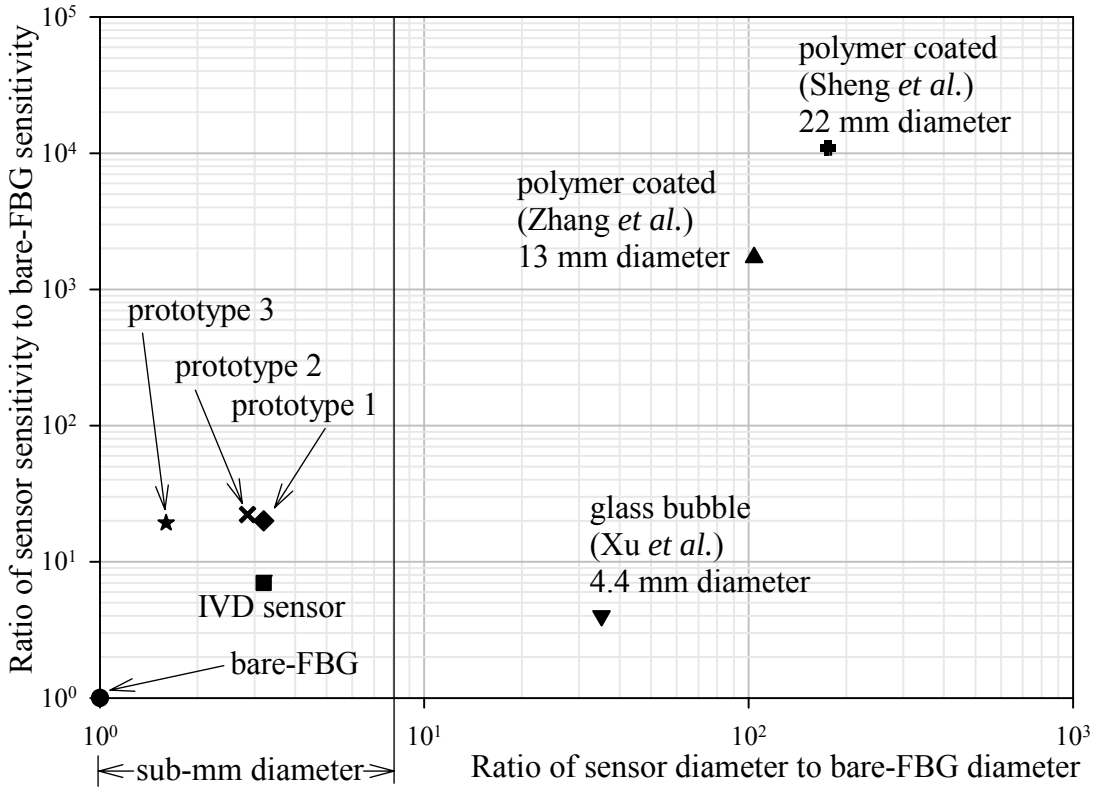

Figure 9: Logarithmic ratio FBG sensor sensitivity/bare-FBG sensitivity versus the logarithmic ratio of sensor diameter/bare FBG diameter.

When the 200 μm prototype is interrogated with fixed filter demodulation, the increased physical sensitivity of the sensor and the increased repeatability of the fixed filter demodulation [20], result in a sensing system that is appropriate for pressure variations of the order kPa (Figure 7). Future work will include refinements to the fixed filter demodulation scheme to achieve even greater repeatability in pressure measurements.

6. Conclusions

In this paper we describe the design, analysis and performance of a FBG pressure sensor that has pressure sensitivity much greater than that of a bare FBG (*i.e.* 20 times)

while maintaining both small size (*i.e.* only 200 μm diameter) and mechanical compliance. Increases in pressure sensitivity are achieved through mechanical amplification of axial strains experienced by the Bragg grating. Mechanical amplification is achieved by reducing the diameter of the fibre in the region of the Bragg grating, thereby resulting in reduced cross sectional area and therefore increased axial strains for a given applied pressure.

Pressure sensitivity of the sensors was modeled using a combined finite-element and strain optic formulation. Strains along the Bragg grating were predicted using the finite-element model, and these strains were then used in strain-optic equations to predict the corresponding shift in the Bragg wavelength for various applied pressures. Furthermore, potential increases/decreases in sensor sensitivity were studied by varying the size of several sensor features and calculating the resulting increase/decrease in the axial strain along the grating.

Three sensor prototypes were constructed and experimentally calibrated. The experimentally measured sensitivities were compared to the predictions of the model described above and good agreement was observed. Sensor calibration was then repeated using a fixed filter demodulation technique. Results obtained showed this new FBG sensor is capable of resolving pressure variations of the order kPa. To our knowledge, this is the only FBG sensor of this size (200 μm outside diameter) capable of resolving pressure variations of this magnitude.

References

[1] Pieter, L. S., Beatrys, M. L., and Anatoli, A. C., 2005, "Chirped fiber Bragg grating sensor for pressure and position sensing," SPIE, p. 054402.

[2] Udd, E., Lawrence, C., and Nelson, D., 1997, "Development of a Three Axis Strain and Temperature Fiber Optic Grating Sensor," Proceedings of SPIE, 3042, pp. 229-236.

[3] Xu, M. G., Reekie, L., Chow, Y. T., and Dakin, J. P., 1993, "Optical in-fibre grating high pressure sensor," Electronics Letters, 29, pp. 398-399.

[4] Yeo, T. L., Sun, T., Grattan, K. T. V., Parry, D., Lade, R., and Powell, B. D., 2005, "Characterisation of a polymer-coated fibre Bragg grating sensor for relative humidity sensing," Sensors and Actuators B: Chemical, 110, pp. 148-155.

[5] Fernandez, A. F., Brichard, B., Berghmans, F., and Decreton, M., 2002, "Dose-Rate Dependencies in Gamma-Irradiated Fiber Bragg Grating Filters," IEEE Transactions on Nuclear Science, 49(6), pp. 2874-2878.

[6] Udd, E., 1991, Fibre Optic Sensors, An Introduction for Engineers and Scientists, Wiley InterScience.

[7] Measures, R. M., 2001, Structural Health Monitoring with Fiber Optic Technology, Academic Press.

[8] Mignani, A. G., and Baldini, F., 1996, "Biomedical sensors using optical fibres," Rep. Prog. Phys., 59, pp. 1-28.

[9] Warner, D. S., and Borel, C. O., 2004, "Treatment of Traumatic Brain Injury: One Size Does Not Fit All," Anesthesia Analgesia, 99, pp. 1208-1210.

[10] Jones, C. F., Kwon, B. K., Itshayek, E., Markez, J., Dennison, C., Singlehurst, D., Wild, P., and Cripton, P. A., 2008, "Development and pilot results from a large animal study to measure cerebrospinal fluid pressure before, during and after spinal cord injury," 4th Annual Injury Biomechanics SymposiumOhio State University.

[11] Jawed, S., Jawad, A. S. M., Padhiar, N., and Perry, J. D., 2001, "Chronic exertional compartment syndrome of the forearms secondary to weight training," Rheumatology, 40, pp. 344-345.

[12] Hao-Jan, S., Ming-Yue, F., Tzu-Chiang, C., Chia-Min, L., Wen-Fung, L., and Sheau-Shong, B., 2004, "High-sensitivity pressure sensor based on a fiber Bragg grating," C. Brian, A. M. Michael, P. D. John, D. C. Samuel, and E. K. Helmut, eds., SPIE, pp. 248-254.

[13] Liu, L., Zhao, Q., Zhang, W., Zhang, H., Jin, L., Zhao, L., Yan, Y., and Gao, S., 2005, "Fiber Grating Pressure Sensor with Enhanced Sensitivity," Proceedings of SPIE, 5623, pp. 16-19.

[14] Ngoi, B. K. A., Paul, J., Zhao, L. P., and Fang, Z. P., 2004, "Enhanced lateral pressure tuning of fiber Bragg gratings by polymer packaging," Optics Communications, 242, pp. 425-430.

[15] Maier, R. R. J., Barton, J. S., Jones, J. D. C., McCulloch, S., and Burnell, G., 2003, "Dual-fibre Bragg grating sensor for barometric pressure measurement," Measurement Science and Technology, 14, pp. 2015-2020.

[16] Liu, Y., Guo, Z., Zhang, Y., Seng, K., Dong, C., and Dong, X., 2000, "Simultaneous pressure and temperature measurement with polymer-coated fibre Bragg grating," Electronics Letters, 36(6), pp. 564-566.

[17] Sheng, H.-J., Fu, M.-Y., Tzu-Chiang, C., Wen-Fung, L., and Sheau-Shong, B., 2004, "A lateral pressure sensor using a fiber bragg grating," IEEE Photonics Technology Letters, 16(4), pp. 1146-1148.

[18] Zhang, Y., Feng, D., Liu, Z., Guo, Z., Dong, X., Chiang, K. S., and Chu, B. C. B., 2001, "High-sensitivity pressure sensor using a shielded polymer-coated fiber Bragg grating," IEEE Photonics Technology Letters, 13(6), pp. 618-619.

[19] Dennison, C. R., Wild, P. M., Dvorak, M. F. S., Wilson, D. R., and Cripton, P. A., 2008, "Validation of a novel minimally invasive intervertebral disc pressure sensor utilizing in-fibre Bragg gratings in a porcine model: An ex vivo study," Spine (In Press).

[20] Nunes, L. C. S., Valente, L. C. G., Llerena, R. W. A., Braga, A. M. B., and Triques, A. L. C., 2004, "Simultaneous measurement of temperature and pressure using single fiber Bragg grating and fixed filter demodulation technique," Proceedings of SPIE, 5622, pp. 906-911.

[21] Dennison, C. R., Wild, P. M., Wilson, D. R., and Cripton, P. A., 2008, "A minimally invasive in-fibre Bragg grating sensor for intervertebral disc pressure measurements," Measurement Science and Technology, under-review.

[22] Abe, I., Frazao, O., Schiller, M. W., Nogueira, R. N., Kalinowski, H. J., and Pinto, J. L., 2006, "Bragg gratings in normal and reduced diameter high birefringence fibre optics," Measurement Science and Technology, 17, pp. 1477-1484.

[23] Tran, T. V. A., Han, Y.-G., Lee, Y. J., Kim, S. H., and Lee, S. B., 2005, "Performance enhancement of long-distance simultaneous measurement of strain and temperature based on a fiber Raman laser with an etched FBG," IEEE Photonics Technology Letters, 17(9), pp. 1920-1922.

[24] Tu, P.-J., Liu, W.-F., and Chen, T.-C., 2005, "Tunable fibre laser based on an etched fiber Bragg grating," Microwave and Optical Technology Letters, 45(4), pp. 297-300.

[25] Milson, T. C. S., and Stilante, K. M., 1995, "Silicon integrated optical pressure sensor based on distributed Bragg reflector structure," J. Tomasz, ed., SPIE, pp. 148-159.

[26] Huang, S., LeBlanc, M., Ohn, M. M., and Measures, R. M., 1995, "Bragg intragrating structural sensing," Applied Optics, 34(22), pp. 5003-5009.

[27] Weller-Brophy, L. A., and Hall, D. G., 1985, "Analysis of waveguide gratings: application of Rouard's method," Journal of the Optical Society of America A, 2(6), pp. 863-871.

[28] Poladian, L., 1993, "Graphical and WKB analysis of nonuniform Bragg gratings," Physical Review E, 48(6), pp. 4758-4767.

[29] Hill, K. O., 1974, "Aperiodic distributed-parameter waveguides for integrated optics," Applied Optics, 13(8), pp. 1853-1856.

[30] Xu, M. G., Geiger, H., and Dakin, J. P., 1996, "Fibre grating pressure sensor with enhanced sensitivity using a glass-bubble housing," Electronics Letters, 32, pp. 128-129.

[31] Colin, G. W., Andreas, O., and Deepak, G. U., 1995, "Fiber Bragg-grating-based laser sensor," G. U. Deepak, ed., SPIE, pp. 48-56.

[32] Taylor, J. R., 1997, An Introduction to Error Analysis, The study of uncertainties in physical measurements, University Science Books, Sausalito, CA.